Magnetic Signature Characterization of a Fixed-Wing Vertical Take-off and Landing (VTOL) Unmanned Aerial Vehicle (UAV)

by

Cody Robert Daniel Hansen
B.Eng., Royal Military College of Canada, 2013

A Thesis Submitted in Partial Fulfillment
of the Requirements for the Degree of

MASTER OF APPLIED SCIENCE

in the Department of Mechanical Engineering

Supervisory Committee

Magnetic Signature Characterization of a Fixed-Wing Vertical Take-off and Landing (VTOL) Unmanned Aerial Vehicle (UAV)

by

Cody Robert Daniel Hansen
B.Eng., Royal Military College of Canada, 2013

Supervisory Committee

Dr. Afzal Suleman (Department of Mechanical Engineering)
Supervisor

Dr. Andrew Rowe (Department of Mechanical Engineering)
Departmental Member

Abstract

Supervisory Committee

Dr. Afzal Suleman (Department of Mechanical Engineering)
Supervisor

Dr. Andrew Rowe (Department of Mechanical Engineering)
Departmental Member

The use of magnetometers combined with unmanned aerial vehicles (UAVs) is an emerging market for commercial and military applications. This study presents the methodology used to magnetically characterize a novel fixed-wing vertical take-off and landing (VTOL) UAV. The most challenging aspect of integrating magnetometers on manned or unmanned aircraft is minimizing the amount of magnetic noise generated by the aircraft's onboard components. As magnetometer technology has improved in recent years magnetometer payloads have decreased in size. As a result, there has been an increase in opportunities to employ small to medium UAV with magnetometer applications. However, in comparison to manned aviation, small UAVs have smaller distance scales between sources of interference and sensors. Therefore, more robust magnetic characterization techniques are required specifically for UAVs. This characterization determined the most suitable position for the magnetometer payload by evaluating the aircraft's static-field magnetic signature. For each aircraft component, the permanent and induced magnetic dipole moment characteristics were determined experimentally. These dipole characteristics were used to build three dimensional magnetic models of the aircraft. By assembling the dipoles in 3D space, analytical and numerical static-field solutions were obtained using MATLAB computational and COMSOL finite element analysis frameworks. Finally, Tolles and Lawson aeromagnetic compensation coefficients were computed and compared to evaluate the maneuver noise for various payload locations. The magnetic models were used to study the sensitivity of the aircraft configuration and to simultaneously predict the effects at potential sensor locations. The study concluded by predicting that a wingtip location was the area of lowest magnetic interference.

Table of Contents

List of Tables

List of Figures

Acknowledgments

The completion of this work was accomplished with a large amount of support from individuals and organizations.

I would like to thank my supervisor, Dr Afzal Suleman, for believing in me from the beginning and providing me the opportunity for growth and professional development throughout the project.

The experimental aspects of the project were accomplished with the support of NRC, CAE, DRDC and Aeromagnetic Solutions Incorporated. Also, I'd like to thank NRCan and 676 RCACC Parents group for allowing us to utilize their respective facilities to conduct experiments. From DRDC, Dr Zahir Daya and Jeff Scrutton contributed their experience and insights. From NRC, Tomas Naprstek (soon to be Dr Naprstek) and Janine Gorman ensured that the accuracy and scientific aspects of the measurements were sound. Most of all, I'd like to thank Brad Nelson (Aeromagnetic Solutions Incorporated) for his patience in mentoring me all throughout the project. He responded to countless emails and endured many long duration phone calls.

On the CfAR design team, I'd like to thank Jenner, Max and Steve for advising and executing many of the complex design feats in less time than truly needed. I'd like to thank Mairina and Gonçalo for their contributions to the project. Gonçalo kept the project management aspects afloat when I was drowning in other commitments. Simultaneously, Mairina designed and built a robust engine test stand. Their implicit moral support is also notable.

Finally, I'd like to thank Dave Lee for assisting in the thesis revision process. It should be known that he devoted part of his vacation to review my work as an ultimate gesture of comradery.

Dedication

This report is dedicated my partner Andrea. Between home-baked muffins and holding-down the home front while I was drowning in work, this work was only made possible through her continued love and support. Her incredible and unwavering care is only matched by her beauty.

1 Introduction / Context / Sensor / Aircraft Description

To set the context for the following study it is necessary to cover the background, motivation, and goals of this research.

1.1 Overview

A fixed-wing vertical take-off and landing (VTOL) unmanned aerial vehicle (UAV) will be used to conduct Magnetic Anomaly Detection (MAD) operations. The magnetic properties of the aircraft must be evaluated in order to integrate the MAD sensor payload in a suitable location. As many fundamental aircraft systems (i.e. propulsion and flight controls) create significant magnetic fields it is necessary to magnetically characterize these components. By understanding the vehicle's unique magnetic signature design decisions can be made to reduce the platform-generated magnetic noise.

This thesis begins with a brief review of airborne magnetometry and an outline of UAVs involved in magnetometry operations. Next, an overview of relevant magnetic field theory and material science is provided followed by a summary of common magnetic noise sources, organized into functional groups. A full description of the preparation, equipment and procedural considerations from the experimental characterization are provided. This serves the reader as an experimental campaign planning guide. During the experimental characterization campaign the aircraft's magnetic sources were identified and characterized.

These measurements were used to assemble all magnetic contributions into three magnetic models representing the aircraft geometry. MATLAB computational and COMSOL numerical static-field models were used to predict and visualize the magnetic fields around the aircraft. Also, Tolles and Lawson aeromagnetic compensation coefficients were computed to understand the effect of maneuver noise. These models were used to evaluate potential MAD sensor payload locations. The results indicated that the wingtips were the areas of lowest magnetic interference. Furthermore, many aircraft design and magnetic grooming recommendations were suggested.

1.2 Background & Motivation

The project "UAV Based Magnetic Anomaly Detection System for Remote Sensing" is a Natural Sciences and Engineering Research Council (NSERC) project to demonstrate an initial UAV-based MAD flight operations concept. The project was completed in collaboration with Defence Research and Development Canada (DRDC), CAE Inc, and the University of Victoria (UVic) Centre for Aerospace Research (CfAR), and was supported by National Research Council (NRC) Canada and Aeromagnetic Solutions Inc.

UAVs have become a vital facet of the defence and security portfolio for many military and civilian agencies. UAVs can provide a remote sensing capability in intelligence, surveillance and reconnaissance roles within terrestrial and maritime environments. This project mission profile will involve multiple UAVs conducting independent magnetic anomaly detection (MAD) searches. These searches will look for submerged metallic vehicles, will be based from a ship's helipad, and will be conducted in a maritime environment. Using MAD as a primary sensor, it becomes necessary to understand and minimize the amount of magnetic noise that the UAV platform produces so as to not interfere with the MAD sensors.

1.2.1 Airborne Magnetometry Operations

Scientists have long been interested in measuring the magnetic properties of the Earth. The first book of geomagnetism was published in 1600 [1]. The book encapsulated scientist curiosity, interest and discoveries as they studied the magnetic properties of the Earth. Centuries later mechanical devices called magnetometers were invented to measure the magnetic fields of objects and anomalies within Earth's geomagnetic field. At the turn of the 20th century magnetometer payloads were first integrated into aircraft operations. The first documented aeromagnetic survey flight was in Russia in 1936 [2]. The advent of the electronic magnetometer during the World War II led to the use of airborne magnetometry for the detection of submarines [3]. Many applications for manned airborne magnetometry have since emerged and in recent decades the use of unmanned aircraft have also been used to conduct airborne magnetometry.

1.2.1.1 Anti-Submarine Warfare

In a military context, airborne magnetometry is called magnetic anomaly detection (MAD); MAD operators search for anomalies in the Earth's magnetic field. In World War II, scalar fluxgate magnetometers were employed onboard anti-submarine warfare (ASW) aircraft to enhance the submarine detection capabilities and to protect Allied naval fleets [3]. Today, airborne ASW assets include manned fixed-wing airplanes and helicopters with limited emergence of ASW UAVs. In wartime conditions, there are five phases of an ASW scenario. The five phases of ASW are [4]:

1. Detection – A submerged object has been detected with a single sensor.
2. Classification – Multi-sensor information is used to judge what the object could be.
3. Localization – If classified a submarine, the target's accurate location is determined.
4. Tracking – Accurate location information is tracked over fixed time intervals, to determine the submarine's course and speed.
5. Attack – If necessary, a weapon solution is generated to eliminate the submarine threat.

ASW aircraft maintain various capability levels within all five phases. For example, the current state of ASW has UAVs primarily employed in detection, localization, and tracking roles, while manned ASW aircraft maintain capability in all five phases. MAD sensors are typically employed as a secondary sensor in the localization phase. However, with the strong decay of target magnetic fields ASW aircraft must fly at lower altitudes to enable detection. With the risk of low-flying aircraft altitudes alerting the submarine, MAD is most often reserved for later phases of ASW [4].

ASW fixed-wing (manned) aircraft like the Lockheed P3 Orion (Figure 1) have large payloads of weapons and sensors and an endurance up to 10 hours [4]. The MAD sensor on the Orion is mounted on a rigid tail boom, also known as a 'stinger boom.' This increases the distance from components that would cause magnetic interference.

Figure 1: P3 Orion ASW Aircraft: MAD Boom Annotated (Modified from [5])

Shipborne ASW (manned) helicopters like the Kaman SH-2G Super Seasprite (Figure 2) offer organic ASW attack capabilities to naval ships [4]. Although less common, ASW helicopters can carry MAD sensors, most often in a 'towed bird' configuration. While the towed bird configuration offers flexibility of mounting and unmounting the sensor quickly, the sway of the line introduces additional sources of noise while maneuvering [3].

Figure 2: SH-2G Super Seasprite ASW Helicopter: Towed MAD Annotated (Modified from [6])

The use of UAVs for ASW is still in its infancy. For example the MQ-8 Fire Scout, an unmanned autonomous helicopter, is said to have limited capability to detect surface submarines based on its secondary role as naval mine detector [7]. In 2015, the Brican TD100 UAV (Figure 3) had undergone magnetic grooming and subsequent flight tests [8], [9]. Its large wingspan lends well to a single wingtip MAD pod. However, to the knowledge of the author, there is no other similar-sized UAV using magnetometer that is capable of VTOL.

Figure 3: Brican TD100 UAV: Wingtip MAD Pods Annotated (Modified from [10])

1.2.1.2 Aeromagnetic Survey / Exploration

Earth's geomagnetic field is of interest to scientists. This magnetic field can be measured for geological studies with the use of ground-based, space-based, or airborne magnetometers.

Figure 4: Carleton-Sander GeoSurv II UAV: Wingtip Magnetometer Pods Annotated (Modified from [11])

Sander Geophysics Limited and Carleton University's GeoSurv II (Figure 4) aeromagnetic surveying UAV has dual wingtip magnetometer pods in a gradiometry configuration. Similar to the Brican TD100 UAV, large wingspans are an attractive configuration for aeromagnetic survey aircraft. Magnetic gradiometry compares the observed field strength values between two measurement points. Magnetic measurements can be made in a single pass by employing two magnetometers on a single aircraft, or in multiple equal-spaced passes by a single aircraft with one magnetometer [12]. Gradient-based changes in the magnetic field may outline geological boundaries of scientific interest [13].

1.2.2 Challenges of Designing and Building Airborne Magnetometry Aircraft

Mounting magnetometers on aircraft has always provided engineers a significant challenge. Being fundamental to flight, propulsion and flight controls systems all carry significant magnetic properties. Gas combustion engines, DC brushless motors and flight control servos all contain strong permanent magnets, electromagnetic windings, and ferromagnetic material. Since these systems cannot be removed it is necessary to mitigate their effects on magnetometer payloads, and ultimately the detection capabilities of the aircraft. Furthermore, material with strong magnetic properties can induce magnetisation in other materials. This is an important consideration regarding assembly and tooling. Tools that are magnetic or have become magnetized can in turnmagnetize fasteners or other aircraft parts they contact. Strong tool control and magnetic discipline are required as to prevent unintentional magnetic contamination.

1.2.3 Aircraft Description

The Nebula N1 UAV (Figure 5) was selected to accomplish the project objectives. The Nebula N1 is a custom-built UAV designed by Nebula Unmanned Aerial Vehicle Systems [14] and features a conventional high wing and T-tail configuration. Table 1 contains a series of parameters describing the aircraft.

Figure 5: Nebula N1 UAV: Conventional Configuration [14]

Table 1: Nebula N1 UAV Description: Conventional Configuration [14]

Parameter	Value
Wingspan	3.9 m
Length	2.0 m
MTOW	35 kg
Dash Speed	80 kn
Cruise Speed	50 kn

At the time of writing, the Nebula N1 was powered by an electric motor, pneumatically-launched then belly landed and had not yet integrated the VTOL systems. To accomplish the project objectives, the intent was to move towards hybrid-gas combustion with fixed-pylon vertical take-off and landing (VTOL) electric motors (Figure 6). The proposed configuration would enable the aircraft to lift vertically like a quadcopter and transition to forward flight. Once at steady level flight, the VTOL motors would become inactive and the aircraft would fly like a conventional fixed-wing aircraft using the gas combustion engine.

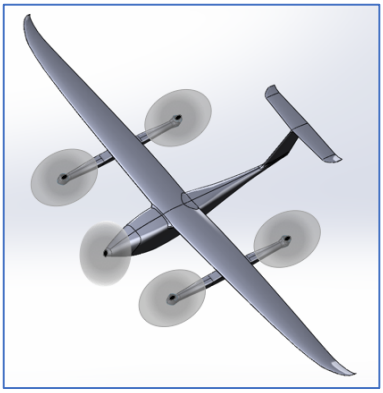

Figure 6: Nebula N1 UAV: Proposed VTOL Configuration [14]

Figure 7 displays the arrangement of internal components of the VTOL variant. Note that both gas combustion engine and electric motor components are shown. It was expected that both variants would be used throughout the project and aircraft development. The geometry of these components was studied for this report.

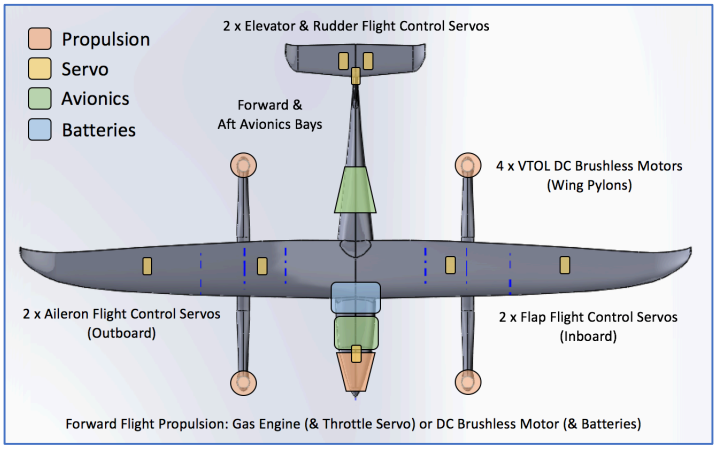

Figure 7: Nebula N1 UAV: Internal Components (Modified from [14])

1.2.4 Mission Profile

As visual description of the project objectives, Figure 8 outlines the VTOL UAV-MAD mission profile in an ocean environment. The intent is to launch multiple UAVs from a single ship. Each UAV would take off vertically from the ship helipad using its VTOL motors and then transition to forward flight. The UAV would dash to the search area at cruise altitude and descend to an appropriate magnetic search altitude. A coordinated multi-

UAV magnetic search would take place. Upon completion of the magnetic search, the UAVs would to the ship in a similar manner to the outboard leg.

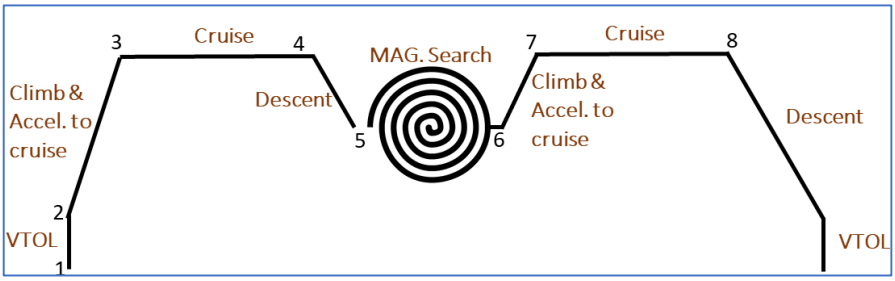

Figure 8: UAV-MAD Mission Profile [15]

There are many factors that affect the magnetic detection capabilities of the UAV. Various magnetic search patterns (type of search, resolution of grid) could be employed depending on the target characteristics (magnetic moment, size, depth), search platform characteristics (altitude, vehicle magnetic signature, magnetometer sensitivity) and environmental noise [16]. As an example, Figure 9 shows an example of a magnetic search technique whereby parallel legs (labelled primary transverses) are flown until an anomaly or deviation is observed. An orthogonal leg (labelled secondary transverse) is then flown to localize the detected object followed by confirmatory final transverse legs. In the case of ASW. these maneuvers are repeated to track the target as it moves and/or conducts evasive maneuvers.

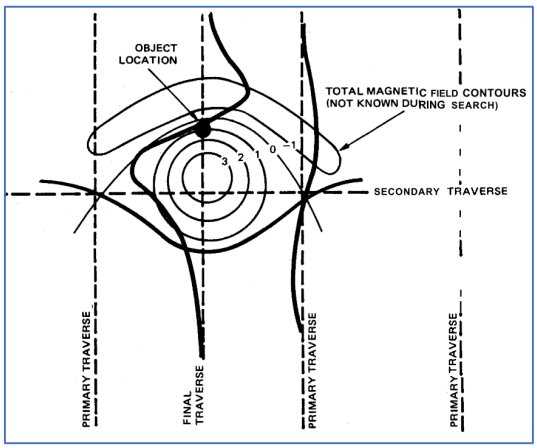

Figure 9: Magnetic Search: Typical Sequence of Traverses During Search Procedures [16]

Among the factors discussed, altitude is an importance operational decision. Given that the submerged targets could be at any depth, lower search altitudes increase chances of target detection. With flight safety in mind, it was assumed that the UAVs would be flown at much lower altitudes than manned aircraft. For reference, modern geomagnetic survey UAVs are being designed to operate at altitudes between 20 m (~ 65 ft) and 50 m (~160 ft)

while manned geomagnetic aircraft operate 250 m (~ 800 ft) and 300 m (~950 ft) [2], [17]. However, the lower the UAV flies, the more it could be affected by environmental noise, and in the maritime environment, ocean swell noise (discussed in section 2.2.3.2.2) could increase signal-to-noise ratios.

1.2.5 Payload Description

The CAE Inc MAD-XR (Extended Role) is a military-grade MAD sensor that is improved and miniaturized from the existing AN/ASQ-508A MAD sensors used by ASW aircraft around the world [18]. The MAD-XR sensor unit (Figure 10) combines a three-axis vector magnetometer with three scalar magnetometers in a splayed configuration to minimize dead zones (patent US 9,864,019). Table 2 contains a payload description of the MAD-XR Sensor Unit (MSU).

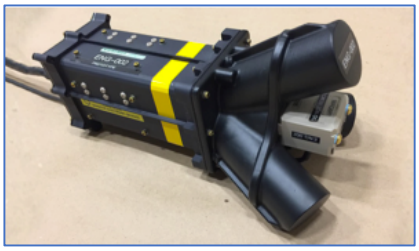

Figure 10: CAE MAD-XR Sensor Unit (MSU) [18]

The vector magnetometer senses the transverse, longitudinal and vertical components of Earth's geomagnetic field (input for compensation algorithms) while the scalar magnetometers detects relative spikes (anomalies) in the ambient magnetic field. In the ASW application, and depending on a variety of factors including the magnetic noise inherent to the platform on which it is installed, the MAD-XR system will generally detect anomalies at target ranges of approximately 1200 m (~ 4000 ft) [18]. The sensor unit also requires an interface unit onboard the aircraft (not shown in the figures or tables).

Table 2: MAD-XR MSU: Payload Description [18]

Parameter	Value
Length	24 cm
Diameter	15 cm
Weight	~ 1.1 kg

1.3 Research Objectives

There were three research objectives at the outset of this study. The primary objective of this study was to magnetically characterize the Nebula N1 UAV in support of the UAV-MAD project goals. An expected byproduct of this characterization was to explore and document experimental, computational, and numerical methods for UAV magnetic signature characterization. The secondary objective was to determine the most suitable position for the magnetometer payload. Finally, the third objective was to provide aircraft-specific design and magnetic grooming recommendations in an effort to reduce the aircraft magnetic signature.

1.4 Research Contributions

The research contributions generated from this study include:

1. An informative review of types of unwanted magnetic interference that can affect airborne magnetometry.
2. A comprehensive series of experimental procedures that enable the reader to completely characterize the magnetic properties of an unmanned vehicle. The thesis is structured such that it can serve as planning guide for any unmanned vehicle magnetic testing campaign.
3. A diverse set of visualizations to observe the magnetic interactions around the UAV. These tools can be used to study the placement of magnetometer payloads in various positions.
4. A consolidated list of aircraft design and magnetic grooming recommendations that can be applied to VTOL and non-VTOL UAVs.

1.5 Thesis Outline

There are four remaining chapters in this thesis. A brief description of the contents of subsequent chapters is provided below.

Chapter 2: Theory / Sources of Magnetic Interference / Design Considerations / Lit Review

The prerequisite physics of magnetic sources and theory required to understand the contents of this study are described. An outline of magnetic sources including moving and non-moving vehicle sources, sensor and environmental noise sources is included. Finally, a literary review of characterization strategies and levels of acceptable noise is presented.

Chapter 3: Experimental Methodology & Results

An introduction to magnetometry and magnetic measurement is presented. The process of planning and executing an experimental characterization campaign is described from a facilities, infrastructure and equipment perspective. Using magnetometer probes magnetic "hot-spots" are identified. Next, partial vehicle experiential procedures and results are discussed. Finally, the individual component characterization procedures and results are presented.

Chapter 4: Analytical & Computational Mapping/Analysis & Results

Collating the results of the individual component experiments, magnetic models of the Nebula N1 UAV are presented. An analytical framework is used to visualize the magnitude of the magnetic source parameters. A COMSOL framework is used to visualize and analyze the magnetic signature of the aircraft. Finally, Tolles and Lawson aeromagnetic compensation coefficients are computed and compared. Two potential MAD sensor locations are evaluated using these models.

Chapter 5: Conclusions and Recommendations

Major conclusions from the study and suggestions for future work are provided. Finally, an extensive list of aircraft design recommendations for low magnetic signature and for magnetic grooming is presented.

2 Theory / Sources of Magnetic Interference / Literature Review

This chapter establishes the theory and context for the magnetic testing and analysis. This chapter outlines relevant magnetic theory, defines sources of magnetic interference and provides a literary review of characterization strategies and levels of acceptable noise.

2.1 Magnetic Theory

Prior to discussing any type of magnetic characterization, it is first necessary to define key terms and establish a baseline understanding of magnetic theory. The purpose of this section is to define fundamental properties of magnetic fields and how we can represent them to accomplish our objectives.

2.1.1 Magnetic Fields

This section generally defines magnetism, total magnetic fields, and the mechanisms of magnetism.

2.1.1.1 Mechanisms of Magnetism

In general, there are two mechanisms of magnetism within physics: magnetic moments and moving electric charges (Figure 11). Magnetic fields are produced by either magnetic moments, being permanent magnetic or ferromagnets, or by moving charges within current-carrying conductors, being electromagnets or eddy-currents. Permanent magnets and ferromagnets maintain their remnant magnetism outside the influence of external fields, while electromagnets require moving electrons to produce magnetic fields [19].

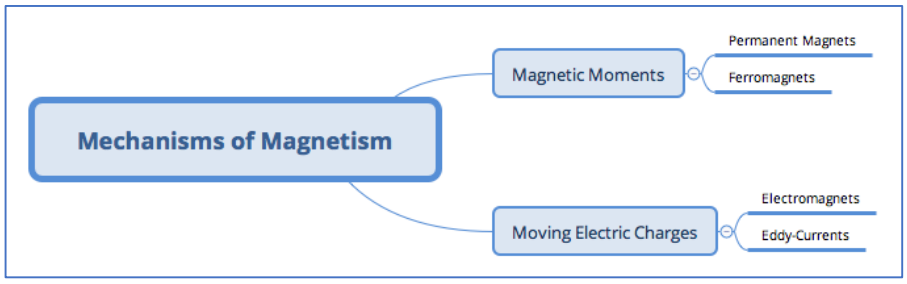

Figure 11: Flowchart for Mechanisms of Magnetism

2.1.1.2 Total Magnetic Field

Magnetic field lines are commonly drawn around magnetic sources to represent magnetic fields. Figure 12 illustrates the magnetic field lines around a permanent magnet and two electromagnets. Qualitatively, the strength of a magnetic field can be represented by the density of the magnetic field lines [20]. Magnetic field lines illustrate closed loops of equal field strength around a magnetic source.

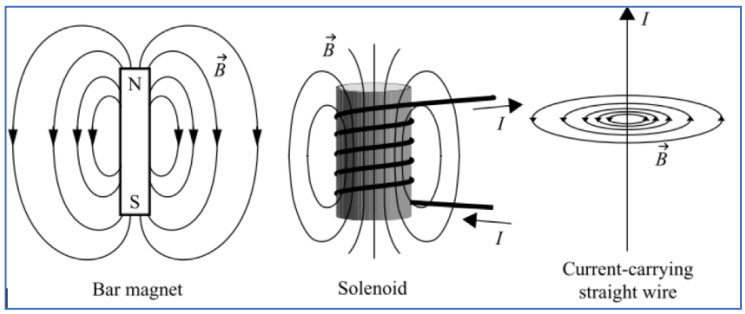

Figure 12: Examples of Magnetic Field Line Representations [21]

The magnetic field at any point in space is the vector sum of all magnetic field components at that point. More specifically, the principle of superposition applies to magnetic fields due to the linear nature of Laplace's equation [22].

2.1.2 Quantifying Magnetic Fields

Qualitative descriptions of magnetic fields do not the satisfy the need to design, optimize and exploit magnetic phenomenon for engineering purposes. This section defines the parameters used to quantify and compare magnetic materials and the fields that they produce.

2.1.2.1 Magnetic Flux Density (B) vs Magnetic Field Strength (H)

There are two parameters used to quantify a magnetic field – magnetic flux density *B*, with SI units of telsa [T] [1], and magnetic field strength *H*, with SI units of ampère per metre [A/m] [2]. In free space, there exists a linear relationship between magnetic flux density *B* and magnetic field strength *H* [19].

---

[1] Other units of magnetic flux density include weber per square meter [Wb/m^2], gamma [γ] and gauss [G] (non-SI unit) whereby 1 T = Wb/m^2, 1 nT = 1 γ and 1 T = 10,000 G.

[2] Other units of magnetic field intensity include newton per weber [N/Wb] and oersteds [Oe] (non-SI unit) whereby 1 A/m = 1 N/Wb and 1 Oe = 79.577 A/m.

$$B = \mu_o H$$

μ_0 is the magnetic permeability of free space, a fundamental constant that characterizes the response to a magnetic field within a non-magnetic vacuum. Assuming that air is non-magnetic, μ_0 may be used to describe magnetic fields on Earth [20]. Therefore, either magnetic field parameter (*B* or *H*) may be used for our purposes.

The choice of parameters depends on the specific application. Magnetic field strength *H* is commonly used to describe external coercive fields for magnetizing or demagnetizing materials. Magnetic flux density *B* is the widely accepted standard to represent a magnetic field as it provides a more complete description of the magnetic field (discussed further in 2.1.2.3) [19]. For the purposes of this study, all following mention of magnetic fields refer to magnetic flux density *B*.

2.1.2.2 Magnetic Fields: Orders of Magnitude

Figure 13 outlines relative orders of magnitudes of magnetic fields. In the context of airborne magnetometry, the typical working unit of magnetic fields is the nanotesla [nT] [3] yet the magnitude of Earth's geomagnetic field is many orders larger. For reference, the magnitude of Earth's geomagnetic field averages about 50 000 nT and geological anomalies encountered on aeromagnetic surveys can be on the order of 0.1 nT, or less [3]. In magnetic measurement, a significant portion of the signal recorded by the magnetometer is unrelated to the signal of interest [23].

[3] Recall that 1 nT = 10^{-9} T

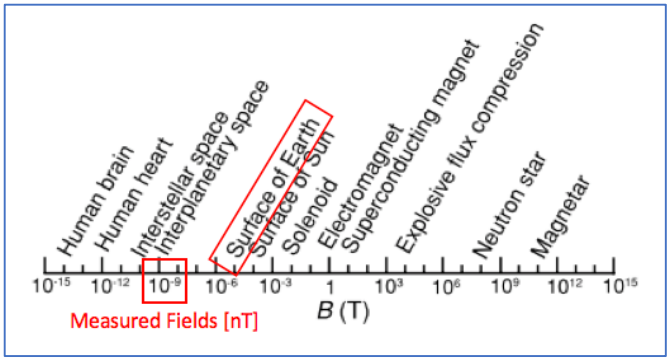

Figure 13: Order of Magnitudes: Magnetic Flux Density (Modified from [24])

2.1.2.3 Magnetization and Demagnetization

The magnetization moment vector *M,* with SI units of [A/m], is used to describe the internal magnetization within a material. *M* refers to the magnetic dipole moment m_i per unit volume *V* of material seen [19].

$$M = \frac{\sum m_i}{V}$$

Within a magnetized material, the volume *V* of the material contains enough elementary dipole moments m_i that *M* is non-zero. On the contrary, a demagnetized material has m_i values that mutually cancel so the *M* value is near to or equal to zero. For any magnetic material, the magnetic field can be described as a sum of internal magnetization $\mu_0 M$ and external field $\mu_0 H$ contributions [19].

$$B = \mu_o (H + M)$$

Figure 15 illustrates the internal magnetization (*M*) and external (*H*) field contributions to the total magnetic flux density *B*. This explains how permanent and ferromagnets will produce magnetic fields outside the influence of externally applied magnetic fields ($H = 0$). The nonmagnetic nature of free space prevents it from ever becoming magnetically saturated, independent of exposure level [25]

A fundamental property any ferromagnetic material is the irreversible nonlinear (and spontaneous) magnetization response to an external magnetic field [24]. Figure 14 shows the hysteresis loop of a ferromagnetic material.

Unique to each material (at a given temperature), the hysteresis loop summarizes the magnetization (and demagnetization) process within the microstructure (magnetic domains) of a ferromagnetic material, with an applied magnetic field H on the horizontal and the level of material magnetization M on the vertical. Note that H is conventionally used in lieu of B, for ease of demagnetization and is related to the difference in externally applied ($\mu_0 B$) and internal fields ($\mu_0 H$) contributions.

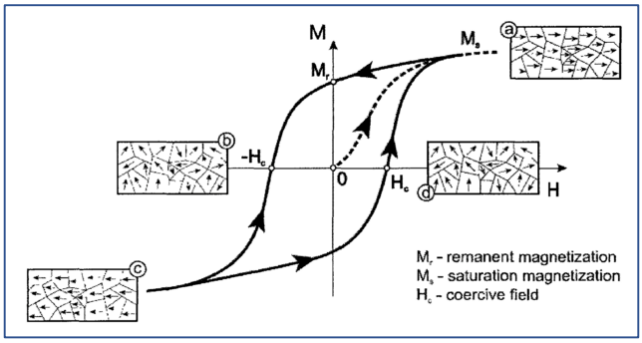

Figure 14: Example Hysteresis Curve [26]

Magnetization Process: In an un-magnetized state (state 0), the magnetic domains and electron spins are oriented such that there is no net magnetic field within the material. As the material is exposed to an external magnetic field H, the domains and electron spins align themselves as magnetization M increases until magnetic saturation M_s occurs (state a). In general, soft magnetic materials will be easily magnetized whereas hard materials are not.

Magnetic Saturation ($M = M_s$): Magnetic saturation M_s indicates the point to which an externally imposed magnetic field can no longer increase the state of magnetization of a material.

Remnant Magnetization ($M = M_r$): If the material is removed from the external field environment, a path from M_s to M_r will be taken. M_r is the remnant or residual magnetization contained within the microstructure of the material. This ferromagnetic material will now retain this order of magnetization, similar to a permanent magnet.

Conversely, the net magnetization order of a material can also be reduced ($M \rightarrow 0$) in an opposite process to magnetization. The mechanisms of demagnetization induce disorder

and randomness within the microstructure of the material. In general, soft magnetic materials will be easily demagnetized whereas hard materials are difficult to demagnetize. There are two methods of demagnetization explained below.

Demagnetizing the Material with Coercive Fields ± H_c: At saturation (M_s), if the material is exposed to a coercive field ± H_c, of opposite polarity (direction), it will decrease the amount of magnetization M within the material. Within Figure 14, a path from M_s to H_c or M_r to $-H_c$ would be taken. Upon completion, the microstructure of the material would be disoriented such that no net magnetic field is produced. This process is commonly referred to as degaussing.

Demagnetizing the Material with Curie Temperature T_c: Another way to demagnetize a material is related to the thermal-magnetic properties of the material. If heated to (at least) this Curie temperature then cooled within a magnetically–quiet or –silent environment, the atomic-level magnetic moments will orient themselves randomly yielding a low or zero net material magnetization [27].

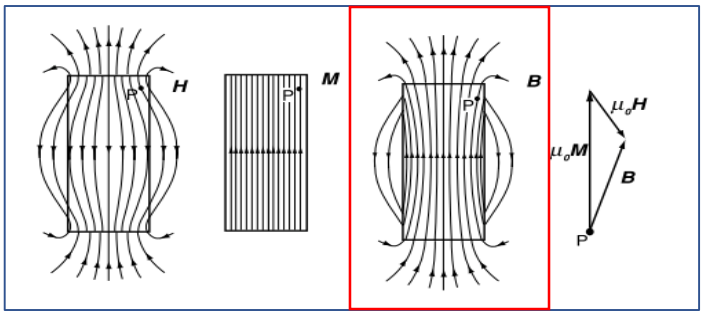

Figure 15: Distinguishing B, H and M within a Magnetized Bar Magnet [24]

2.1.3 Comparing Magnetic Material

This section compares describes the parameters used to compare magnetic materials.

2.1.3.1 Relative Magnetic Permeability (μ_r)

A key material property, magnetic permeability μ, characterizes the response of a material to an externally applied magnetic field. In mediums other than free space, the value of μ

will change with exposure to magnetizing forces, shown below for a linear, isotropic and homogeneous material [24].

$$B = \mu H \quad \text{or} \quad \mu = \frac{B}{H}$$

Relative magnetic permeability μ_r is a dimensionless quantity used to compare materials to a common baseline, μ_o.

$$\mu_r = \frac{\mu}{\mu_o}$$

For magnetic materials, unique curves like Figure 14 are published where the μ_r value can be extracted based on magnetic field exposure. $\mu_r > 1$ is exhibited for magnetic materials and $\mu_r = 1$ denotes a non-magnetic material. In ferromagnetic materials (discussed in section 2.1.3.3), the relationship between *B* and *H* is nonlinear and $\mu_r >> 1$ [20].

2.1.3.2 Magnetic Susceptibility ($\mathcal{X}$)

Another key material property, magnetic susceptibility $\mathcal{X}$, is a parameter used to describe the relationship between *M* and *H* within magnetic materials [24].

$$\mathcal{X} = \frac{M}{H}$$

Ferromagnetic materials are strongly attracted to ambient magnetic fields and therefore also carry large positive susceptibility values. Alternatively, there exists a simple relationship to the previously discussed relative permeability [19], [24].

$$\mu_r = \mathcal{X} + 1$$

Permeability is sometimes used in lieu of susceptibility when referring to soft magnetic materials due to their large μ_r values [24].

2.1.3.3 Ferromagnetic Material and Rare-Earth Magnets

Generally, magnetic materials are classified into hard and soft ferromagnetic material [19]. Permanent magnets fill the hard ferromagnetic category as they retain their magnetic properties over large time scales. Electromagnets fill the soft ferromagnetic category, as they do not retain magnetic properties and are used as temporary magnets. Generally, the harder the material, the stronger the magnet will be [28]. Examples of soft ferromagnetic material include iron, nickel-iron alloys, and low-carbon steels. Examples of hard materials

include Alnico (Al-Ni-Co) iron-alloys, high-carbon steels, and magnetite (iron oxide) [19], [24], [29].

Rare earth magnets are formed through natural metallurgical processes within the Earth. The mechanisms to create these magnets include large physical shocks to the material or remaining in a fixed orientation for significant periods within the Earth's geomagnetic field [28]. Thus, the magnetic history of a material is also a consideration as it can change over time.

2.1.3.4 Non-Magnetic Materials

Outside the realm of magnetic materials, the following materials are typically considered "non-magnetic": aluminum, austenitic stainless steel, brass, bronze, copper, gold, platinum, silver and most precious stones [28]. However, to be truly non-magnetic, the material would be unaffected by coercive magnetic fields (discussed in 2.1.2.3), non-conductive, and unable to attain a net magnetic moment. This is not the case for many of the above materials (see section 2.1.3.5). Examples of materials unaffected by coercive magnetic fields include: glass, rubber, plastic, and wood.

2.1.3.5 Electrically-Conductive Material

Electrically-conductive metals like aluminum and cooper can become magnetized under certain transient-field conditions despite being "non-magnetic" [30]. According to the Ampère-Maxwell Law, in the presence of AC currents (i.e. changing electric flux) a magnetic field will be induced within electrically-conductive material. Conversely, Faraday's Law of Electromagnetic Induction states that electrically-conductive material moving through a static magnetic field (a changing magnetic flux from the perspective of the moving material) induces an electric current coupled to its own magnetic field. Finally, Lenz' Law explains how eddy-current are then produced to oppose any change in observed magnetic flux.

2.1.4 The Magnetic Dipole

The magnetic dipole is an elementary magnetic quantity used to idealize and represent magnetic field sources.

A magnetic dipole can be thought of as an infinitely small bar magnet or a current-carrying loop. The dipole moment vector $\vec{m}$, with SI unit of ampère per metre squared [Am^2], is normal to the loop-plane in accordance with the 'right-hand rule' seen in Figure 16. Idealized magnetic dipole moments can be approximated using the relation below.

$$\vec{m} = I \cdot A$$

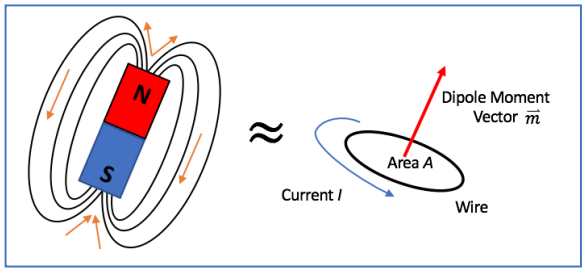

Figure 16: Representation of Magnetic Dipole Moment Vector

Magnetic dipoles moments can also be used to represent various magnetic field sources as seen in Figure 17.

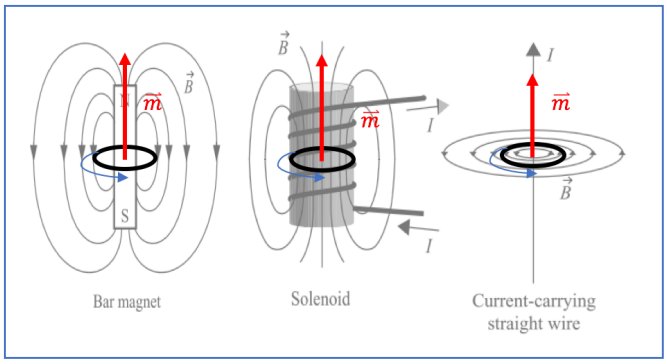

Figure 17: Representation of Magnetic Field Sources as Magnetic Dipoles (Modified from [21])

As an expansion of Gauss' Law, the magnetic field of an ideal magnetic dipole is given by the equation below [27].

$$\vec{B} = \frac{\mu_0}{4\pi}\left[\frac{3\,(\vec{m}\cdot\hat{r})\hat{r} - \vec{m}}{\|\vec{r}\|^3}\right]$$

Where $\vec{r}$ is the position vector from source to the observation point. Observe that the magnitude of the magnetic dipole field is proportional to the inverse cube of distance. As

$\vec{r}$ is increased, the magnetic field decays at a $\frac{1}{\vec{r}^3}$ rate. Alternatively, the dipole equation can also be expressed as a vector with components parallel to $\vec{m}$ and $\vec{r}$ [24], [31].

$$\vec{B} = \frac{\mu_0}{4\pi}\left[\frac{3\,(\vec{m}\cdot\hat{r})\hat{r}}{\vec{r}^5} - \frac{\vec{m}}{\vec{r}^3}\right]$$

Note the units in both of the above equations: B [T] and m [Am^2]. In the Cartesian coordinate system, the total magnetic dipole moment $\vec{m}_{total}$ may be described using *X-Y-Z* vector components $\vec{m}_{total} = \vec{m}_x + \vec{m}_y + \vec{m}_z$. Evidently, the scalar norm of the total dipole moment is $\|\vec{m}_{total}\| = \sqrt{\vec{m}_x{}^2 + \vec{m}_y{}^2 + \vec{m}_z{}^2}$. The ideal magnetic dipole can be further described using two vector components: permanent and induced magnetic dipole moments, $\vec{m}_{P\,i}$ and $\vec{m}_{I\,i}$, respectively. Each *X-Y-Z* vector component can be described as $\vec{m}_i = \vec{m}_{P\,i} + \vec{m}_{I\,i}$. The induced dipole moment can be further characterized as $\vec{m}_{I\,i} = \mathcal{X}_i * \vec{B}_{e\,i}$ whereby $\mathcal{X}_i$ is the volume directional susceptibility and $\vec{B}_{e\,i}$ is the vector component of Earth's geomagnetic field. Collectively, the total magnetic dipole is described with B_e [T] and m [Am^2] units below [8], [32].

$$\vec{m}_{total} = \left(\vec{m}_{P\,x} + \mathcal{X}_x * \vec{B}_{e\,x}\right)\hat{\imath} + \left(\vec{m}_{P\,y} + \mathcal{X}_y * \vec{B}_{e\,y}\right)\hat{\jmath} + \left(\vec{m}_{P\,z} + \mathcal{X}_z * \vec{B}_{e\,z}\right)\hat{k}\,.$$

2.2 Sources of Magnetic Interference

The purpose of this section is to apply magnetic theory to define the relevant sources of magnetic noise concerning UAVs involved in airborne magnetometry. For the purposes of this paper a magnetic noise source, is any unwanted magnetic field contribution sensed onboard. The noise can be either static or transient, and can pre-exist in the environment or be created by onboard systems or aircraft maneuvering. Magnetic noise has the effect of raising signal to noise ratios, reducing sensor sensitivity and decreasing detection ranges.

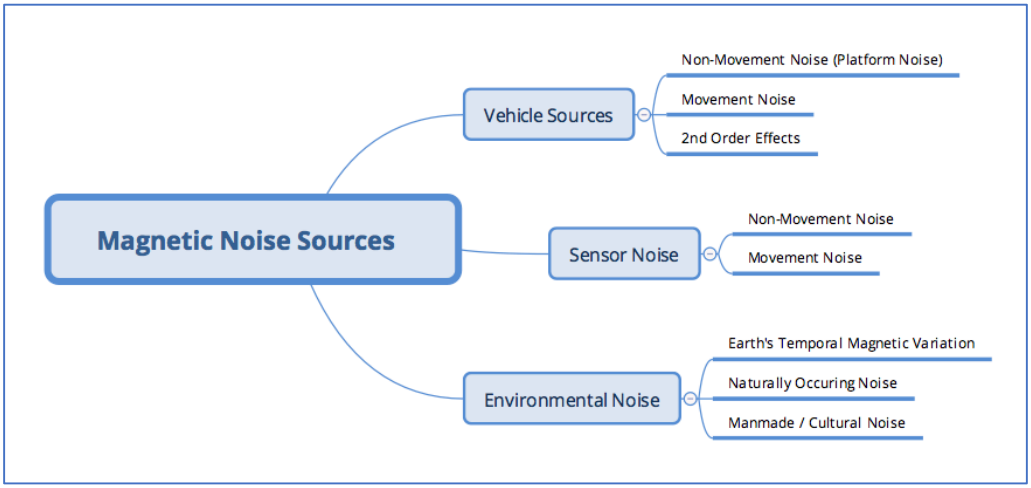

Figure 18: Mind Map Summary of Magnetic Noise Sources

Recall from Figure 11 that the sources of magnetism include permanent magnets, ferromagnets, electromagnets, and eddy-currents. Figure 18 further refines and expands that list to include all sources of magnetic noise that an airborne operation could experience. For the purposes of this paper, magnetic noise sources will be divided into three branches: vehicle noise sources, sensor noise sources and environmental noise sources. The following sections define the magnetic noise branches seen in Figure 18. The full mind map with all magnetic noise branches defined can be found in Appendix E.

2.2.1 Vehicle Sources

In this magnetometry context, the term ‘magnetic signature’ refers to the amount of (unwanted) magnetic noise generated by magnetic sources onboard the vehicle, whereby the accuracy of the magnetic data obtained in flight is highly dependent on the vehicle magnetic signature. The magnetic signature of the vehicle directly affects the detection capabilities and subsequent mission effectiveness of the platform. Vehicles sources of magnetic noise (Figure 19) include non-movement sources (static and transient sources of noise produced by onboard systems), movement noise (rigid and flexible vehicle motion, rotating components) and second order effects to all the above. The following sections classify and describe these sub-categories.

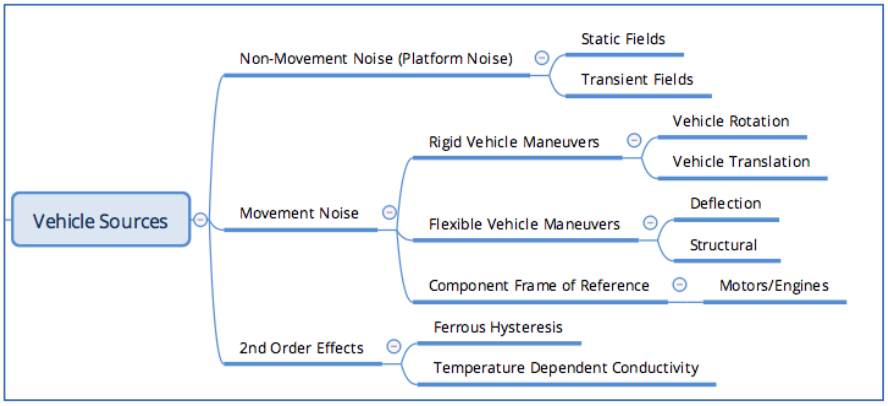

Figure 19: Flow Chart Excerpt: Summary of Vehicle Sources

2.2.1.1 Non-Movement (Platform) Noise

Non-movement noise, also known as platform noise, includes the static and transient sources of noise produced by onboard systems and components. Non-movement noise can be framed as the total magnetic noise produced by the aircraft sitting on the ground with or without electrical power applied. In Figure 20, static field sources include permanent magnets and DC electromagnetics (i.e. steady DC currents) while transient sources include those with changing electric flux (i.e. AC currents, load-dependent devices). Non-movement noise does not include the transient noise produced by motors or engines while running, which is covered in 2.2.1.4.3.

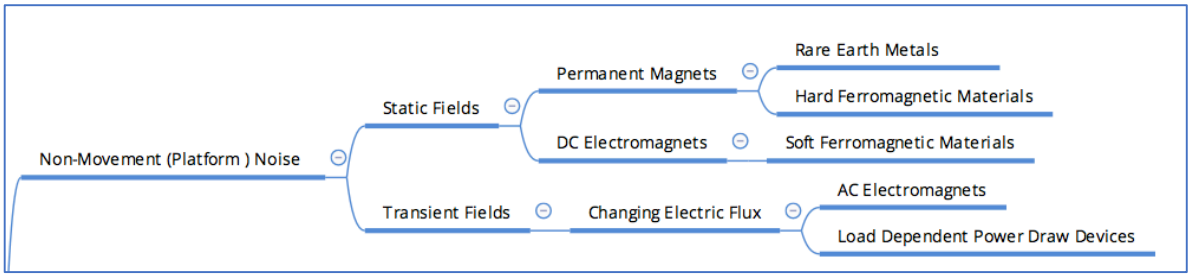

Figure 20: Flow Chart Excerpt: Summary of Non-Movement (Platform) Noise

2.2.1.2 Static Fields

A static magnetic field refers to a magnetic field source that does not vary with time. Static magnetic field sources do not change with time and maintain constant magnetic flux values, unlike transient magnetic sources. While static magnetic fields can be produced by moving charges, as in current-carrying wire, permanent magnets produce static magnetic fields without currents.

2.2.1.2.1 Permanent Magnets and Hard Ferromagnetic Material

Permanent magnets make up large portions of vehicle magnetic signatures. Having a net magnetic polarization, permanent magnet and ferromagnetic sources within the vehicle, will shape the ambient magnetic field around the vehicle as it changes direction (heading). Rare earth metals generally produce permanent magnets while ferritic stainless steels produce ferromagnets.

Following the discussion of hard ferromagnetic and rare-earth materials discussion in **2.1.3.3**, it may be evident that there are several permanent magnet sources aboard aircraft. The most well-known sources of static onboard vehicle noise come from the propulsion and flight control servos when inactive [2], [8], [13], [33]–[36]. Combustion engines, electric motor/generators and servos all contain permanent magnets and ferromagnets that contribute to the vehicles magnetic noise level. Furthermore, it is common to use a magnetic safety shunt to ensure the vehicle's propulsion or electrical system remains inactive until deliberately removed [8], [23], [35]–[37].

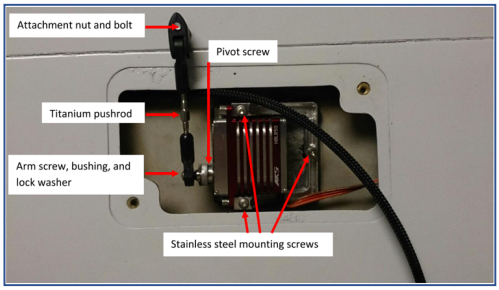

Figure 21: Servo Assembly on Brican TD100 UAV: Ferromagnetic Material Annotated [8]

Furthermore, assorted vehicle fasteners and attachment hardware are commonly made from ferromagnetic material. As an example, Figure 21 shows the flight control servo assembly of a similar UAV. The figure annotates the various ferromagnetic hardware components that were identified as having detectable magnetic fields. These identified sources would need to be replaced or demagnetized. Table 3 provides more examples of permanent magnet and hard ferromagnetic sources.

2.2.1.2.2 DC Electromagnets

Electrical currents induce magnetic fields. Electromagnets, in general, can be considered weak permanent magnets [24]. This classification does not include load-dependent devices. The obvious source of DC electromagnetic noise on aircraft is the extensive amount of

straight, looped (solenoids) and toroid-shaped wires throughout. Electrical wires typically reach all regions of the vehicle but remain most concentrated within avionics or sensor bays. Further sources of noise could be found near the battery compartments. As DC electrical sources, batteries can also produce static magnetic noise from a parasitic current draw, even when the connected components are powered-off. An example of parasitic power draw noise can be found in unmanned ground vehicle testing done in [37]. Moreover, any other conductive material that comes into contact current-carrying sources will also become a source of static magnetic noise. Table 3 provides more examples of electromagnet sources.

Table 3: Summary of Static Noise Source UAV Examples

Permanent + Ferro Magnets	**DC Electromagnets**

• (Inactive) Servos
  • Internal Gears, Actuator PMs
• (Inactive) Combustion Engines
  • Crankshaft, Connecting Rod, Hall Effect RPM Sensors
  • Ferromagnetic Casing
• (Inactive) Electric Motor/Gen
  • Internal PMs, Ferromagnets
  • Ferromagnetic Casing
• Assorted Hardware
  • Ferritic Stainless Steel
  • Screws, Nuts, Lock-Washers, Bushings, Bolts, Springs
• Magnetic Kill-Switches
	• Conductors that carry/touch DC current
	• Battery
	  • DC Current, Parasitic Draw, Metal Jackets
	• (Powered) Wiring Harnesses
	• (Active) Spark Plugs
	• (Powered) Position/Speed Control Electronics

2.2.1.3 Transient Fields

A transient magnetic field is a magnetic field source that varies with time. Transient magnetic sources include changes in electric and magnetic fluxes (Ampère-Maxwell and Faraday's laws, respectively). This section only considers only magnetic sources produced by changing electric flux as changing magnetic flux is covered in section 2.2.1.4.3. Variable (AC) currents produce variable transient magnetic fields.

2.2.1.3.1 Changing Electric Flux

Ampère-Maxwell law states that a constant current or changing electric flux induces a magnetic field. Given the large amount of AC-powered or load-dependent electronics within a vehicle, many sources of transient magnetic noise can be identified. Examples of

AC-powered electronics include inverters, transformer rectifier units (TRU) and RF transmitters and examples of variable-draw electronics include autopilot, flight control, and throttle servos. The latter of the two can be compensated using techniques for in [38]. Table 4 provides more examples of sources with changing electric flux.

Table 4: Summary of Transient Noise Source UAV Examples

Changing Electric Flux	Changing Magnetic Flux

• Anything carries/touches AC current
• Inverters / TRU / DC-DC
• (Powered) AC Wiring Harnesses
• (Powered) Position/Speed Control Electronics
• (Powered) Autopilot
• Assorted Avionics / Sensors
• RF Transmitters
	• Movement Noise
	  • Rigid Vehicle Induced Noise
	  • Rigid Vehicle Eddy Noise
	  • Rigid Vehicle Buffeting Noise
	  • Flexible Vehicle Noise
	• (Active) Servos
	  • Rotating PMs
	• (Active) Combustion Engines
	  • Rotating PMs, Hall Effect RPM Sensors
	• (Active) Electric Motor/Gen
	  • Rotating PMs

2.2.1.3.2 Note on Ferromagnetic Material

The magnetic properties of ferromagnetic material can change over time with exposure to coercive magnetic fields. This suggests that ferromagnetic material is a transient source, since the properties vary with time (and exposure). Ferromagnetic hulls of naval ships are often considered a transient source as degaussing is employed to reduce threat of magnetically-fused undersea mines [30], [39]. For the purposes of this study, it was assumed that all ferromagnetic sources were static-field sources for the duration of magnetic and subsequent flight testing.

2.2.1.4 Movement Noise & Changing Magnetic Flux

Movement noise is an important consideration in airborne applications. Aircraft translation and maneuvers within Earth's geomagnetic field produce various magnetic fields on the aircraft. Intuitively, all forms of movement noise produce transient magnetic noise signatures. Figure 22 summarizes the aspects of vehicle movement noise. Movement noise includes rigid vehicle maneuvers (changes in pitch, roll and yaw) along with translations through ambient magnetic field gradients, flexible vehicle structural flexing and control surface deflections, and components that rotate within their own frame of reference. Table 4 also provides more examples of sources with changing magnetic flux.

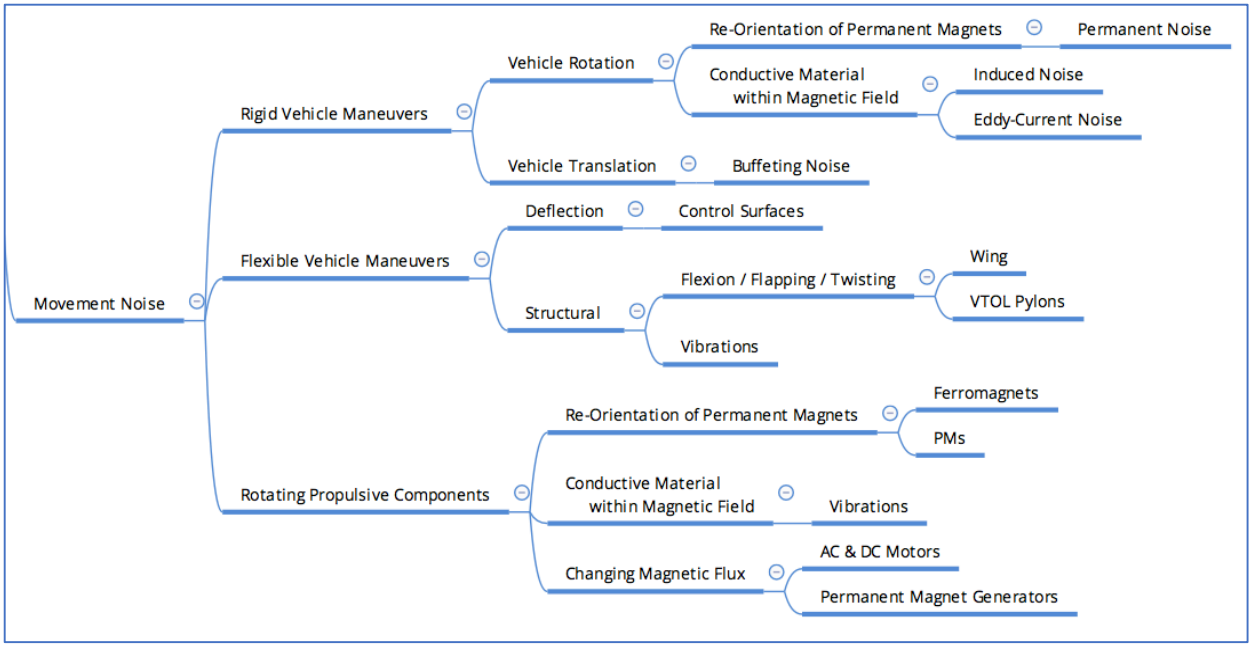

Figure 22: Flow Chart Excerpt: Summary of Movement Noise

2.2.1.4.1 Rigid Vehicle Maneuvering

The most dynamics sources of noise sources are those caused by vehicle motion. Movement noise is produced by rotational attitude changes in pitch, roll, and yaw along with vertical changes in altitude within Earth's geomagnetic field. The three rotational noise sources are permanent noise, induced noise, and eddy-current noise [40]–[42], summarized in Table 5.

Table 5: Summary of Rigid Vehicle Rotational Maneuver Noise Mechanisms

Airborne Noise	**Explanation of Magnetic Noise**		**Magnetic Mechanism**
	Action	**Result**	
Permanent	Reorientation of Perm and Ferromagnets within Geomagnetic Field	Magnetic Interactions Re-Shape the Aircraft Permanent Magnetic Field	Gauss' Law of Magnetics
Induced	Rotation of Soft Ferromagnetic or Conductive Material within Geomagnetic Field	Material Observes a Changing Magnetic Flux and Produces Induced Currents	Faraday's Law of Electromagnetic Induction
Eddy-current	Material Observes a Changing Magnetic Flux and Produces Induced Currents	Eddy-Current Produced to Oppose the Change in Observed Magnetic Flux	Lenz' Law

The permanent field sources of the aircraft interact instantaneously with Earth's geomagnetic field as the aircraft changes orientation in 3D space. As the vehicle maneuvers

throughout Earth's geomagnetic field, the vehicle observes changes in magnetic flux. Aircraft maneuvers produce electrical currents within metallic parts of an aircraft. These currents have a magnitude proportional to the time rate of change in magnetic flux [41]. Thus, the induced and eddy-current noise effects are proportional to the time-dependent pitch, roll and yaw maneuvers.

Table 6: Summary of Rigid Vehicle Translation Maneuver Noise Mechanisms

Airborne Noise	Explanation of Magnetic Noise		Magnetic Mechanism
	Action	Result	
Buffeting	Translation of Soft Ferromagnetic or Conductive Material within Geomagnetic Field	Material Observes a Changing Magnetic Flux and Produces Induced Currents	Faraday's Law of Electromagnetic Induction
Eddy-current	Material Observes a Changing Magnetic Flux and Produces Induced Currents	Eddy-Current Produced to Oppose the Change in Observed Magnetic Flux	Lenz' Law

Similar to the induced and eddy-current effects experienced in rigid-body flight, turbulent perturbations experienced in flight combined with vertical magnetic gradients cause buffeting noise, see Table 6 [9], [43], [44]. Subtle changes in aircraft pitch (and altitude) due to aerodynamic and meteorological factors increase the observed changes in magnetic flux and subsequent magnetic noise. Buffeting noise assumes that the aircraft is a rigid body and does not take wing flexion into account [32]. Similar to induced movement noise, buffeting noise follows Faraday's law, which does not depend on the total amount of magnetic flux through the aircraft surfaces but rather it depends only on how fast the flux changes [21]. Using IGRF data to estimate a local vertical gradient [nT/m] and autopilot data from flight tests, an estimate of buffeting noise can be obtained [9], [44].

2.2.1.4.2 Flexible Vehicle Maneuvering

One area of research that is not well established is the magnetic noise associated with flexible vehicles. As the vehicle shape changes in flight, the associated induced magnetic noise effects will also change. Flexible vehicle noise in this case includes deflections of control surfaces, structural flexion (i.e. wing flexion) and vibrations.

For example, as the control surfaces on aircraft deflect, the angle of those surfaces change relative to the rigid vehicle. Further burrowing into Faraday's law, it is a changing magnetic

flux normal to the surface (of investigation) that produces induced currents (and subsequent magnetic noise) [21]. In the case of the Nebula N1, the control surfaces are made of carbon fibre so it is forecasted that the deflecting control surfaces could induce further maneuver noise.

Wing flexion is prevalent of modern high efficiency and high aspect ratio wings – UAVs included. As the aircraft is exposed to aerodynamic or meteorological forces, the fuselage and payload weight will cause the wings to respond elastically to the flight loads. Relative movement among permeant magnet and induced sources will also produce transient noise. Wing flexion or torsion is particularly concerning for wing-mounted magnetometer configurations, as in [17] whereby vertical magnetic gradient targets were established for a small geomagnetic survey UAV. In the case of the VTOL-variant of the Nebula N1, the fixed-pylon VTOL pods could also flex and twist in-flight producing similar noise. It has been suggested by [32] that one could model wing flexion noise in terms of the pitch angle or potentially the derivative of the pitch angle.

Finally, any type of vibration on the vehicle causing relative motion between sources would also negatively affect sensor performance. In most aircraft, and most notably rotary-wing aircraft, vibration isolation mechanisms are applied to reduce material fatigue. Reducing structural vibrations associated with propulsive systems is of primary concern, especially when propulsive systems are known to be significant magnetic noise sources.

2.2.1.4.3 Rotating Propulsive Components

Within the rigid and flexible vehicle frames of reference, there are propulsive components that rotate internally which produce significant transient magnetic noise. Generally, electric engines have been found to produce more magnetic noise than combustion engines in airborne UAV magnetometry applications [2], [45].

DC brushless motors are the most common for UAV propulsion. They are selected for their low weight, reliability and suitability for high-speed flight [24]. Figure 23 is a simple illustration of the internal components of such a motor. The motor has a permanent magnet

(PM) rotor surrounding a stator composed of a series of coil-pairs which act as electromagnets (EM). When DC voltage is passed through the coil-pairs, a magnetic field is produced (Ampère's circuital law) which interacts with the PM rotor. As like poles repel, the rotor begins to rotate away from the coil-pairs as they are selectively sequenced to induce rotary motion.

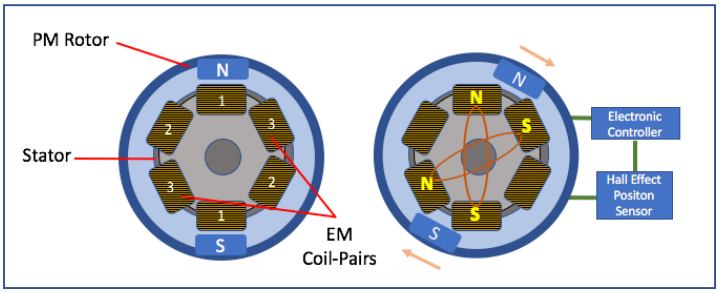

Figure 23: Components and Operation of a Brushless DC Motor

The magnetic noise consequences of this rotary motion produce a significant amount of changing magnetic flux noise. The changing magnetic flux has the effect of inducing currents in surrounding conductive surfaces, which then produce their own magnetic fields (Biot-Savart law) and eddy-currents (Lenz' law). A similar situation occurs in other types of electric engines. Flight control servos commonly include brushed DC motors. Table 7 broadly summarizes the configuration of other types of electric motors sorted according by magnetic components: EM and PM.

Table 7: Comparison of Electric Engine Rotor/Static Components

	Stator	**Rotor**
Brushed DC Motor	PM	EM
Brushless DC Motor	EM	PM
AC Induction Motor	EM	EM

Similarly, combustion engines are also significant magnetic noise sources. It is common that crankshaft, pistons, cam valve pins and connecting rods made of high ferritic steels. Moreover, permanent magnetic generators are commonly included to power key aircraft or payload support systems. The above internal components of gas combustions engines produce a similar set of permanent, induced, vibrational and eddy-current movement noise.

2.2.2 Sensor Integration Noise

While the magnetometer design is not part of this thesis, it is of value to briefly cover some potential sources of noise associated with scalar magnetometer integration. Figure 24

summarizes the identified sources of sensor integration which include movement and non-movement sources of noise or errors in data collection.

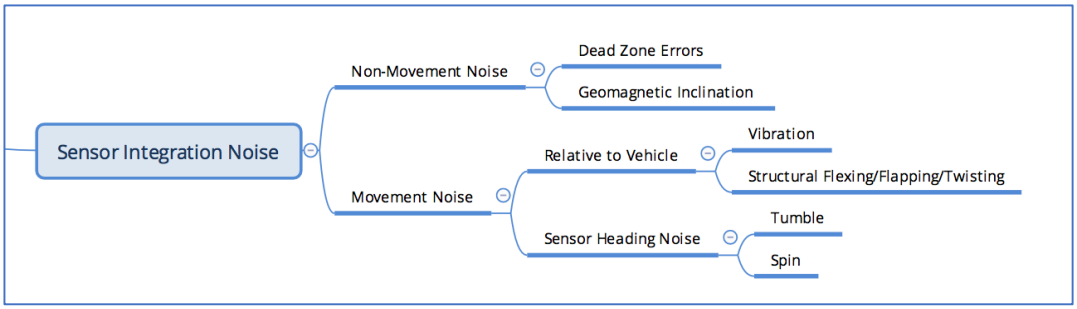

Figure 24: Flow Chart Excerpt: Summary of Sensor Noise

2.2.2.1 Non-Movement Noise

The alignment of scalar magnetometer is an important design consideration. Knowledge of magnetometer limitations such a sensor heading error, drift, and dead zones are critical to successful mission completion [23]. In general, a single-axis optically pumped (scalar) magnetometer measures and meters the light-controlled opacity of a gaseous vapour, in a process that is proportional to variations in magnetic field [3]. These types of magnetometers cannot measure magnetic fields within 30 degrees of their optical axis, called 'dead zones' [3]. Attention must be placed on aligning magnetometers payloads in orientations to minimize exposure to dead zones or outside the local geomagnetic inclination. In the case of the MAD-XR, the splayed configuration of three magnetometers mentioned in section 1.2.5 minimizes dead zones.

2.2.2.2 Movement Noise

The following sections outline the potential errors and noise involved in sensor integration.

2.2.2.2.1 Relative to Vehicle

Similar to section 2.2.1.4.2, relative movement between the magnetometer and any magnetic sources would cause magnetic noise. Most prominent in towed magnetometer configurations, many positional error and induced effects can reduce sensor performance. Although less prominent, flexion or twisting of stinger booms through turbulent flow would also produce magnetic noise. In the case of a MAD payload mounted on the wingtip,

wing flexion would create transient changes in the magnetic flux. Furthermore, any flexion of the VTOL pylons in flight would produce magnetic noise on wingtip-mounted MAD payloads on the Nebula N1. The same is true for any type of relative vibration between the airframe and MAD payload.

2.2.2.2.2 Heading Noise

Related to the dead zones of single-axis scalar magnetometers, spin and tumble errors can occur through dynamic maneuvering. As the aircraft pitches, rolls and yaws the optical axis will pass towards and away from the target of interest. Tumble refers to the interruption of magnetic measurement as the sensor rotates about a lateral axis. Spin refers to the interruption of magnetic measurement as the sensor rotates about a longitudinal axis. Tumble and spin errors require specific modelling considerations as to not skew affect measurement results [32].

2.2.3 Environmental / Ambient Noise

A large consideration in all magnetic studies is the interaction of local magnetic sources and the surrounding magnetic environment. In this study, the surrounding environment will be described in three categories (Figure 25): Earth's geomagnetic field (2.2.3.1), naturally-occurring noise sources (2.2.3.2) and manmade (cultural) noise sources (2.2.3.3).

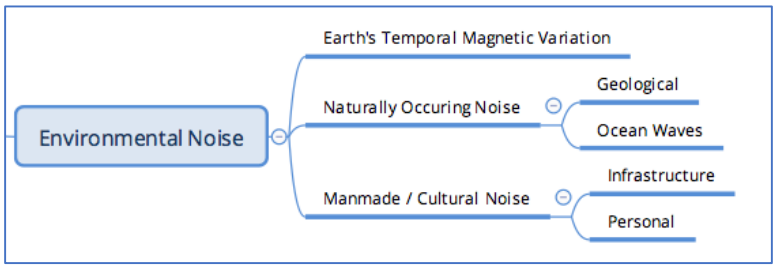

Figure 25: Flow Chart Excerpt: Summary of Environmental Noise

2.2.3.1 Earth's Temporal Magnetic Field Noise

Changes deep within Earth's liquid interior drive local and large-scale variations within the Earth's geomagnetic field [1]. The magnitude of these variations can be anywhere between 20 000 and 70 000 nT with local variations of up to several hundred nT [3]. Commonly, Earth is described as a large bar magnet (Figure 26). However, this is not entirely accurate.

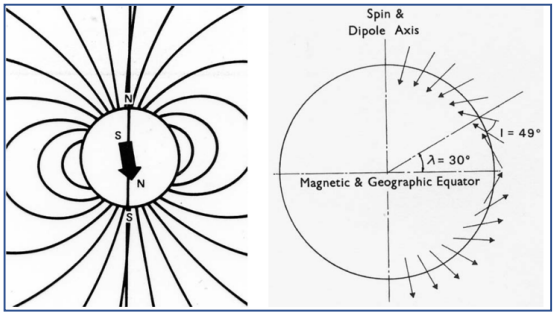

Figure 26: Earth's Dipolar Magnetic Field [3]

The reality is that Earth's geomagnetic field is very complex. The interaction between Earth and the sun combined with Earth's daily rotation leads to a variation in the amount of charged particles, known as solar wind, influencing Earth's ionosphere (see Figure 27) [3]. As Earth rotates, the solar wind causes instability in Earth's magnetosphere for daytime observers and stable conditions at night. This daily cycle in magnetic stability is also known as diurnal variation.

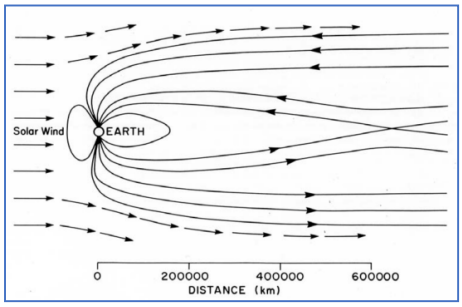

Figure 27: Solar Wind and the Earth's Ionosphere [3]

Most significant diurnal effects are observed at noon with daily amplitude variations as high as 50 nT [3]. Higher levels of sunspot activity or magnetic storms can lead to drastic variations (hundreds of nT) on Earth [3]. Figure 28 shows an example of this geomagnetic complexity.

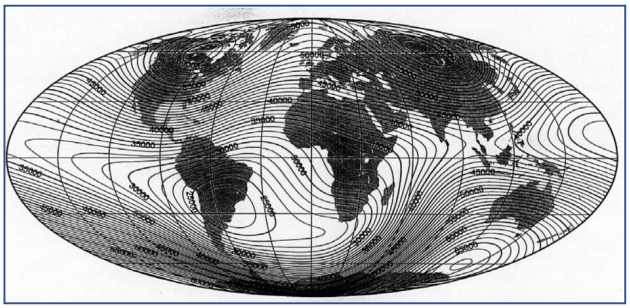

Figure 28: IGRF Map of Earth's Complex Geomagnetic Field [3]

Given these temporal effects on Earth, a worldwide observatory system has been established. Using spatially separated observations around the world, a mathematical model of Earth's predicted geomagnetic field is published [3]. The International Geomagnetic Reference Field (IGRF) allows scientists to account for and subtract temporal effects from magnetic measurements in post-processing. The IGRF model can predict the ambient field characteristics at any point on Earth. Typically 99% of the measured value is removed when IGRF is subtracted [3]. Moreover, geomagnetic anomalies are usually at least two orders of magnitude smaller than the magnitude of the total magnetic field measured [3].

2.2.3.2 Naturally Occurring Noise (Environmental)

With geological diversity around the world there are significant magnetic field contributions that need to be considered when entering new regions. For instance, the significance of regional magnetism can be felt in central Brazil where recorded anomalies have been seen to exceed 50 000 nT (where the local geomagnetic field is only 23 000 nT) [3].

2.2.3.2.1 Regional Geology Noise

Geological sources can produce significant magnetic anomalies, with notable sources being metamorphic rocks, igneous and plutonic rocks, hypabyssal rocks, banded iron formations, and ore bodies [3]. Generally, sedimentary rocks are assumed to be non-magnetic, provided the sediment does not contain iron or metavolcanic deposits [3]. One must pay particular attention near continental shelves, where igneous or volcanic rocks typically lie beneath the non-magnetic sedimentary layers [28]. Other environmental materials considered to be non-magnetic include sand, silt, mud, coral, and pure water [28].

2.2.3.2.2 Ocean Swell Noise

While pure water is considered non-magnetic, salted sea water is electrically-conductive. As the ocean swells vertically within the Earth's geomagnetic field a magnetic field commonly known as "swell noise" is produced [28], [46]. The magnitude of swell noise is proportional to the amplitude, direction, and velocity of the swell and the distance from measurement [28]. Swell noise can be overcome in airborne applications simply by flying

higher. However in undersea autonomous undersea vehicle applications, the conductive nature of sea water causes an additional source of noise as it passed over the body of the vehicle [35]. Figure 29 shows examples of ambient magnetic fields associated with the ocean environment.

Magnetic Sources	Magnitude (nT)	Frequency or period
Earth's core	$\sim 32000 - 62000$	$\sim$ DC
M2 lunar tide	~ 1	12.42 hours
Solar ionospheric tide	~ 5	12 hours
Ocean swells	~ 0.1	$0.04 - 0.08$ Hz
Seismic activity	$\sim 0.02 - 0.2$	$0.001 - 0.1$ Hz
Schumann resonances	~ 0.001	$8, 14, 20, 26, 32, 37, 43$ Hz

Figure 29: Magnitudes of Ambient Magnetic Fields Associated with the Ocean [47]

2.2.3.3 Manmade (Cultural) Noise

Manmade and cultural noise sources surround us and have significant variation in magnetic field contribution. These objects would include any nearby object composed of ferromagnetic, permanent magnets, or electromagnets with static or transient fields. This section briefly covers a few examples of cultural and personal sources of noise for demonstrations. This section is not meant to be exhaustive.

On land, there are many large sources that can cause cultural noise. Notable static field sources of cultural noise include buried pipelines, steel telephone lines, manhole covers, water pipes, rebar-reinforced, and magnetic concrete buildings or tunnels. Large transient field sources of cultural noise include nearby aircraft, trains, cars, and transmission lines. Similarly, on the sea there are also sources of cultural noise. Shipwrecks, submerged pipelines, anchored chains, and oil-drilling platforms are all examples of static field sources. Finally, one must also consider transient-field sources at sea which include: floating buoys, saltwater pipelines, submarines, and steel-hulled ships. Figure 30 summarizes the relative magnitude of various manmade noise sources.

Magnetic Anomalies of Common Objects

Object	Typical Maximum Anomaly	
	Near Distance	Far Distance
Ship (1,000 tons)	30 m (100 feet) 300 to 2000 gammas	300 m (1,000 feet) 0.3 to 2.0 gammas
Anchor (20 tons)	15 m (50 feet) 200 to 650 gammas	30 m (100 feet) 25 to 80 gammas
Light aircraft	6 m (20 feet) 10 to 30 gammas	15 m (50 feet) 0.5 to 2 gammas
Pipeline-30 cm (12 in.) dia.	8 m (25 feet) 50 to 200 gammas	15 m (50 feet) 12 to 50 gammas
Pipeline-15 cm (6 in.) dia.	3 m (10 feet) 100 to 400 gammas	15 m (50 feet) 4 to 16 gammas
DC Electric Train	150 m (500 feet) 5 to 200 gammas	300 m (1,000 feet) 1 to 50 gammas
cm dia.x 25 cm long) (2 in. dia. x 10 in. long)	6 m (20 feet) 60 to 200 gammas	30 m (100 feet) 0.5 to 1.5 gammas
Well casing and wellhead	15 m (50 feet) 200 to 500 gammas	150 m (500 feet) 2 to 5 gammas
Automobile (1 ton)	10 m (30 feet) 40 gammas	30 m (100 feet)

Figure 30: Relative Magnitude of Various Objects[4] [28]

While large sources can be obvious, small personally-sized items can also affect magnetic measurement results. Figure 31 lists a series of magnetic objects and the distance at which a magnetic field of 1 nT is produced. Strong adherence to personal magnetic discipline is necessary for any type of magnetic measurement campaign.

Object	r_i [m]
Safety pin	1
Buckle of belt	1
Watch	1
Metallic pen	1
Knife	2
Screwdriver	2
Revolver	3
Hammer	4
Spade	5
Rifle	7
Bicycle	7
Motor cycle	20
Car	40
Bus	80

Figure 31: Magnetic Fields (of nT) of Everyday Objects and Distance [1], [48]

2.3 Literature Review

The following summarizes some of the literature reviewed while preparing for this study. Other sections of the thesis contain literary reviews, where applicable.

2.3.1 Acceptable Levels of Total-Field Noise

While there were no explicit magnetic field requirements for this project, a survey of acceptable magnetic noise levels was conducted. Note that the scope of this survey did not

[4] Note that 1 gamma [γ] = 1 nT

include vertical or horizontal gradiometry. In general, the magnetic design requirements for gradient measurements are more strict than those for total-field measurements [49]. Most of the published information regarding magnetic total-field noise levels come from geomagnetic survey. In Canada, there are published geomagnetic survey standards. Using a fourth difference error of a continuous measurement swath, contracted geomagnetic surveys must maintain a 0.1 nT noise envelope (±0.05 nT) [42], [50]. Outside of these tolerances, measurement legs would be re-flown. In [13], [27], [51], the GeoSurv II geomagnetic survey UAV attempted to meet the 0.1 nT (±0.05 nT) target for static-field sources and 0.01 nT (±0.005 nT), for transient-field sources. In [17], the Corvus geomagnetic survey UAV, further incorporated improvement ratios (IR ~20) from manned aeromagnetic compensation studies ([44], [49]) to produce a pre-compensation target of 2.0 nT at the magnetometer location. For comparison, the NRC Convair 580 (manned) aeromagnetic research aircraft pre-compensation field has been reported between 5.0 nT [32] and 20 nT [8]. It is understood that aeromagnetic survey and MAD mission profiles are much different, however much of the details behind military capabilities remain cloaked under operational security. Thus, for the purposes of this study, a 2.0 nT pre-compensation total-field target was selected to remain competitive with modern low signature UAVs.

As an amplification, it is of value to briefly mention the MAD frequency bands of interest. In [44], adaptive compensation algorithms were applied to the MAD sensor frequency band (<1.0 Hz) and portion extreme low frequency (ELF) frequency band (1.0 to 10 Hz) to observe the reduction in noise. In the context of MAD, respective bandpass filters are used in conjunction with fixed-term, time-domain compensation [32]. Similarly, for the GeoSurv II geomagnetic survey UAV, it was specified that the transient sources of interest were ranged from of zero to 5.0 Hz [13], [27]. The MAD and ELF bands contain sources from static-field (DC, 0 Hz), structural vibrations to assorted avionics, DC-current switching and certain AC electric-currents [32]. While most electric motors and gas engines rotate at RPMs outside of these bands, optically-pumped magnetometers are known to alias higher frequency signals into MAD or ELF frequency ranges [52]. Thus, care must be applied when selecting bandpass filters.

2.3.2 Vehicle Characterization Strategies

While the magnetic signature characterization and management strategies are well developed for spacecraft [53]–[56], ships [30], [39], [47], [57] and autonomous undersea vehicles (AUVs) [23], [35], [36], [58]–[60], most UAV studies have been limited to the current decade. Both rotary-wing [61], [62] and fixed-wing [51], [62]–[66] UAVs have been evaluated for geomagnetic surveys. The characterization strategies for UAVs either attempt to measure isolated magnetic sources or attempt to characterize the UAV with all sources in situ.

For the flight control servos of the GeoSurv II UAV, Wells [13] proposed single dipole and multipole modelling based on isolated experimental measurements along with passive cancellation schemes. Forrester [27], [34] later improved the experimental procedures, dipole models, optimized the flight control servo configuration and validated the results using COMSOL numerical simulations. Nelson [8] used a magnetometer probe on the Brican TD100 UAV to meticulously identify magnetic sources for demagnetization, replacement or characterization. Sources extracted for characterization were isolated, oriented through ten positional measurements and a least squares approximation was applied to determine the ideal magnetic dipole parameters for each source [8]. Furthermore, Nelson [8] compared the transient-fields from four potential servos.

Sterligov et al [2], [45] experimentally-mapped a GeoScan-201 flying-wing UAV using a using a custom-gridded surface above the UAV. In this study, magnetic sources were identified in situ and transient-fields from servos and electric motors were examined. Tuck et al. [17] used a custom measuring stand that included a GPS receiver, autopilot and magnetometer to measure at various continuous points around the Corvus UAV. A series of filtered heat maps were used to identified in situ magnetic sources, observe transient-field tests and implement a multi-criteria index overlay to provide a map of the UAV planform.

In both in situ cases, the source identification relies heavily on interpolation and is limited to a 2D planform view of the aircraft. The methodology presented by Tuck et al. [17] is scalable to larger UAVs, unlike the methodology presented by Sterligov et al [2], [45]. The primary advantage of these strategies is that operational UAVs can remain ready for flight, unlike the isolated source strategies presented by Forrester [27], [34] and Nelson [8]. While time-consuming, these isolated source methods enable modelling of aircraft components in 3D space. With the VTOL configuration, a 3D model is much more desirable. Furthermore, if aircraft components are ever modified or replaced, they can be reassessed using the magnetometer probe. If characterization is required, only the affects component parameter would be updated in aircraft signature models.

3 Experimental Methodology & Results

The purpose of this chapter is to outline the methodology used to experimentally characterize the components of the UAV. Furthermore, the chapter describes the equipment used, experimental planning considerations, experimental procedures, experimental results, how magnetic parameters were computed and a summary of conclusions.

3.1 Measuring Magnetic Fields

It is necessary to first define the tools used to magnetically characterize aircraft components. The magnetometer is used to characterize both the aircraft and an operational payload.

3.1.1 Magnetometer Types

For the purposes of this paper, all magnetometers are sorted into two categories: scalar and vector magnetometers. Scalar magnetometers, also known as total-field (TF) or total magnetic intensity (TMI) magnetometers, measure only the scalar magnitude (norm) of the magnetic field, independent of orientation. Conversely, (three-axis) vector magnetometers measure the magnitude and direction of the magnetic field. Generally, uniaxial (vector) sensors, arranged in an orthogonal configuration, are used to measure the three components of Earth's geomagnetic field. Table 8 summarizes the similarities and differences between them. The following sections will expand on the contents of Table 8.

Table 8: Summary of Magnetometer Types

	Vector Magnetometers	**Scalar Magnetometers**
Sensor Orientation	Only Measures in Specific Axes	Orientation Independent (less dead zones)
Experimental-Use	Measures Orthogonal Components of Magnetic Fields	Measures Total Magnetic Field Magnitude (Norm)
Operational-Use (Airborne Magnetic Search - MAD)	Measure Changing Magnetic Fields due to Aircraft Maneuvers- Input to Noise Compensation Algorithms	Anomalies in Total Magnetic Field Indicate Detection - Primary Concern in MAD
Relevant Magnetometers [19], [67]	Uniaxial or Three-Axis Fluxgates	Optically-Pumped, Vapour-Pumped, Proton Procession

3.1.2 Experimental Context

In an experimental (ground-based) context, measurements are taken near test objects at various distances to observe the field decay properties. Scalar magnetometers are commonly used [8], [13], [17], [27], [45], [61] to measure localized magnetic fields. Additional scalar magnetometers can be implemented into test procedures to observe magnetic gradients or measure the background/ambient magnetic fields away from the test object [8], [17], [45], [61]. Similarly, vector magnetometers can fill similar roles near and far from test objects [34], providing their relative orientations are known [13], [27]. The most common experimental use for vector magnetometers is to obtain the vector components of Earth's geomagnetic field [27] in lieu of published IGRF geomagnetic models [8], [13].

3.1.3 Operational Context

In an airborne operational context, both types of magnetometers are employed on airborne platforms [34], [44], [46]. In MAD operations, scalar magnetometers are used as they can sense magnetic anomalies independent of aircraft attitude (excluding dead zones). Vector magnetometers are typically rigidly-mounted to sense relative changes in Earth's geomagnetic field as the aircraft maneuvers. Operationally, vector magnetometers provide real-time magnetic vector component measurements. Combined with scalar magnetometers, these measurements are then fed into compensation algorithms [40], [41] to account for the noisy interaction between Earth's magnetic field and ferromagnetic/conductive components of the vehicle. For instance, the MAD-XR sensor payload contains both vector and scalar magnetometers in order to apply compensation algorithms.

3.2 Progression and Overview of Magnetic Experimental Methodology

Figure 32 summarizes the magnetic experimental characterization process used on the subject UAV. The process was split into four steps and covers the following progression: Experimental Preparations (3.3), Hot-Spot Localization (3.4), Whole Vehicle Tests (3.5) and Individual Component Tests (3.6).

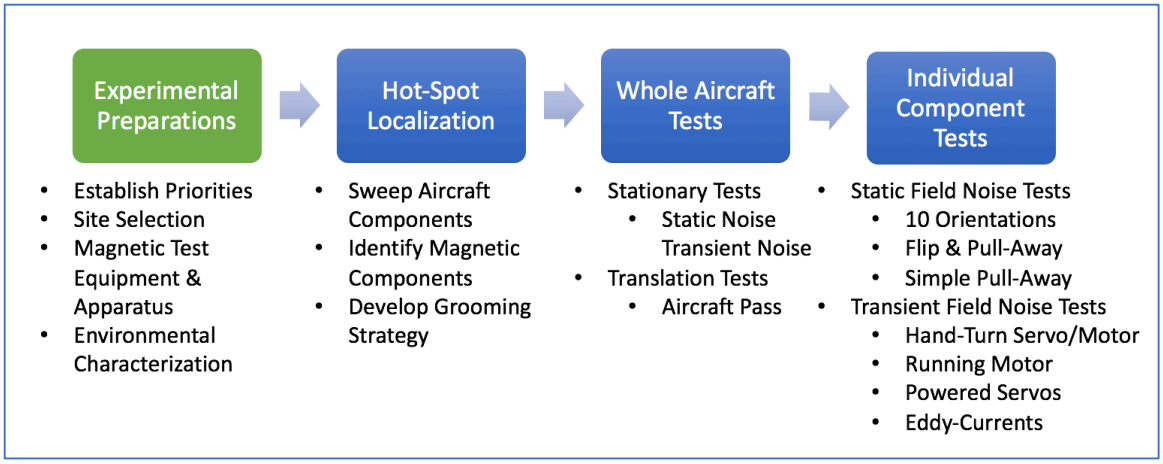

Figure 32: Experimental Characterization Process

3.3 Experimental Preparations

The purpose of this section is to outline the planning and preparation efforts that took place prior to the experimental characterization campaign. Furthermore, the section describes the initial experimental priorities, test site surveys, equipment used, aircraft experimental preparations, and environmental characterization procedures.

3.3.1 Priorities for Experimental Characterization

An important first step was to establish experimental priorities – this involved assessing the vehicle based on suspected magnetic effect of all systems and components. Table 9 outlines the magnetic testing priorities for the Nebula N1 UAV. The purpose of this list was to drive experimental planning decisions, ensure proper allocation of resources, and ensure aircraft components of (suspected) greater magnetic significance were properly characterized.

Table 9: Experimental Priorities for Magnetic Signature Characterization

Experimental Priority	Group	Components	Static Fields	Transient Fields
1	Servos	Flight Controls & Throttle	X	X
2	Primary Propulsion	DC Brushless VTOL Motors	X	
		Combustion Forward Flight Engine	X	X
3	Avionics Bay	Localization of Magnetic Hot-Spots	X	X
4	Alternate Propulsion	DC Brushless Forward Flight Motor	X	X
5	Fasteners	Assorted Fasteners / Hardware	X	

Reviewing the aircraft configuration in Figure 7 (section 1.2.3), one can see the reasoning behind the experimental priorities list. The flight control servos were deemed greatest priority as they would be the closest sources to potential MAD locations. Furthermore, there was significant emphasis placed on flight control servos within the literature review [13], [17], [27], [45]. Next, it was assumed that the DC brushless VTOL motors and the forward flight combustion engine would cause significant magnetic noise, as they both contain large permanent magnets and electromagnetic windings. Per the mission profile (section 1.2.4), the transient field characteristics of the VTOL motor were not prioritized as they would be inactive during (forward flight) magnetic searches. Thirdly prioritized were the assorted and magnetically-unknown avionics located within the fuselage. The forward flight DC brushless motor is purely an alternative propulsion system, to be used in some developmental flights. Lastly, the various ferromagnetic fasteners that are noted in other magnetic grooming studies were the final priority.

3.3.2 Aircraft Preparations

The aircraft was also prepared for magnetic testing. Figure 33 depicts the aircraft geometric coordinate system assigned to the Nebula N1 UAV. The origin was placed at the leading-edge wing root with the x-axis projecting forward towards the nose, y-axis towards the starboard wingtip and z-axis downwards. Prior to magnetic testing, the 3D geometric coordinates of all aircraft components and systems were recorded prior to conducting magnetic tests. This was a key step to enable the 3D magnetic modelling in Chapter 4.

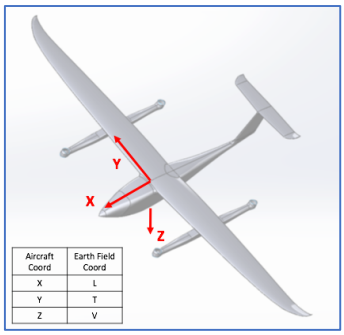

Figure 33: Aircraft Reference System (Modified From [14])

Note there are two coordinate systems used in this report. Table 10 provides a summary of the equivalency among aircraft geometric coordinate system and the coordinate system used for aeromagnetic compensation (section 4.3.1).

Table 10: Coordinate System Equivalency

Aircraft Coordinate System	Earth Coordinate System
X	L
Y	T
Z	V

3.3.3 Site Surveys

The largest challenge with obtaining magnetic experimental results is avoiding background noise. For the purposes of these experiments, the following three locations were considered for magnetic testing of the Nebula N1 UAV in Victoria, Canada: UVic CfAR (3.3.3.1), 676 Royal Canadian Air Cadet Squadron Parade Hall (3.3.3.2) and NRCan Magnetic Observatory – Victoria (3.3.3.3). These locations were evaluated based on their existing infrastructure and suspected magnetic qualities.

To ensure experimental fidelity, it is necessary to secure a test site with the low ambient noise level. It is necessary to avoid areas of high manmade (cultural) noise (section 2.2.3.3). For that reason, rural sites or those on the outskirts of major cities tend to be used. Moreover, the site should also avoid area of high geological variation (section 2.2.3.2.1).

3.3.3.1 UVic CfAR Site Survey

Located at Victoria International Airport, UVic CfAR (Figure 34) was surveyed as a potential site for magnetic testing. Being the computational and physical workspace/workshop for UVic CfAR UAV projects, it is an established location for UAV testing.

Figure 34: Location of UVic CfAR: 48°39'05" N 123°25'04"W

The UVic CfAR workshop (Figure 35) features a variety of tools and large metal workbenches for assembling unmanned vehicles. However, the proximity of these ferromagnetic materials makes the UVic CfAR workshop unsuitable for magnetic testing.

Figure 35: UVic CfAR: Workshop

During magnetic testing, the movement of personnel, ferromagnetic or electrically-conductive material would be restricted. While the conducting experiments in-house is convenient, the significant toll on staff during testing would be too great. Furthermore, CfAR's proximity to active airport taxiways could introduce anomalies into testing data. UVic CfAR was deemed ill-suited for vehicle and component magnetic characterization, and as a result only qualitative magnetometer probe testing was conducted here.

3.3.3.2 Air Cadet Parade Hall Site Survey

The 676 Royal Canadian Air Cadet Squadron Parade Hall was also surveyed for magnetic testing. Constructed of mostly wooden materials and farther from the active runway, the Air Cadet Hall (Figure 36) showed great potential.

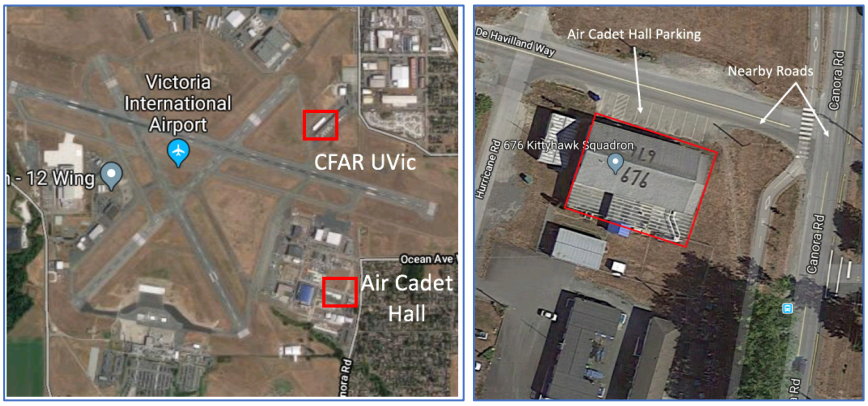

Figure 36: Location of Air Cadet Hall: 48°38'33"N 123°25'02"W

Figure 37 shows the spacious interior of the facility. The building allowed for full-scale aircraft testing within a weather-protected facility. Despite being closer to residential

vehicle traffic, this site was selected as the primary site for magnetic testing given its proximity to CfAR, spaciousness, existing infrastructure, and less ferromagnetic content.

Figure 37: Inside of Air Cadet Parade Hall

3.3.3.3 NRCan Magnetic Observatory – Victoria Site Survey

Part of the International Real-time Magnetic Observatory Network (INTERMAGNET), NRCan Magnetic Observatory – Victoria was also surveyed for magnetic testing. The remote forested site (Figure 38) is a 30-minute drive from UVic CfAR and offered many advantages for magnetic testing.

Figure 38: NRCan Magnetic Observatory: 48°31'13"N 123°24'56"W

Being a magnetic observatory, the geological properties of the site have been previously surveyed for magnetic measurements [68]. Furthermore, the NRCan facilities (Figure 39) are far from environmental, geological, and other cultural noise sources.

Figure 39: NRCan Magnetic Observatory: Canadian Magnetic Observatory System [CANMOS] (left) and surrounding grounds (right)

Among the sites surveyed, the NRCan site had the most favourable magnetic properties. However, the NRCan site infrastructure was least favourable. Being an isolated and wooded area, resources were limited. The service buildings were very small and had limited or no electrical power. The surrounding forest featured moss-covered rocks, uneven terrain and exposure to poor weather. Based on the infrastructure limitations and assumed low ambient noise level, this site was selected as the secondary site for magnetic testing, reserved for sources with the smallest signals (i.e. running engine tests)

3.3.4 Magnetic Test Equipment & Apparatus

This section outlines the magnetic test equipment and apparatus used for the experimental characterization of the subject UAV. The magnetic test equipment (

Table **11**) was supplied by National Research Council (NRC) Flight Research Lab (FRL) and CAE Inc. The scalar magnetometers were used as background and test object sensors while the vector magnetometers were used only to obtain Earth's magnetic vector components.

Table 11: Magnetic Test Equipment Used for Experiments

Device	Type	Purpose	Notes
Geometrics G824A Magnetometer	Scalar	Primary: Experimental and Background Magnetometers	Master-and-Slave Configuration for Post-Processing Background Removal
QuSpin QTFM Magnetometer	Scalar	Secondary: Experimental and Background Magnetometers	
Billingsley TFM100G2 Magnetometer	Vector	Primary: Obtain Local Measurements of Earth's Field Components	N/A
Bartington MAG-03 Magnetometer	Vector	Secondary: Obtain Local Measurements of Earth's Field Vector Components	
Foerster MAGNETOSCOP 1.069 Probe	Scalar	Magnetic "Hot Spot" Localization	Point Pole Probe

Unless otherwise stated, Figure 40 shows the experimental set-up and sensor geometry for all magnetic tests. In this set-up, the test component was placed on a non-magnetic table at a known distance from the primary magnetometer (TF #1). Using a master-and-slave configuration, a secondary magnetometer (TF #2) was used to capture background noise far from the test component, see Table 12. Therefore, the magnetic field of the test object $B_{test\ object}$ can be obtained with the following expression.

$$B_{test\ object} = B_{TF\#1} - B_{TF\#2}$$

Table 12: Purpose of TF Scalar Magnetometers

Magnetometer	Magnetic Purpose	Proximity to Test Object
TF#1	Test Object	Close to Test Object
TF#2	Background Noise	Far from Test Object

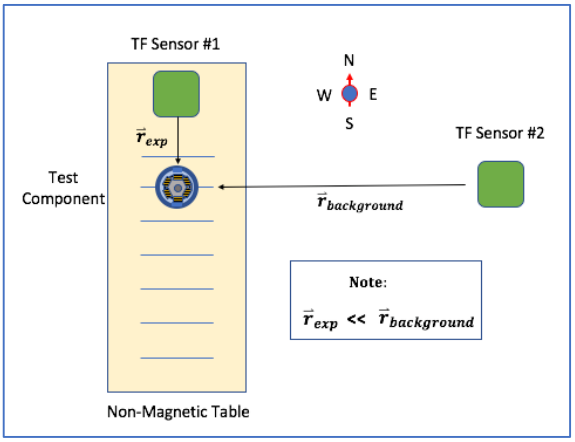

Figure 40: Component Testing Geometry and Set-Up

The following procedure summarizes the apparatus set-up:

1. Prepare aircraft and components to be characterized.
    a. Establish aircraft coordinate system.
    b. Prior to disassembly, obtain position and orientation for all aircraft components using aircraft coordinate system.
    c. Establish coordinate system for each component.
    d. Remove components (as practicable).
2. Magnetically-sanitize test personnel and test site.
3. Characterize background and test site.
    a. Obtain components of Earth's geomagnetic field $\left(\vec{B}_{E\,x}, \vec{B}_{E\,y}, \vec{B}_{E\,z}\right)$ using vector magnetometer (or published IGRF values), see section 3.3.5.
4. Establish TF #1 on non-magnetic table.
5. Establish TF #2 to measure ambient field away from table in master-and-slave configuration.
6. Level all TF sensors to test component.
7. With a compass, align all TF sensors with magnetic north.

Demagnetizing equipment was also used during the experimental characterization campaign. Certain components, if determined suitable, were degaussed using equipment provided by NRC. There were two custom devices used: a pulsating "puck" (Variac) and wire coil "solenoid" degausser. Using 60 Hz AC input, demagnetizers generate a coercive magnetic field to reduce the permanent magnetization of ferromagnetic components.

3.3.5 Environmental Characterization

To characterize the unwanted ambient magnetic field, it is necessary to conduct a background characterization. The purpose is to establish an ambient noise floor and understand the effect of natural or man-made magnetic noise sources near the test site. In the absence of a site-specific background characterization, published field data from IGRF models may be used, however it may not adequately capture localized field phenomena. As in all magnetic tests, the movement of personnel, ferromagnetic, or electrically-conductive material was restricted while measuring magnetic fields.

3.3.5.1 Background Field Characterization – Air Cadet Hall

At the Air Cadet Hall, a background magnetic characterization was completed. This was conducted prior to moving any equipment into the space. Two Geometrics G824A magnetometers (in master-and-slave configuration) were utilized, taking continuous measurements for 2 minutes at a 250 Hz sampling frequency, see Figure 41.

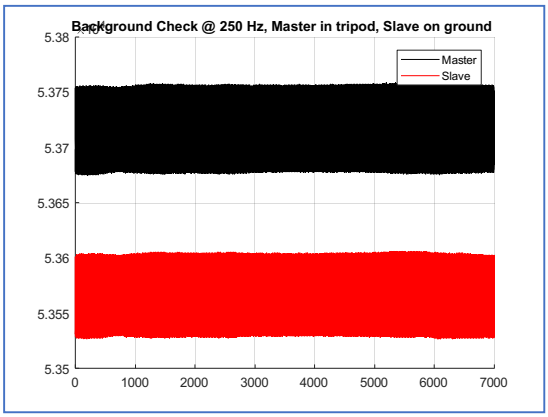

Figure 41: Background Magnetic Noise (time domain) @ 250 Hz: Air Cadet Hall [52]

Furthermore, these measurements were observed in the frequency domain (see Figure 42). Note the large signal spikes near 1 Hz and 60 Hz. The former was due to nearby vehicle and residential traffic (cultural noise) and the latter was due to AC electrical power system within the facility.

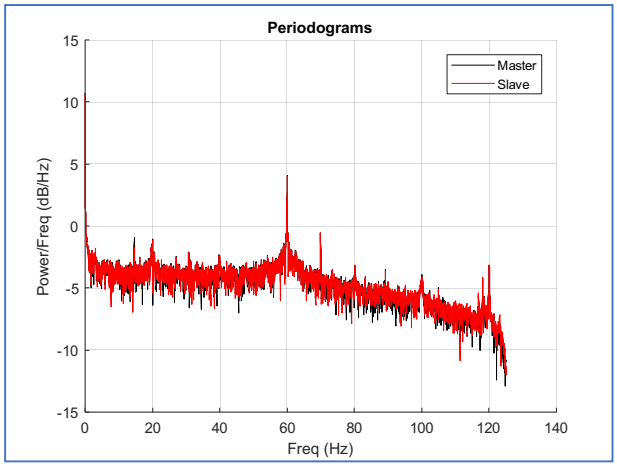

Figure 42: Background Magnetic Noise (frequency domain) @ 250 Hz: Air Cadet Hall [52]

3.3.5.2 Vector Components of Earth's Geomagnetic Field – Air Cadet Hall

Using the Billingsley TFM100G2 magnetometer, the vectors of Earth's geomagnetic field were obtained. Comparable to published IGRF-12 data (for Jan 8, 2018), the measured values are presented in Table 13.

Table 13: Measured Vector Components of Earth's Geomagnetic Field: Air Cadet Hall

Vector Component	Cardinal Direction	Measured Values [nT]	IGRF Values [nT] [69]
$\boldsymbol{B_{E\,X}}$	North	19 372	17 988
$\boldsymbol{B_{E\,Y}}$	East	37	5 209
$\boldsymbol{B_{E\,Z}}$	Down	50 081	50 484
$\|\boldsymbol{B_E}\|$	N/A	53 697	53 846

$\|B_E\|$ was obtained by taking the norm of the vector magnetometer measurements, $\|B_E\| =$ 53 697 nT. Note the geomagnetic coordinate system: x-axis is positive in the northward direction, y-axis is positive in the eastward direction and z-axis is positive in the downward direction. While the IGRF values closely match the measured values, it was assumed that there were some local magnetic phenomenon causing the field differences in $B_{E\,Y}$. All experimental calculations in this report use the measured values.

3.3.5.3 Horizontal Gradient – Air Cadet Hall

To obtain the horizontal gradient (in north and east direction), two Geometrics G824A magnetometers were utilized in following procedure.

Background Gradient Characterization:

1. Using continuous measurements move TF #1 to position #1 & wait for 15 sec.
2. Move TF #1 to position #2.
3. Wait for 15 sec.
4. Move TF #1 back to position #1 (momentarily, to induce a measurement disturbance).
5. Move TF #1 to position #3.
6. Wait for 15 sec.
7. Repeat steps #5 through #7 from remaining positions.
8. Field measurements are obtained by subtracting TF #1 from TF #2.

9. Subtract east-west measurements and divide by 24.5 cm to obtain G_{EAST} horizontal magnetic gradient [nT/m].
10. Subtract north-south measurements and divide by 24.5 cm to obtain G_{NORTH} horizontal magnetic gradient [nT/m].
11. Average the G_{EAST} and G_{NORTH} results.

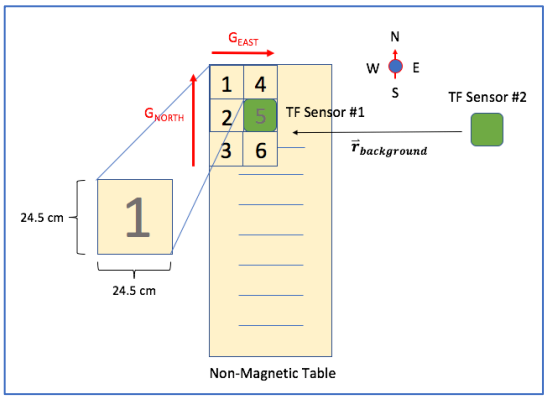

Figure 43: Horizontal Gradient (G_{EAST}, G_{NORTH}) Measurement

Figure 44 shows the measured results plotted as continuous data points. Capturing steps #2 though #8 in the above procedure, the plot shows distinct plateaus (annotated in red) for each positon in Figure 43.

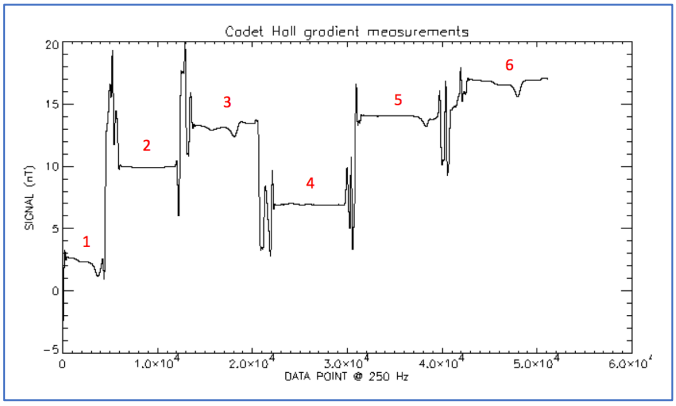

Figure 44: Plot of Horizontal Gradient Measurement Data (Modified from [52])

Furthermore,

Table **14** presents this data in tabular form and Table 15 and Table 16 present the results of the gradient calculation (steps #10 through #12) for both the Air Cadet Hall and NRCan Geomagnetic Observatory

Table 14: Horizontal Gradient Measurement Data for Air Cadet Hall

Position	Measured TF [nT]
1	2.25
2	9.89
3	13.21
4	6.96
5	14.06
6	16.76

While the gradient seemed high, every effort was made to mitigate the horizontal gradient by keeping all measurements contained within the dimensions of the non-magnetic table at the test site.

Table 15: Horizontal Gradient Measurement Results for Air Cadet Hall

Average	Gradient [nT/m]
G_{EAST}	17.25
G_{NORTH}	-20.76

Table 16: Horizontal & Vertical Gradient Measurement Results for NRCan Observatory [70]

Average	Gradient [nT/m]
G_{EAST}	-23.3
G_{NORTH}	7.2
G_{DOWN}	27.2

3.4 Magnetic "Hot-Spot" Localization

Prior to embarking on a vehicle characterization campaign, it is necessary to localize sources of magnetic noise around the vehicle. This allows hidden magnetic sources to be identified and an effective magnetic noise reduction strategy to be developed. The commonly used [8], [17], [27] magnetometer probe for "hot spot" localization is Foerster Magnetoscop (uniaxial) fluxgate sensor (with handheld point pole probe, Figure 45).

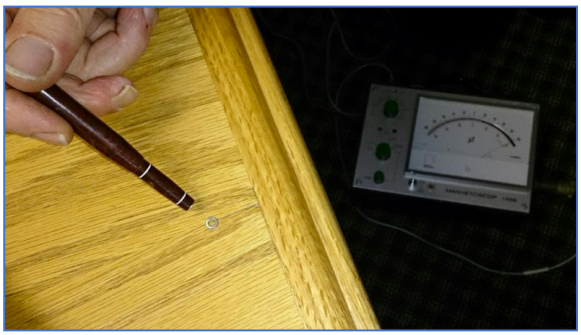

Figure 45: Foerster Magnetoscop Point Pole Probe [8]

Alternatively, without a magnetometry probe, it was suggested in [23], [27] that sweeping small permanent magnets around the vehicle could be used to identify magnetic sources. This is not recommended. When magnetic components are exposed to strong permanent magnets, they can become magnetically saturated (section 2.1.2.3). As it was experienced by the author, many aircraft fasteners became magnetically saturated prior to characterization. Thus, to remain productive, it is recommended that only magnetometer probes be used to identify magnetic sources.

The experimental process, similar to [8], was as follows:

1. Methodically comb the vehicle with the probe to identity magnetic sources around the vehicle, as seen in Figure 46.
    a. Photograph and record observations and results.
    b. Label component hot-spots.
2. For each "hot spot," select a magnetic grooming strategy:
    a. Identify components for immediate degaussing.
    b. Identify components for non-magnetic alternative/replacement.
    c. Otherwise, identify components for experimental characterization.

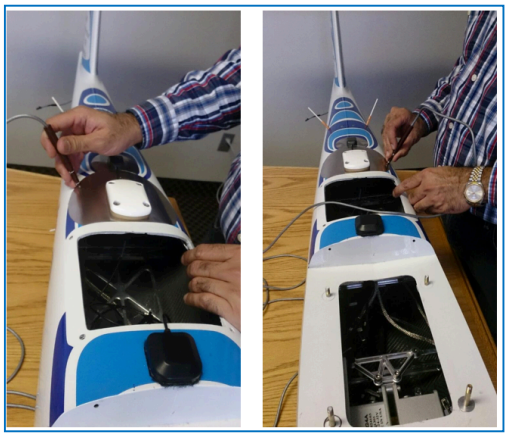

Figure 46: Use of Magnetometer Probe on Brican TD-100 UAV [8]

When using the probe to identify magnetic sources, it was also noted that source orientation was important. In some cases, the orientation of the test object or the angle at which the source was measured would affect the probe measurement value. Test objects containing induced magnetization displayed a constant field value for all orientations whereas test objects containing permanent magnetization displayed different probe values with various

orientation. Sources of induced magnetization contain material that aligns with Earth's coercive geomagnetic field at all orientations. In the case of permanent sources, test object magnetic fields interact with Earth's geomagnetic field as they are re-oriented. This is an important point as it affects the grooming strategy for a test object. Permanent magnetization can be demagnetized (degaussed), whereas induced magnetization cannot.

3.4.1 Degaussing of Magnetic Fasteners and Hardware

From the 'hot-spot" localization, many magnetic sources were degaussed, most notably assorted hardware and fasteners. Certain sources of permanent magnetization were fully degaussed, though some could only be partially degaussed. For demonstration, Table 17 shows a subset of probe results prior to and after degaussing.

Table 17: Sample of Fastener Probe Results Before and After Degaussing

Item Number	Aircraft Fastener Name	Aircraft In Situ Orientation	Before Degaussing [µT]	After Degaussing [µT]
#1	Aft Bulkhead-Saddle, Attachment Bolt	± X	120	±1
#1	Aft Bulkhead-Saddle, Bolt Spring	± X	100	±1
#2	Belly-Payload Access Cover, Attachment Bolt	± Z	186	±1
#2	Belly-Payload Access Cover, Bolt Spring	± Z	40	±1
#4	Fwd Avionics Bay Access Cover, Attachment Bolt	± X	-34	-13 (induced)
#8	Launch Guide Rail (Port/Starboard)	± Y	-45	-26 (induced)
#9	DGPS Antenna Attachment Bolts	± Z	-200	-27 (induced)

From Table 17, one can see that experimentally-assigned Item Numbers #1 and #2 showed a significant decrease in field magnitude once degaussed. This indicates that there was a strong presence of permanent magnetization within these sources. Moreover, experimentally-assigned Item Numbers #4, #8 and #9 shows less significant results indicating residual induced magnetization which cannot be removed. To the greatest extent possible, assorted fasteners (bolts, screws, washers, springs), electrical connectors, and launch hardware were degaussed to reduce permanent magnetic noise on the Nebula N1

UAV. Once demagnetized, many of these sources were also retested using small source pull-away tests discussed in section 3.6.1.2.

3.5 Whole Vehicle Noise Tests

Despite being preferable to characterize vehicle components individually, there are some instances where whole vehicle tests were utilized. This section outlines the static and transient field tests completed on large sections of the vehicle. Many of the experiments described here could be conducted for power-on and power-off vehicle states. In this study, whole vehicle tests were used only as crude order-of-magnitude measurements.

3.5.1 Stationary Noise Tests

A series of tests were completed with the vehicle in a stationary position on the testing surface. These tests eliminated the chance of contaminating the data with movement-induced eddy-currents.

3.5.1.1 Transient Field Noise Tests

When testing the transient noise of a vehicle there are various ways data can be obtained. The purpose of this section is to explain testing procedures used.

3.5.2 Translating Vehicle Noise Tests

The purpose of this section is to outline the noise tests that involved translating the vehicle either past or away from the primary magnetometer. The Unpowered Pull-Away Test (3.5.2.1) and the Unpowered Profile Test (3.5.2.2) were selected as appropriate testing methods.

3.5.2.1 Unpowered Pull-Away Noise Test

At the time of testing, the forward flight brushless DC motor could not be removed nor could it be characterized individually. Thus, a partial vehicle pull-away test was conducted on the aircraft fuselage (without VTOL motors and wings). To the greatest extent possible, certain avionics were removed from the aircraft to isolate the motor as much as possible.

Figure 47 shows the fuselage facing north on the testing surface near TF #1 with TF #2 in the background.

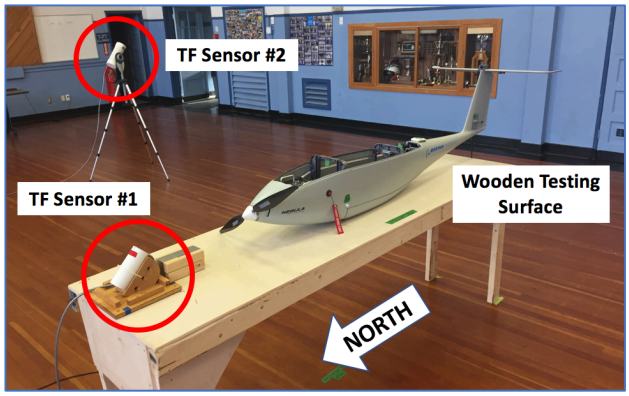

Figure 47: Fuselage Unpowered Static Field Pull-Away Test: Set-Up

Two southward pull-away tests were completed: one with the fuselage oriented north and the other oriented south.

Unpowered Pull-Away Test:

1. Measure distances from significant magnetic sources.
2. With all test personnel still in place, begin continuous measurements for a 15 sec baseline.
3. While keeping the vehicle level, translate it away from the TF #1 using personnel hand-off, like Figure 48.
4. At a large distance from TF #1, stop vehicle movement and wait for another 15 sec baseline.

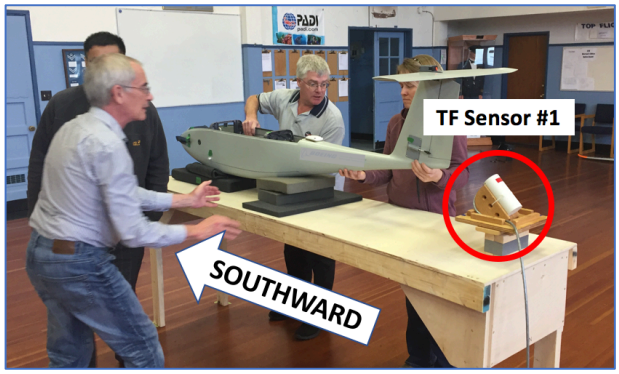

Figure 48: Fuselage Unpowered Static Field Pull-Away Test: Translation Southward

For demonstration, Figure 49 shows the field results of the north-facing pull-away test. The results show a 25 nT disturbance as the fuselage was pulled-away. In this specific case, it was assumed that the magnetic noise signal was mainly due to the forward flight DC brushless motor.

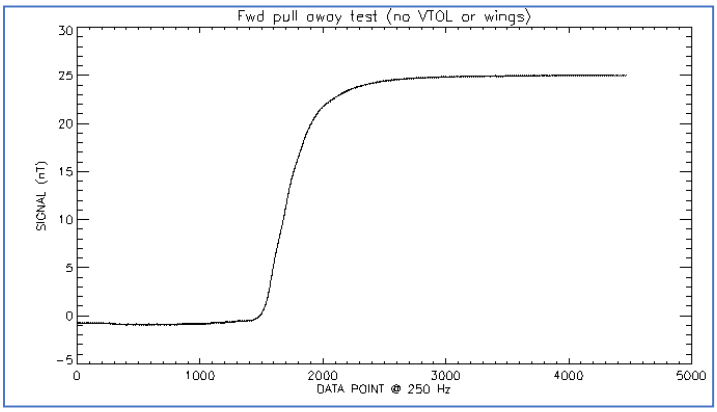

Figure 49: Fuselage Unpowered Static Field Pull-Away Test: North-Facing Results [52]

In the field, it is common to obtain rough or crude approximations based on measured results. Using a simple rule-of-thumb based on the inverse cube field decay property of magnetic fields, the field can be extrapolated to any distance (see below).

$$B_{crude,MAD} = B_{max} * \left(\frac{\|r_{exp}\|}{\|r_{MAD}\|}\right)^3$$

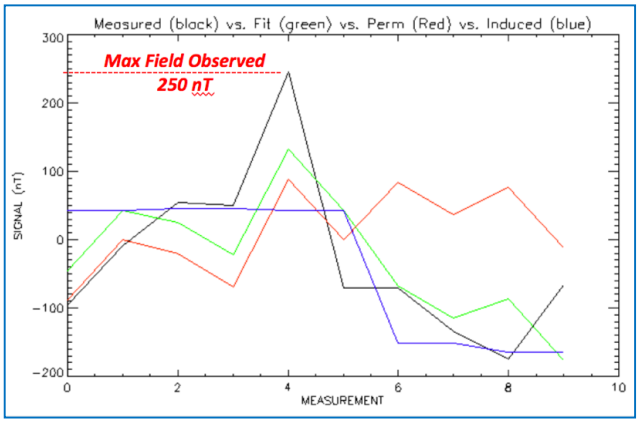

Figure 50: Example Plot of Measured and Computed Magnetic Parameters: Maximum Annotated (Modified from [8])

In other words, the field at any distance (or potential MAD sensor location - $B_{crude,MAD}$) can be approximated using the maximum measured field value B_{max} and their respective distances, r_{exp} and r_{MAD}. Table 18 summarizes the results of the unpowered fuselage pull-away tests. These results were used as order-of-magnitude approximations (~1 nT) to

provide a means to potentially gain confidence in magnetic modelling results. Of note, the crude field extrapolation does not consider direction, but rather, only magnitude.

Table 18: Fuselage Unpowered Static Field Pull-Away Test: Overall Results

Pull-Away Test	Distance to Source [m]			Magnetic Disturbance [nT]	Crude Field Extrapolation [nT]	
	DC Brushless Motor	Fwd Avionics Bay	Aft Avionics Bay		Wingtip @ 2.08 m	Tail @ 1.82 m
North-Facing	0.54	0.75	1.75	25.5	0.45	0.66
South-Facing	2.21	2.00	1.00	0.9	0.96	1.42

3.5.2.2 Unpowered Profile Translation Test

In these tests, the magnetic field disturbance was measured while the fuselage was translated past TF #1. The motivation for this test was to create a test that simulated the magnetic noise caused by the in situ electric motor at the wingtips (a potential MAD location).

Unpowered Profile Translation Test:

1. Use tape to make a pre-measured straight line path past TF #1, like Figure 42.
2. With all test personnel still in place, begin continuous measurements for a 15 sec baseline.
3. While keeping the vehicle level, translate it across TF #1 using personnel hand-off, like Figure 52.
4. Pause for another 15 sec baseline.
5. Change in magnetic noise is obtained by subtracting TF #1 from TF #2.

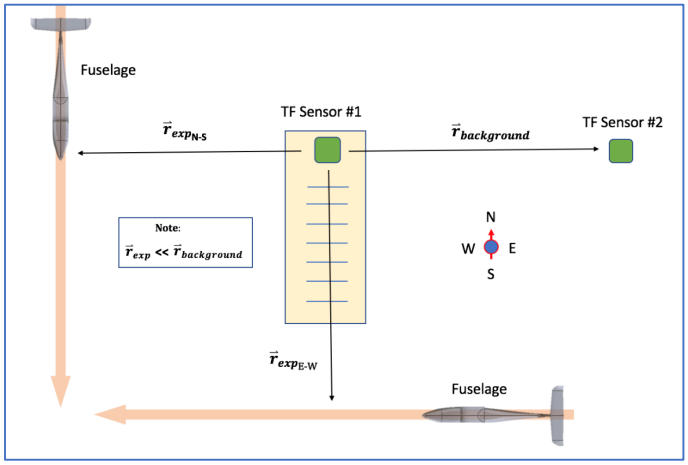

Figure 51: Unpowered Fuselage Translation Tests: Geometry and Set-Up

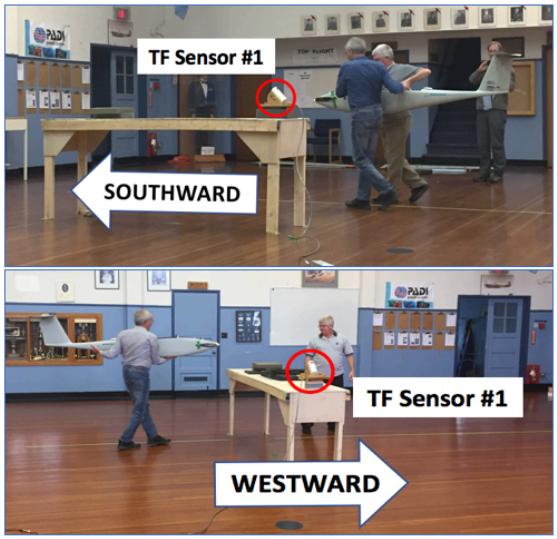

Figure 52: Unpowered Profile Tests: North-South (top) and East-West (bottom)

As an example, Figure 53 shows the field results of the east-west translation test. Peak-to-peak, sources with the fuselage caused a 0.8 nT disturbance as they were translated past the sensor. Using a timer, the large disturbance was correlated to the moment that the DC brushless motor was abeam to the sensor.

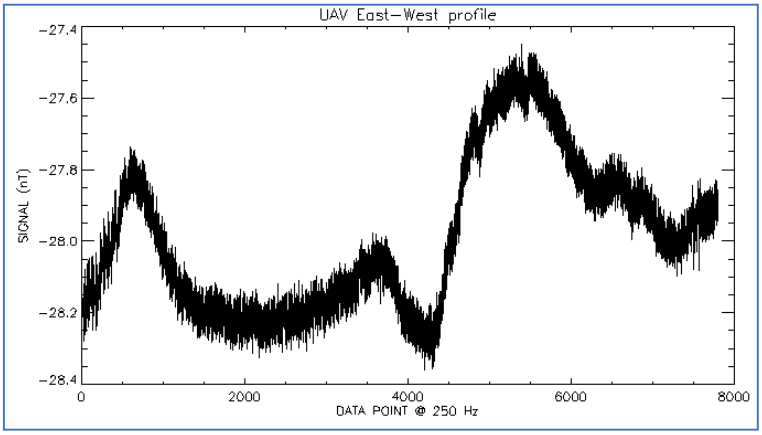

Figure 53: Unpowered Fuselage Translation Tests: East-West Results [52]

Table 19 summarizes the results of the unpowered fuselage pull-away tests. These results were used as order-of-magnitude wingtip approximations (< 1 nT) to provide a means to gain confidence in magnetic modelling results.

Table 19: Unpowered Fuselage Translation Tests: Overall Results

Translate Test	**Distance to Path [m]**	**Magnetic Disturbance [nT]**	**Crude Field Extrapolation Wingtip @ 2.08 m [nT]**
North-South	2.06	0.9	0.87
East-West	1.86	0.8	0.57

3.6 Individual Component Noise Tests

It is preferred to characterize vehicle components individually. Isolating the test object minimizes the chance of unwanted fields from skewing the measurements. This section captures static and transient field tests executed on individual aircraft components. Many of the experiments described here can be conducted for either powered-on and powered-off states.

3.6.1 Static Field Noise Tests

Static field tests refer to tests that include magnetostatic fields that do not change with time. This section outlines the tests performed and corresponding results.

3.6.1.1 10-Orientation 3D Source Characterization

Similar to [8], a 10-orientation 3D characterization methodology was used to obtain magnetic dipole moment components for various aircraft sources. Recalling the total magnetic dipole equation from section 2.1.4, it is re-written below with revised units, B_E [nT] and M [nTm^3].

$$\vec{M}_{total} = \left(\vec{M}_{P\,x} + \mathcal{X}_x * \vec{B}_{E\,x}\right)\hat{\imath} + \left(\vec{M}_{P\,y} + \mathcal{X}_y * \vec{B}_{E\,y}\right)\hat{\jmath} + \left(\vec{M}_{P\,z} + \mathcal{X}_z * \vec{B}_{E\,z}\right)\hat{k}\ .$$

10-Orientation 3D Source Characterization:

1. Set test component at a known distance, directly south from TF #1 (Figure 40).
2. Conduct field tests on test components in ten orientations, as seen in Table 20.
3. Use least squares inversion is used to obtain six magnetic dipole parameters for each test object using the matrix relation below that were derived from dipole equations above.

$$\begin{Bmatrix} B_1 \\ B_2 \\ B_3 \\ B_4 \\ B_5 \\ B_6 \\ B_7 \\ B_8 \\ B_9 \\ B_{10} \end{Bmatrix} = \left(\frac{1}{\|R\|^3 \|B_E\|}\right) \begin{bmatrix} 0 & -2B_{Ex} & -B_{Ez} & 0 & 2B_{Ex}^2 & -B_{Ez}^2 \\ 0 & 2B_{Ex} & -B_{Ez} & 0 & 2B_{Ex}^2 & -B_{Ez}^2 \\ 2B_{Ex} & 0 & -B_{Ez} & 2B_{Ex}^2 & 0 & -B_{Ez}^2 \\ -2B_{Ex} & 0 & -B_{Ez} & 2B_{Ex}^2 & 0 & -B_{Ez}^2 \\ 2B_{Ex} & 0 & B_{Ez} & 2B_{Ex}^2 & 0 & -B_{Ez}^2 \\ -2B_{Ex} & 0 & B_{Ez} & 2B_{Ex}^2 & 0 & -B_{Ez}^2 \\ -B_{Ez} & 2B_{Ex} & 0 & -2B_{Ez}^2 & 2B_{Ex}^2 & 0 \\ -B_{Ez} & -2B_{Ex} & 0 & -2B_{Ez}^2 & 2B_{Ex}^2 & 0 \\ 2B_{Ex} & -B_{Ez} & 0 & 2B_{Ex}^2 & 2B_{Ez}^2 & 0 \\ -2B_{Ex} & -B_{Ez} & 0 & 2B_{Ex}^2 & 2B_{Ez}^2 & 0 \end{bmatrix} \begin{Bmatrix} M_{Px} \\ M_{Py} \\ M_{Pz} \\ \mathcal{X}_x \\ \mathcal{X}_y \\ \mathcal{X}_z \end{Bmatrix}$$

$B_1, \ldots, B_{10}$ terms are the ten orientation magnetic field measurements, $B_{E\,x}$ and $B_{E\,z}$ are the north and down components of Earth's geometric field, respectively. The three permanent dipole moments $M_{P\,x}, M_{P\,y}, M_{P\,z}$ and three directional volume susceptibilities $\mathcal{X}_x, \mathcal{X}_y, \mathcal{X}_z$ are obtained using least squares inversion. Using the six dipole parameters obtained from each test component, the respective magnetic field contributions can be obtained using the models described in Chapter 4.

Table 20: Ten Orientations to Obtain Ten Magnetic Measurements [8]

	Component Coord System		
Orientation	**x-axis**	**y-axis**	**z-axis**
1	East	South	Down
2	West	North	Down
3	North	East	Down
4	South	West	Down
5	North	West	Up
6	South	East	Up
7	Down	North	East
8	Down	South	West
9	North	Down	West
10	South	Down	East

This experimental methodology was used to characterize most of the individual components. Appendix A contains a summary of all magnetic dipole moment results. The following three sections outline the aircraft components characterized using this method (or slight modifications thereof), and provides examples and summaries of the results.

3.6.1.1.1 Avionics / Electronics Testing

As an example of this process, observe the results from the (custom) Flight Battery Pack #1 (Figure 54: Flight Battery Pack #1). Figure 55 shows the (continuous) uncorrected magnetometer data from the ten orientations. Annotated in red are the ten orientations along with background measurements at the beginning and end.

Figure 54: Flight Battery Pack #1

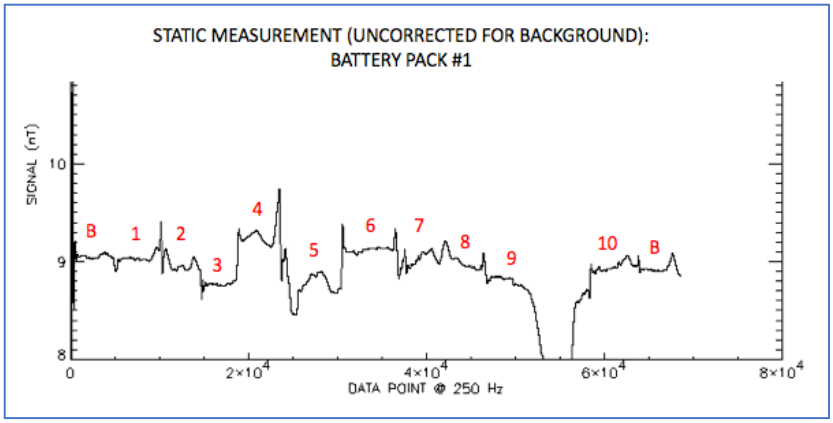

Figure 55: Static Measurement (Uncorrected for Background): Flight Battery Pack #1 (Modified from [52])

Next, Table 21 summarizes the measurement data from Flight Battery Pack #1. These values, along with the measured vector components of Earth's geomagnetic field (section 3.3.5.2), were used in the least squares inversion to produce the magnetic parameters in Table 22.

Table 21: Extracted Static Field Measurement Values: Flight Battery Pack #1

Parameter	**Field Measurement [nT]**	
	Uncorrected	**Average Background Removed**
Background: Start	9.06	N/A
Orientation 1	9.02	3.70E-02
Orientation 2	8.94	-4.94E-02
Orientation 3	8.77	-2.22E-01
Orientation 4	9.25	2.59E-01
Orientation 5	8.88	-1.11E-01
Orientation 6	9.15	1.60E-01
Orientation 7	9.07	8.64E-02
Orientation 8	8.99	0.00
Orientation 9	8.81	-1.73E-01
Orientation 10	8.96	-2.47E-02
Background: End	8.91	N/A
Background: Average	8.99	

Table 22: Results of Least Squares Inversion: All Avionics / Electronics

Aircraft Component	M_{Px} [nTm^3]	M_{Py} [nTm^3]	M_{Pz} [nTm^3]	χ_x [m^3]	χ_y [m^3]	χ_z [m^3]
Battery Flight Pack #1	-2.61E-02	1.00E-04	8.00E-04	5.00E-07	4.00E-07	1.00E-07
Battery Flight Pack #2	-1.47E-01	5.13E-02	-1.27E-01	5.30E-06	1.80E-06	3.00E-07
Video Encoder (Antrica Ant-1772)	1.92E-02	2.47E-02	7.50E-03	9.00E-07	1.60E-06	8.00E-07
DGPS Antenna (NovAtel)	-1.73E-02	-1.40E-03	6.20E-03	6.00E-07	1.20E-06	1.00E-07
DGPS Electronics (NovAtel)	5.09E-02	6.00E-02	7.66E-02	2.69E-06	2.43E-06	1.19E-06
Silvis 2.4 GHz Radio - Reduced Cabling (StreamCaster 4200)	-8.21E-02	-1.30E-01	-1.90E-01	0.00E+00	2.00E-07	9.00E-07

As conducted before, a quick field extrapolation was conducted to observe the magnetic noise that would be experienced at potential MAD locations, seen in section 3.5.2.1. In the case of the Flight Battery Pack #1, magnetic noise would be very low (Tail ~0.01 nT; Wingtip ~0.004 nT). Moreover, probe tests suggest that the fasteners on the battery packs could be degaussed, further reducing their magnetic contribution. It was also suggested that magnetized hardware could be the reason why Flight Battery Pack #2 had larger extrapolated noise value compared to Flight Battery Pack #1.

Table 23: Crude Field Extrapolation: Summary of Electronics Tested

	Experimental Measurements		Crude Field Extrapolation			
			Wingtip		Tail	
Aircraft Component	**Distance [m]**	**Maximum Magnetic Field [nT]**	**Distance from Source [m]**	**Maximum Field [nT]**	**Distance from Source [m]**	**Maximum Field [nT]**
Battery Flight Pack #1	0.5	0.250	1.98	0.004	1.42	0.011
Battery Flight Pack #2	0.5	2.800	2.03	0.042	0.57	1.865
Video Encoder (Antrica Ant-1772)	0.5	0.850	2.01	0.013	1.57	0.027
DGPS Antenna (NovAtel)	0.5	0.500	2.01	0.008	0.64	0.234
DGPS Electronics (NovAtel)	0.5	1.300	2.01	0.020	0.64	0.609
Silvis 2.4 GHz Radio - Reduced Cabling (StreamCaster 4200)	0.5	2.100	2.03	0.031	1.66	0.057

3.6.1.1.2 Throttle and Flight Control Servos Testing

Highest on the experimental priorities list, this test shows the Currawong CBS-15 servo used all throughout the Nebula N1 UAV. The servo is used for flight controls, as well as to throttle the gas combustion engine. A single servo was tested using the ten-orientation methodology.

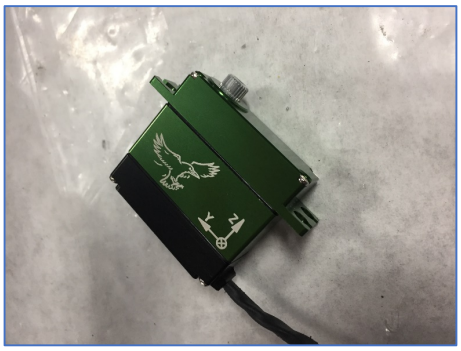

Figure 56: Currawong CBS-15 Servo

Table 24 shows the test results and crude field extrapolation of the single servo test for each location throughout the aircraft. Noting the very large field extrapolated at the tail

(~700 nT), one can immediately see that the elevator and rudder servos have a significant effect in this payload location.

Table 24: Extrapolation of Field for Each Servo Location

	Experimental Measurements		Crude Field Extrapolation			
			Wingtip		Tail	
Aircraft Component	**Distance [m]**	**Maximum Magnetic Field [nT]**	**Distance from Source [m]**	**Maximum Field [nT]**	**Distance from Source [m]**	**Maximum Field [nT]**
Gas Engine Throttle Servo	0.25	10.750	2.00	0.021	1.54	0.046
Port Flap Flight Control Servo	0.25	10.750	1.38	0.063	1.25	0.085
Port Aileron Flight Control Servo	0.25	10.750	0.61	0.730	1.75	0.031
Starboard Flap Flight Control Servo	0.25	10.750	2.52	0.011	1.25	0.085
Starboard Aileron Flight Control Servo	0.25	10.750	3.29	0.005	1.75	0.031
Port Elevator Flight Control Servo	0.25	10.750	2.25	0.015	0.38	2.985
Starboard Elevator Flight Control Servo	0.25	10.750	2.36	0.013	0.38	2.985
Rudder Flight Control Servo	0.25	10.750	2.23	0.015	0.06	678.146

Table **25** shows the six magnetic parameters of the single servo test. Note for each servo, a transformation was applied to match the orientation as it sits within the aircraft. This an important step as mis-orientation of magnetic dipoles would change the magnetic modelling results.

Table 25: Magnetic Parameter Results: Servo, Transformed into Local Orientations

Aircraft Component	$M_{P\,x}$ [nTm^3]	$M_{P\,y}$ [nTm^3]	$M_{P\,z}$ [nTm^3]	χ_x [m^3]	χ_y [m^3]	χ_z [m^3]
Gas Engine Throttle Servo	1.24E-02	1.52E-02	1.26E-01	4.57E-07	3.32E-07	1.12E-06
Port Flap Flight Control Servo	1.26E-01	1.52E-02	-1.24E-02	1.12E-06	3.32E-07	4.57E-07
Port Aileron Flight Control Servo	1.26E-01	1.52E-02	-1.24E-02	1.12E-06	3.32E-07	4.57E-07
Starboard Flap Flight Control Servo	-1.26E-01	1.52E-02	1.24E-02	1.12E-06	3.32E-07	4.57E-07
Starboard Aileron Flight Control Servo	-1.26E-01	1.52E-02	1.24E-02	1.12E-06	3.32E-07	4.57E-07
Port Elevator Flight Control Servo	1.26E-01	1.52E-02	-1.24E-02	1.12E-06	3.32E-07	4.57E-07
Starboard Elevator Flight Control Servo	-1.26E-01	1.52E-02	1.24E-02	1.12E-06	3.32E-07	4.57E-07
Rudder Flight Control Servo	-1.24E-02	-1.52E-02	1.26E-01	4.57E-07	3.32E-07	1.12E-06

To ensure the servo results were reasonable, Table 55 in Appendix D compares the servo results with servo data from a magnetic grooming study on the Brican TD100 UAV [8]. By chance, the existing Currawong CBS-15 servos on the Nebula N1 had a relatively low (permanent and induced) magnetic signature compared to the data found in the literature.

3.6.1.1.3 Propulsion Unit Testing

In the case of the propulsion units (Figure 57) a modified procedure was used. Given the presence of radially-symmetrical internal windings and permanent magnets, the procedure was executed using four rotor (propeller spindle) positions: 0 deg, 90 deg, 180 deg and 270 deg. The results of each test were then averaged to obtain average magnetic parameter values. See the results for each propulsion unit in Table 26, Table 27 and Table 28. Only one VTOL motor was tested and it was assumed that all VTOL motors would have the same magnetic properties.

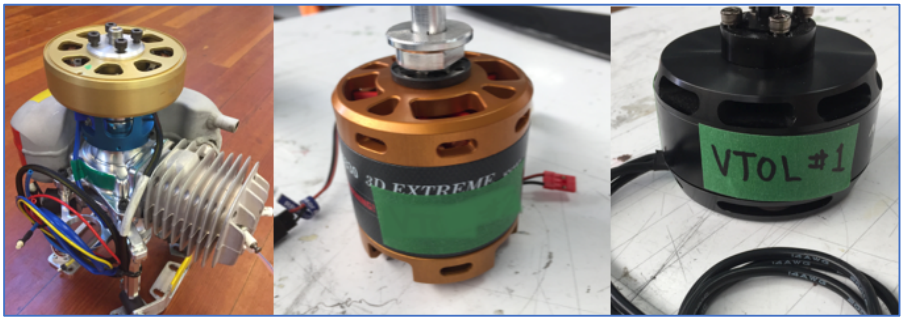

Figure 57: Propulsion Units: Forward Flight Gas Engine, Forward Flight Electric Motor, VTOL Electric Motor

Table 26: Magnetic Parameters: Gas Combustion Engine

Parameter	0 deg	90 deg	180 deg	270 deg	Average
M_{Px} [nTm^3]	-0.32	-4.02	-4.59	-0.14	-2.27
M_{Py} [nTm^3]	-4.71	2.03	2.98	-7.36	-1.77
M_{Pz} [nTm^3]	6.14	9.94	-10.48	-33.19	-6.90
χ_x [m^3]	7.00E-06	1.60E-04	2.03E-04	5.90E-05	1.07E-04
χ_y [m^3]	-8.20E-05	1.90E-04	2.22E-04	-5.00E-06	8.10E-05
χ_z [m^3]	7.40E-05	1.36E-04	1.02E-04	1.24E-04	1.09E-04

Table 27: Magnetic Parameters: VTOL DC Brushless Motor

Parameter	0 deg	90 deg	180 deg	270 deg	Average
M_{Px} [nTm^3]	13.29	-20.95	6.15	22.09	5.14
M_{Py} [nTm^3]	30.73	21.16	-30.29	-17.51	1.02
M_{Pz} [nTm^3]	2.87	3.82	2.65	3.88	3.30
χ_x [m^3]	-1.05E-04	2.10E-05	7.50E-05	1.80E-05	2.00E-06
χ_y [m^3]	-7.10E-05	-9.70E-05	1.90E-05	5.80E-05	-2.30E-05
χ_z [m^3]	-3.00E-06	3.00E-05	-1.70E-05	5.00E-06	3.00E-06

Table 28: Magnetic Parameters: Forward Flight DC Brushless Motor

Parameter	0 deg	90 deg	Average
M_{Px} [nTm^3]	-0.33	-0.01	-0.17
M_{Py} [nTm^3]	-0.71	0.60	-0.05
M_{Pz} [nTm^3]	-0.04	0.16	0.06
χ_x [m^3]	-1.43E-05	1.10E-05	-1.65E-06
χ_y [m^3]	-2.77E-05	2.75E-05	-9.89E-08
χ_z [m^3]	-2.72E-06	8.44E-06	2.86E-06

Furthermore, the largest measured values (of the four-rotor position tests) were selected and extrapolated to the potential MAD sensor locations (see Table **29**). Note the significant contribution (tail ~59 nT; wingtip ~12 nT) of the aft VTOL motors on the potential MAD

locations. There was significant difference between the magnetic dipole parameters of the forward flight gas combustion engine (Table 26) and the electric motor (Table 28). Moreover, there was a substantial difference in the magnetic fields produced at the wingtips and tail.

Table 29: Crude Field Extrapolation: Summary of Propulsion Units

	Experimental Measurements		Crude Field Extrapolation			
			Wingtip		Tail	
Aircraft Component	**Distance [m]**	**Maximum Magnetic Field [nT]**	**Distance from Source [m]**	**Maximum Field [nT]**	**Distance from Source [m]**	**Maximum Field [nT]**
Gas Combustion Engine	0.75	79.012	2.07	3.750	1.81	5.654
Forward Flight Electric Motor	0.5	0.169	2.08	0.002	1.82	0.003
Port Forward VTOL Motor	0.50	281.540	1.46	11.341	1.90	5.108
Port Aft VTOL Motor	0.50	281.540	1.43	12.140	0.84	59.314
Starboard Forward VTOL Motor	0.50	281.540	2.69	1.814	1.90	5.108
Starboard Aft VTOL Motor	0.50	281.540	2.67	1.850	0.84	59.314

3.6.1.2 Small Source Pull-Away Tests

Like the fuselage pull-away tests discussed in section 3.5.2.1, pull-away tests were used for many smaller sources. Smaller sources are defined as aircraft components that are physically small, and in most cases, have weak magnetic properties. There were two procedures used for small sources: simple pull-away (3.6.1.2.1) and flip and pull-away (3.6.1.2.2).

3.6.1.2.1 Simple Pull-Away Test

The simple pull-away test was used for small sources that are not easily reoriented. Examples of these types of sources include electrical connectors and cabling which are not easily manipulated during testing. The disadvantage of this procedure is that one cannot

obtain orientation-dependent measurements, rather assuming the test object is the point source. The Simple Pull-Away test is as follows [52]:

1. Establish test object at known distance from TF#1.
2. With all test personnel still in place, begin continuous measurements for a 15 sec baseline.
3. Move the source away from TF#1.
4. Measure background for 15 sec.

As an example, the results from the simple pull-away test is shown from the DGPS to Aft Switchboard connector (Figure 58). In Figure 59, observe that when the connecter is pulled away (initially 0.16 m from TF#1) there is 9.2 nT change in magnetic field.

Figure 58: DGPS to Aft Switchboard Connector

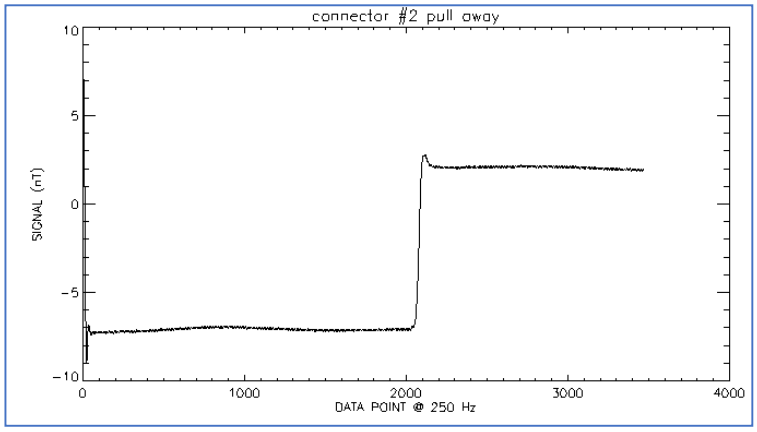

Figure 59: Simple Pull-Away Test: DGPS to Aft Switchboard Connector (Labelled Connector #2) [52]

Using a crude estimation of the permanent dipole moment $M_{P\,x}$, its value can be obtain using the following relation.

$$M_{P\,x} \approx \frac{B_{max}\, {r_{exp}}^3}{2} \quad \text{since} \quad B_{test\ object} \approx \frac{2\, M_{test\ object}}{{r_{exp}}^3}$$

Given the lack of field measurements, the sources were assumed to have only x-axis permanent magnetic components (see in Table 30). Furthermore, these field measurements can be extrapolated to potential MAD sensor locations (see Table **31**). In general, it was determined that the tested source would have negligible effects at the sensor locations.

Table 30: Magnetic Parameters: Simple Pull-Away

Aircraft Component	M_{Px} [nTm^3]	M_{Py} [nTm^3]	M_{Pz} [nTm^3]	χ_x [m^3]	χ_y [m^3]	χ_z [m^3]
Connector: Aft Switchboard to Saddle	1.33E-02	0.00	0.00	0.00	0.00	0.00
Connector: DGPS to Aft Switchboard	1.88E-02	0.00	0.00	0.00	0.00	0.00
Access Cover: Front Avionics Bay, Top	4.10E-04	0.00	0.00	0.00	0.00	0.00

Table 31: Extrapolate Fields: Simple Pull-Away

	Experimental Measurements		**Crude Field Extrapolation**			
			Wingtip		**Tail**	
Aircraft Component	**Distance [m]**	**Maximum Magnetic Field [nT]**	**Distance from Source [m]**	**Maximum Field [nT]**	**Distance from Source [m]**	**Maximum Field [nT]**
Connector: Aft Switchboard to Saddle	0.16	6.500	1.96	0.004	0.93	0.033
Connector: DGPS to Aft Switchboard	0.16	9.200	2.01	0.005	0.64	0.141
Access Cover: Front Avionics Bay, Top	0.16	0.200	2.00	1.02E-04	1.57	2.11E-04

3.6.1.2.2 Flip and Pull-Away Test

The flip and pull-away test was used for small sources that are easily reoriented. The advantage of this procedure is that one can obtain orientation-dependent measurements. The Flip and Pull-Away test is as follows [52]:

1. With all test personnel, still in place, begin continuous measurements for a 15 sec baseline.
2. Move source to 0.25 m mark (near TF #1) for 15 sec.
3. Rotate the item 180 deg while remaining at 0.25 m mark, hold for 15 sec.
4. Move the source away from TF#1.

5. Measure background for 15 sec.

As a demonstration, Figure 60 shows the measurement results from the flip and pull-away procedure for the aft bulkhead saddle fastener. The key inflections in the data are annotated in accordance with the procedure.

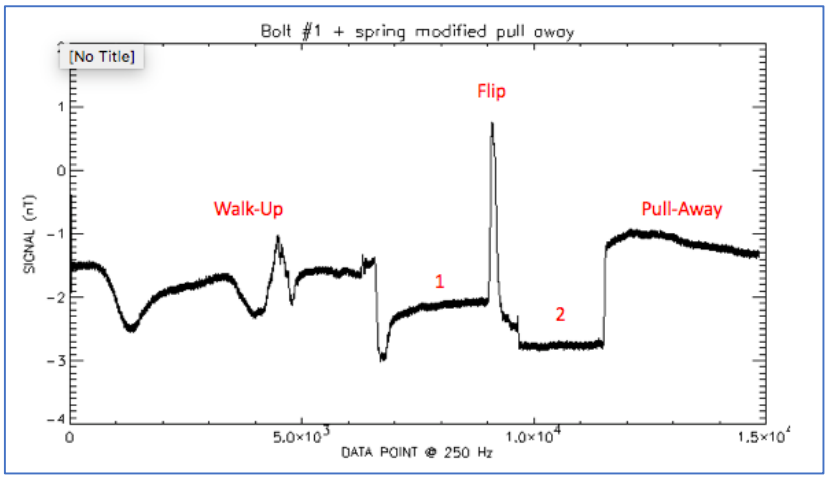

Figure 60: Flip and Pull-Away Measurement Results: Fastener: Aft Bulkhead Saddle + Spring [52]

Table 32: Flip and Pull-Away Measurement Results: Fastener: Aft Bulkhead Saddle + Spring

Parameter	**Field Measurement [nT]**	
	Uncorrected	**Average Background Removed**
Background: Start	-1.610	N/A
Orientation 1	-2.090	-0.685
Orientation 2	-2.770	-1.365
Background: End	-1.200	N/A
Background: Average	-1.405	
Maximum	-1.365	
Perm Field	0.340	
Induced Field	-1.025	

Table 32 summarizes the measurements and computed the permanent and induced fields according to the following relations. Refer to section 3.4 regarding permanent and induced magnetization in fasteners.

$$B_{perm} \approx \frac{B_1 - B_2}{2}; \; B_{ind} \approx \frac{B_1 + B_2}{2}$$

The maximum fields were also extrapolated, seen in Table 33. These relations were used to infer the magnetic parameters of the sources tests, see Table 34. Many of these test objects were found to have negligible effect at potential MAD locations. Nonetheless, they were included in the modelling results as all points in a vector field are cumulative.

Table 33: Field Extrapolation: Flip and Pull-Away

	Experimental Measurements		Crude Field Extrapolation			
			Wingtip		Tail	
Aircraft Component	**Distance [m]**	**Maximum Magnetic Field [nT]**	**Distance from Source [m]**	**Maximum Field [nT]**	**Distance from Source [m]**	**Maximum Field [nT]**
Fastener: Aft Bulkhead Saddle + Spring	0.16	1.365	1.96	7.44E-04	1.30	2.54E-03
Fastener: Belly Payload Access Cover + Spring	0.16	0.050	1.96	2.73E-05	1.30	9.30E-05
Fastener: Fwd Avionics Power Dist Board Outer Screw	0.16	0.430	1.96	2.35E-04	1.30	8.00E-04
Fastener: Engine Top Access Cover Firewall	0.16	0.050	1.96	2.73E-05	1.30	9.30E-05
Wing Joining Spar	0.25	0.050	1.96	1.04E-04	1.30	3.55E-04
Magnetic Safety Shunt	1.00	8.500	1.89	1.257	1.50	2.534

Table 34: Magnetic Parameters: Flip and Pull-Away

Aircraft Component	M_{Px} [nTm^3]	M_{Py} [nTm^3]	M_{Pz} [nTm^3]	χ_x [m^3]	χ_y [m^3]	χ_z [m^3]
Fastener: Aft Bulkhead Saddle + Spring	6.96E-04	0.00	0.00	1.30E-07	0.00	0.00
Fastener: Belly Payload Access Cover + Spring	0.00	0.00	0.00	0.00	0.00	0.00
Fastener: Fwd Avionics Power Dist Board Outer Screw	2.87E-04	0.00	0.00	3.07E-08	0.00	0.00
Fastener: Engine Top Access Cover Firewall	0.00	0.00	0.00	0.00	0.00	0.00
Wing Joining Spar	0.00	0.00	0.00	0.00	0.00	0.00
Magnetic Safety Shunt	3.49E+00	0.00	0.00	2.87E-05	0.00	0.00

3.6.2 Transient Field Noise Tests

Transient field tests refer to tests that include changing or alternating magnetic fields. This section outlines the transient field tests performed and the corresponding results.

3.6.2.1 Hand Turn Engine/Motor Tests

In lieu of running engine/motor tests, hand turning allows one to observe the magnetic effect of the internal permanent magnets and coils in motion. This is a suitable procedure when isolated engine/motor tests are not possible. This section outlines the tests completed on the gas combustion engine, forward flight electric motor (in situ), and VTOL motors.

Hand Turn Engine/Motor Test procedure is as follows:

1. Establish test source at known distance (0.50 m, for example) south of TF #1.
2. While keeping the motor firmly in place, begin turning rotor/propeller ten full rotations.
3. Move the motor to next distance mark (0.75 m).
4. Conduct ten rotations.
5. Repeat steps #2 through #3 for all distance markers (up to 2.25 m).

For demonstration, the gas engine test results are presented. Figure 61 shows the measurement plot of the hand-turn test at various distances along with a summary in Table 35.

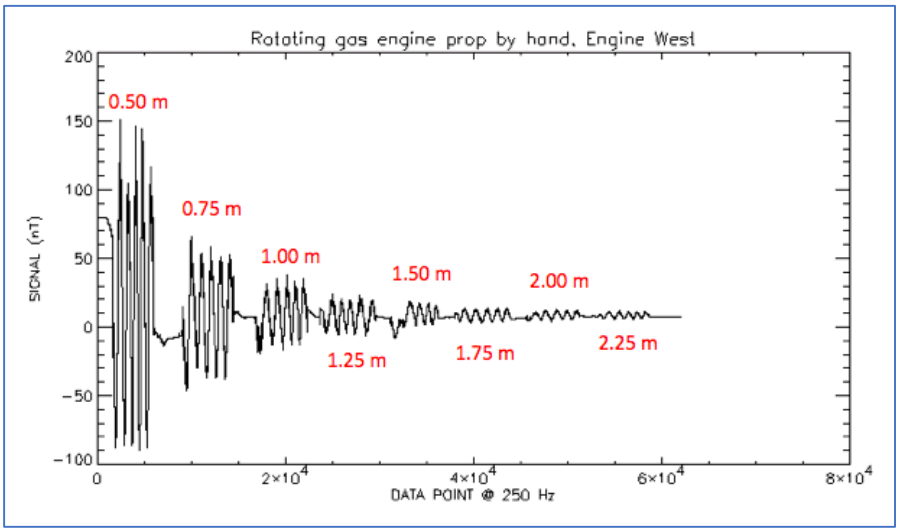

Figure 61: Hand-Turn Measurement Results: Gas Engine, Facing West [52]

The results and extrapolated results are presented in Table 36. It was predicted that the gas engine would produce a field of ~7 nT at the wingtip and ~10 nT at the tail.

Table 35: Hand-Turn Interpreted Results: Gas Engine, Facing West

	Field Measurement [nT]	
Distance South [m]	**Uncorrected**	**Average Background Removed**
0.50	29.620	21.290
0.75	7.400	-0.930
1.00	11.110	2.780
1.25	7.860	-0.470
1.50	8.790	0.460
1.75	8.330	0.000
2.00	8.330	0.000
2.25	8.790	0.460
Background: Average	8.330	

Table 36: Hand-Turn Extrapolated Results: Gas Engine, Facing West

Experimental Measurements				**Crude Field Extrapolation**			
				Wingtip		**Tail**	
Distance West [m]	**Distance South [m]**	**$\|\|R\|\|$ [m]**	**Maximum Magnetic Field [nT]**	**Distance from Source [m]**	**Maximum Field [nT]**	**Distance from Source [m]**	**Maximum Field [nT]**
0.37	0.50	0.62	231.480	2.07	6.266	1.81	9.449
0.37	0.75	0.84	90.740	2.07	5.970	1.81	9.003
0.37	1.00	1.07	50.000	2.07	6.818	1.81	10.281
0.37	1.25	1.30	26.850	2.07	6.691	1.81	10.090
0.37	1.50	1.54	15.740	2.07	6.529	1.81	9.846
0.37	1.75	1.79	11.110	2.07	7.152	1.81	10.785
0.37	2.00	2.03	7.400	2.07	7.004	1.81	10.562
0.37	2.25	2.28	6.480	2.07	8.642	1.81	13.031
				Average	6.884	**Average**	10.380

3.6.2.2 Eddy-current Tests

Another potential source of magnetic noise is eddy-currents. Many aircraft materials (aluminium, carbon fiber), despite being non-magnetic, can produce measurable magnetic signals if they are electrically-conductive. To measure eddy-currents, two tests were conducted: waving samples near the TF sensors and resistance tests with an ohmmeter.

Figure 62: VTOL Carbon Fiber Propeller

Samples of aircraft skin material or carbon fiber propeller (Figure 62) were waved in front of the TF sensors to measure the magnetic effects. Furthermore, an Ohm-meter was used to investigate the electrical conductive nature of the carbon fiber sample (see Figure 63).

Figure 63: Resistance Test on Carbon Fiber Skin Sample

Table 37 summarizes the results of the eddy-current tests. In short, no significant magnetic signals were detected. As a confirmation of the experimental procedure an aluminum tray was waved in front of the sensor, producing a (~15 nT) signal. Therefore, it can be safety assumed that the propellers and aircraft skin will not generate eddy-currents. For this reason, eddy-currents were assumed negligible and were not modelled for the Nebula N1 UAV.

Table 37: Results of Eddy-current Tests

Source	Eddy-Current Test	Observation
Carbon Fiber VTOL Propeller	Waving Near TF Sensor	Nothing Significant Observed
Carbon Fiber Sample (Similar to Fwd Fuselage + Wing)	Waving Near TF Sensor	Nothing Significant Observed
	Resistance Test	No Relationship Between Resistance and Distance
Tin Foil Aluminum Tray [Not an Aircraft Component]	Waving Near TF Sensor	15 nT peak-to-peak @ 0.05 m

3.7 Summary/Conclusions of Results

All sources of magnetic noise were identified for replacement, demagnetization or characterization. The major sources of noise were the VTOL motors and flight control servos. Major sources of concern were noted for special attention in the modelling phase. Appendix A contains all dipole parameter computed during the experimental campaign. When compared to other studies (Appendix D), the experimental result suggested that the flight control servos had a relatively low magnetic signature.

4 Analytical & Numerical Modelling, Analysis & Results

With the six magnetic dipole parameters obtained for each aircraft component (Appendix A), the representative dipole sources were collated to produce three aircraft magnetic models. The computational and numerical static-field models feature dipoles assembled in 3D space while the third model evaluates maneuver noise by comparing aeromagnetic compensation coefficients.

4.1 Aircraft Analytical Modelling: Magnetic Dipole Moments

Using established analytical solutions to approximate the field of ideal magnetic dipoles, the experimental results were collated into the following aircraft magnetic model.

4.1.1 Model Description

The total magnetic field produced by an ideal magnetic dipole of a source B_i is obtained using the following equation [8].

$$B_i = \frac{3\,(M_{total,i} \cdot r_i)(r_i \cdot B_E)}{B_E\, {r_i}^5} - \frac{(M_{total} \cdot B_E)}{B_E\, {r_i}^3}$$

Combined with the respective magnetic dipole moments $M_{total,i}$ [nTm^3] (Appendix A), the measured value for Earth's geomagnetic field B_E and the distance from each source to MAD location r, the total magnetic field of all sources $B_{total,MAD\ \#1}$ can be estimated. This relation was used to evaluate the combined effect of all measured sources at various MAD locations. The evaluation procedure is summarized below:

1. For each magnetic source (*i, j,* ...) and each potential MAD payload location *(MAD#1, MAD#2,* ...), extrapolate the scalar magnetic noise ($B_{i,MAD\#1}$, $B_{j,MAD\#1}$, $B_{i,MAD\#2}$, $B_{j,MAD\#2}$, …) using the distance from source to the MAD location, see Figure 64.
2. Sum the magnetic noise contributions from each source at each potential MAD location.

$$B_{total,MAD\ \#1} = \sum (B_{i,MAD\#1} + B_{j,MAD\#1} + \cdots)$$

$$B_{total,MAD\ \#2} = \sum (B_{i,MAD\#2} + B_{j,MAD\#2} + \cdots)$$

3. Compare the total magnetic noise value at each potential MAD location $(B_{total,MAD\ \#1}, B_{total,MAD\ \#2})$.

   If $B_{total,MAD\ \#1} < B_{total,MAD\ \#2}$ → Chose MAD #1

   If $B_{total,MAD\ \#1} > B_{total,MAD\ \#2}$ → Chose MAD #2

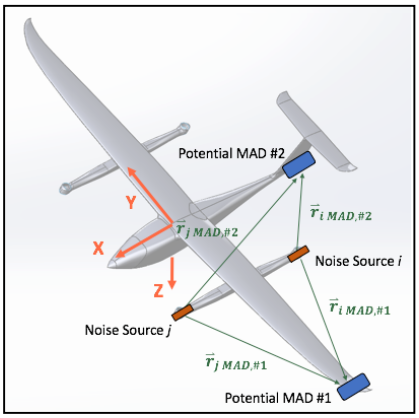

Figure 64: Geometric Evaluation of Potential MAD Configurations (Modified From [14])

4.1.2 Model Assumptions

This model evaluates the static magnetic field of the aircraft using dipole equations. It was assumed that every source can be accurately modelled by an ideal point source dipole. Moreover, all magnetic dipoles were assembled using an assumption of superposition, aligned with magnetic north. The background magnetic field B_E values used to compute the magnetic fields were specific to the temporal conditions during the time of testing.

In the dipole moment equations, only permanent and induced magnetic aspects were computed, while eddy-currents were not. Based on the eddy-current tests conducted (section 3.6.2.2), no significant eddy-currents were observed. Furthermore, it has been found generally that UAVs of this size, and material type, produce negligible eddy-current noise [32].

4.1.1 Aircraft Computational Dipole Model Results

Using the experimentally-obtained magnetic dipole parameters (Appendix A), a series simple visualizations were produced. Plotted per the aircraft geometry, Figure 65 presents the magnitudes of magnetic dipole moments. The radius of the red circles is directly

proportional to the magnitude of the total magnetic dipole moment $\|M_{total,i}\|$. An overlay of the aircraft outer model line is provided for visualization.

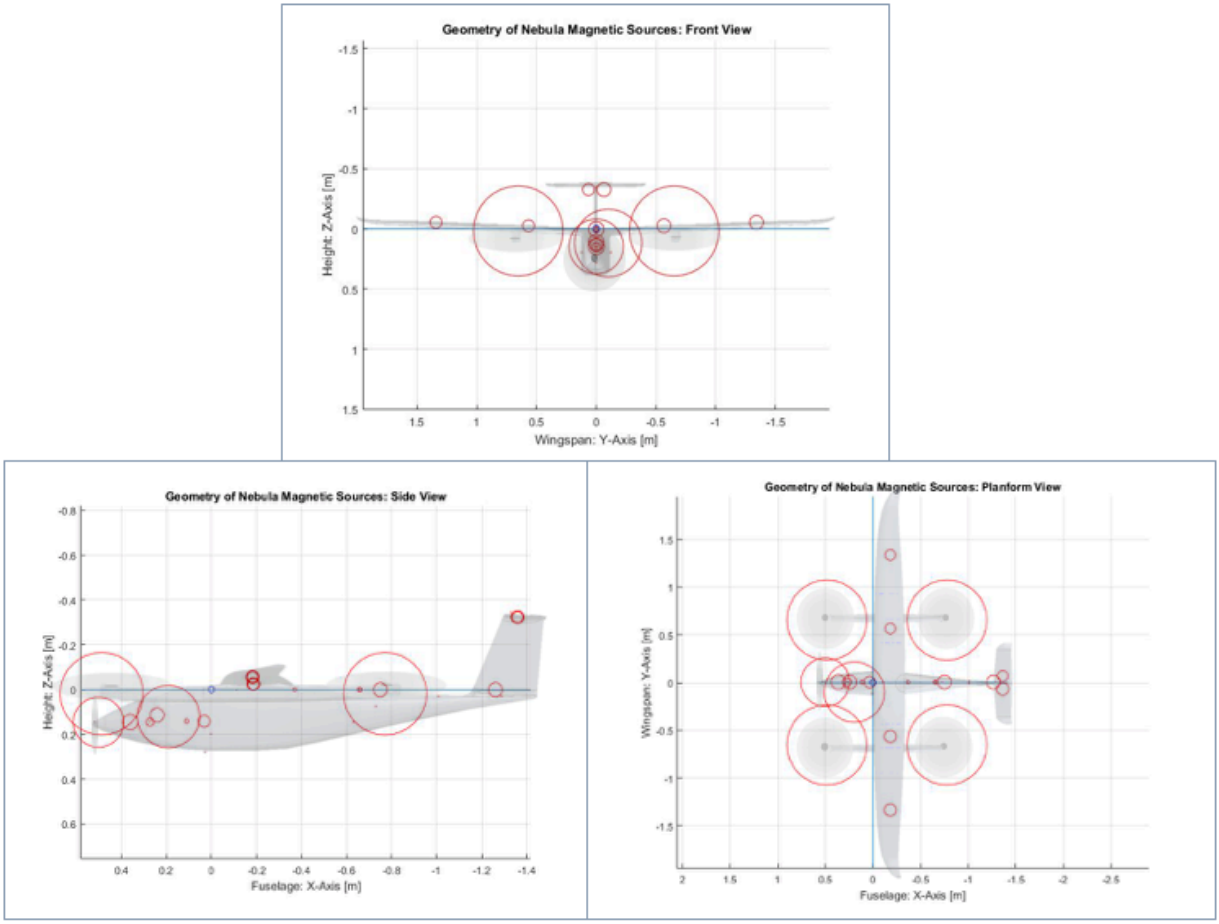

Figure 65: Scatter Plot: Gas-VTOL Configuration

Observe the large contribution of the DC brushless VTOL motors and the forward flight gas combustion engine. Within the fuselage there are scattered sources between the forward and aft avionics bays. Along wing and tail surfaces, the flight control servos are the small and symmetrically distributed. An interesting observation came from the magnetic safety shunt located on the port-side near the forward flight engine. This is a remove-before-flight magnet that produced a large dipole moment. The magnetic shunt was included in these plots purely for demonstration purposes.

4.2 Aircraft Numerical Modelling with COMSOL Multiphysics

COMSOL is a commercial multiphysics finite element analysis software. Within the COMSOL AC/DC module, magnetic dipole models were constructed using *Magnetic Fields* physics and a reduced-field formulation [71], [72].

4.2.1 Model Description & Assumptions

This model evaluates the static magnetic field of the aircraft using magnetostatic point dipoles. Similar to the aforementioned aircraft magnetic model, experimentally-obtained dipole parameters were arranged as point sources according to the aircraft geometry. Within COMSOL, dipole moment values m_{COMSOL} are entered in ampère per metre squared [Am^2]. However, the dipole equations used to compute the magnetic dipole moment m_{EXP} used nanoteslas per metre cubed [nTm^3]. A unit conversion factor is provided below.

$$m_{COMSOL}[\mathrm{Am^2}] = 10^7\, m_{EXP}[\mathrm{nTm^3}]$$

Furthermore, all dipole models were surrounded by two concentric spherical domains of air, see Figure 66. The inner layer immediately surrounding the magnetic dipole(s) was named the Analysis Domain, as that is where the magnetic fields were computed. The outer layer, named the Infinite Domain, was meshed using infinite elements. Infinite elements provide a means for the magnetic flux to decrease to negative infinity [27].

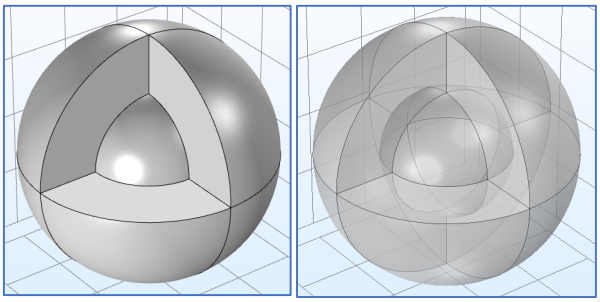

Figure 66: Simple Magnetic Dipole Simulation Set-Up

Using "extremely fine" physics-controlled meshing and a series of probes, the magnetic flux density norm was computed at various distances around the aircraft. Furthermore, as a starting point a simple set of single magnetic dipole were simulated and compared to the analytical solutions, see Appendix B.

4.2.2 Aircraft Magnetic Dipole Simulation Results

This section outlines the aircraft magnetic signature results from the COMSOL numerical simulation. In all following figures, the aircraft shell was only imported for ease of visualization. The aircraft shell was meshed using elements of air and it did not contribute to the physics at all. In this model, it is the magnetic flux density norm that is being plotted.

In Figure 67, observe the magnetic fields annotated in semi-transparent coloured 100 nT isosurfaces. The prominent VTOL motors seemed to have merged with the forward flight gas engines. Along the wing and tail surfaces, the flight control servos are represented while assorted avionics are distributed throughout the fuselage. Note the similarity between models in Figure 67 and Figure 65, supporting COMSOL model fidelity.

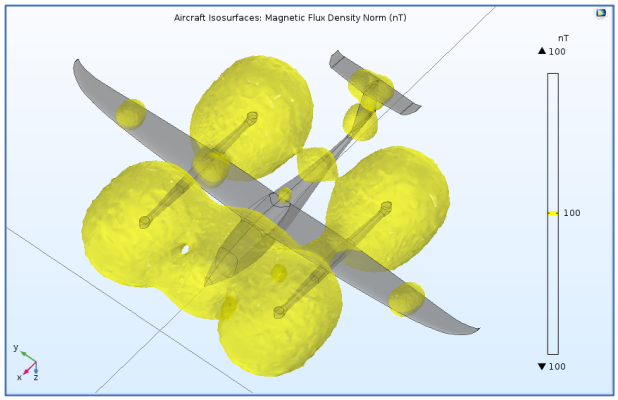

Figure 67: COMSOL – Aircraft Isosurfaces – 100 nT

Furthermore, Figure 68 displays an XY-plane slice positioned below the aircraft at $Z = 0.5$ m. This figure amplifies the significant effect that the propulsive units have on the magnetic signature of the aircraft.

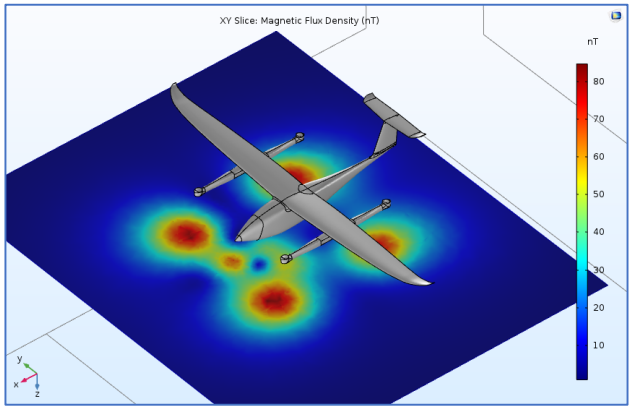

Figure 68: COMSOL – XY Slice ($Z = 0.5$ m) – 80 nT

4.3 Aircraft Tolles & Lawson Aeromagnetic Compensation Coefficients

To quantity the movement-induced magnetic maneuver noise experienced in-flight, Tolles and Lawson (T&L) aeromagnetic compensation coefficients were computed and compared. The T&L model encompasses the geometric and magnetic properties of the aircraft to which the magnetic noise at each potential MAD sensor location can be evaluated [41].

4.3.1 Model Description

The T&L model encompasses the permanent, induced and eddy-current noise due to aircraft maneuvers. By computing the T&L compensation coefficients, the maneuver noise of the aircraft can be evaluated. Recall that the magnitude of the induced and eddy-current effects are proportional to the time rate of change of magnetic flux within the aircraft [41]. The T&L model predicts the total movement noise $B_{MOVE}(t)$ which can be later removed from the raw signal measured by the MAD sensor $B_{MAD,raw}$ to obtain the uncontaminated signal $B_{MAD,clean}$.

$$B_{MAD,compensated} = B_{MAD,raw} - B_{MOVE}(t)$$

The total movement noise at MAD location $H_{MOVE}(t)$ can be expressed below as the sum of the respective noise sources [41].

$$B_{MOVE}(t) = B_{PERM}(t) + B_{IND}(t) + B_{EDDY}(t)$$

The full 18-term T&L interference model can be generalized below.

$$B_{MOVE}(t) = \sum_{i=1}^{18} C_i A_i(t)$$

For each potential MAD location, the T&L coefficients C_i quantify the constant interference experienced at the MAD sensor, while the T&L terms A_i are a set of real-time magnetic field coefficients [9], [41]. The T&L model can be scaled depending on the noise sources considered.

Table 38: Summary of T&L Terms

C_i	**Movement Noise Source**
$1 \leq i \leq 3$	Permanent Noise - $B_{PERM}(t)$
$4 \leq i \leq 9$	Induced Noise - $B_{IND}(t)$
$10 \leq i \leq 18$	Eddy-Current Noise - $B_{EDDY}(t)$

Table 38 summarizes the eighteen T&L coefficients C_i, capturing the geometric and magnetic properties unique to each aircraft configuration. The first three terms of the T&L model permanent magnetic noise as outlined below.

$$B_{PERM}(t) = A_1(t)C_1 + A_2(t)C_2 + A_3(t)C_3$$

The next six coefficients model the induced magnetic noise:

$$B_{IND}(t) = A_4(t)C_4 + A_5(t)C_5 + A_6(t)C_6 + A_7(t)C_7 + A_8(t)C_8 + A_9(t)C_9$$

The final ten coefficients model the eddy-current noise:

$$H_{EDDY}(t) = A_{10}(t)C_{10} + A_{11}(t)C_{11} + A_{12}(t)C_{12} + A_{13}(t)C_{13} + A_{14}(t)C_{14} + A_{15}(t)C_{15} + A_{16}(t)C_{16} + A_{17}(t)C_{17} + A_{18}(t)C_{18}$$

In the case of the Nebula N1 UAV, only the permanent and induced terms were computed. Similar to the two previous magnetic models, eddy-currents were considered negligible based on the experimental results (section 3.6.2.2). Thus, only T&L coefficients 1 through 9 were computed. To define the real-time A_i terms, a new coordinate system must be defined. An aircraft-centric reference system is used, seen in Figure 33, whereby L, T and V are the longitudinal, transverse and vertical axes, respectively. The origin was placed at the leading-edge wing root with the L-axis projecting forward towards the nose, T-axis towards the starboard wingtip, and V-axis downwards. Additionally, the components of the Earth's geomagnetic field (as observed by the vehicle) can be described using $B_{E,L}, B_{E,T}, B_{E,V}$ and the magnitude of the Earth's total magnetic field B_E is defined with respect to the aircraft's real-time maneuvers as seen below [41].

$$B_E(t) = \sqrt{\overrightarrow{B_{Ex}(t)}^2 + \overrightarrow{B_{Ez}(t)}^2 + \overrightarrow{B_{Ez}(t)}^2} = \sqrt{\overrightarrow{B_{E,L}(t)}^2 + \overrightarrow{B_{E,T}(t)}^2 + \overrightarrow{B_{E,V}(t)}^2}$$

As the vehicle pitches, rolls and yaws in flight, $B_{E,L}$, $B_{E,T}$ and $B_{E,V}$ change with time.

Like the other models, eddy-currents were assumed to be negligible based on the experimental results. For the T&L aeromagnetic compensation model, only permanent and induced magnetic components were considered. These values can also be expressed into a set of real-time (normalized) magnetic field terms A_i [9]:

$$A_1(t) = \frac{B_{E,L}}{\|B_E\|}\ ; A_2(t) = \frac{B_{E,T}}{\|B_E\|}\ ; A_3(t) = \frac{B_{E,V}}{\|B_E\|}\ ; A_4(t) = \frac{B_{E,L}\,B_{E,L}}{\|B_E\|}\ ; A_5(t) = \frac{B_{E,L}\,B_{E,T}}{\|B_E\|}\ ;$$

$$A_6(t) = \frac{B_{E,L}\,B_{E,V}}{\|B_E\|}\ ; A_7(t) = \frac{B_{E,T}\,B_{E,T}}{\|B_E\|}\ ; A_8(t) = \frac{B_{E,L}\,B_{E,V}}{\|B_E\|}\ ; A_9(t) = \frac{B_{E,V}\,B_{E,V}}{\|B_E\|}\ .$$

Finally, the nine constant T&L coefficients can be defined. These coefficients are defined in terms of the permanent dipole moments $M_{P\,i}$ and directional magnetic susceptibilities $\mathcal{X}_i$ [32].

$$C_1 = \frac{3\,(M_{total,i}\cdot r_i)x_i}{{r_i}^5} - \frac{M_{P\,xi}}{{r_i}^3};\; C_2 = \frac{3\,(M_{total,i}\cdot r)\,y_i}{{r_i}^5} - \frac{M_{P\,yi}}{{r_i}^3};\; C_3 = \frac{3\,(M_{total,i}\cdot r_i)\,z_i}{{r_i}^5} - \frac{M_{P\,zi}}{{r_i}^3};$$

$$C_4 = \frac{3\,k_x\,x^2}{{r_i}^5} - \frac{\mathcal{X}_{xi}}{{r_i}^3};\; C_5 = \frac{3\,(\mathcal{X}_{yi}\,x^2+\mathcal{X}_{xi}\,y^2)}{{r_i}^5};\; C_6 = \frac{3\,(\mathcal{X}_{zi}\,x^2+\mathcal{X}_{xi}\,z^2)}{{r_i}^5};$$

$$C_7 = \frac{3\,\mathcal{X}_{yi}\,y^2}{{r_i}^5} - \frac{\mathcal{X}_{yi}}{{r_i}^3};\; C_8 = \frac{3\,(\mathcal{X}_{zi}\,y^2+\mathcal{X}_{yi}\,z^2)}{{r_i}^5};\; C_9 = \frac{3\,\mathcal{X}_{zi}\,z^2}{{r_i}^5} - \frac{\mathcal{X}_{zi}}{{r_i}^3}.$$

The evaluation procedure is summarized below:

1. For potential MAD sensor location *(#1, #2, ...)* and each magnetic source (*i, j, ...*), evaluate each of the T&L coefficients ($C_{1,MAD\#1,i}$, $C_{1,MAD\#2,i}$, $C_{2,MAD\#1,j}$, $C_{2,MAD\#2,j}$, …) using the distance from source to the MAD location, similar to Figure 64.
2. Sum all T&L coefficients from each potential MAD location.

   For MAD #1:

$$C_{1,MAD\#1} = \sum\left(C_{1,i} + C_{1,j} + \cdots\right)_{MAD\#1}$$

$$\cdots$$

$$C_{9,MAD\#1} = \sum\left(C_{9,i} + C_{9,j} + \cdots\right)_{MAD\#1}$$

   For MAD #2:

$$C_{1,MAD\#2} = \sum\left(C_{1,i} + C_{1,j} + \cdots\right)_{MAD\#2}$$

$$\cdots$$

$$C_{9,MAD\#2} = \sum\left(C_{9,i} + C_{9,j} + \cdots\right)_{MAD\#2}$$

3. Obtain the total permanent and induced T&L coefficient values. Sum the absolute value of T&L coefficients noting that permanent and induced coefficients are summed differently.

   For permanent coefficients (C_1:C_3):

$$C_{perm,MAD\#1} = \sum\left(\left|C_{1,MAD\#1}\right| + \left|C_{1,MAD\#1}\right| + \left|C_{1,MAD\#1}\right|\right)$$

$$C_{perm,MAD\#2} = \sum\left(\left|C_{1,MAD\#2}\right| + \left|C_{1,MAD\#2}\right| + \left|C_{1,MAD\#2}\right|\right)$$

For induced coefficients (C_4:C_9):

$$C_{ind,MAD\#1} = \sum\left(\left|C_{4,MAD\#1}\right| + \cdots + \left|C_{9,MAD\#1}\right| \right) * \|B_e\|$$

$$C_{ind,MAD\#2} = \sum\left(\left|C_{4,MAD\#2}\right| + \cdots + \left|C_{9,MAD\#2}\right| \right) * \|B_e\|$$

4. Compare the total permanent and induced T&L coefficient values at each potential MAD location ($B_{total,MAD\ \#1}, B_{total,MAD\ \#2}$).

   If $C_{perm,MAD\#1} < C_{perm,MAD\#2}$ && $C_{ind,MAD\#1} < C_{ind,MAD\#2}$ → Chose MAD #1

   If $C_{perm,MAD\#1} > C_{perm,MAD\#2}$ && $C_{ind,MAD\#1} > C_{ind,MAD\#2}$ → Chose MAD #2

4.4 Noise Prediction at Potential MAD Sensor Locations

As a primary objective of this study, the magnetic models were used to predict areas of lowest magnetic interference. This section describes the methodology used to evaluate the static-field and maneuver noise at various payload locations.

4.4.1 Evaluation of Potential MAD Sensor Locations

When integrating new payloads, it behooves the professional engineer to evaluate all possible payload configurations. Section 1.2.1 outlines existing MAD configurations for manned and unmanned aircraft in both civilian and military applications. The towed configuration has the advantage of maximizing distance from the aircraft but suffers from movement induced noise, positional errors and a risk of losing magnetometer due to Canadian icing conditions [42]. Thus, the towed configuration was unrealistic for this low level fixed-wing UAV application; hence, only rigid body designs were considered. While many outside-the-box configurations were considered, many were deemed unfeasible for various aerodynamic, structural and operational reasons. For example, in [8] it was suggested that the MAD sensor could be placed above the fuselage for safety reasons. This configuration was quickly rejected given the presence of the highly magnetic VTOL motors near the fuselage and the out-of-plane aerodynamic drag implications. Thus, only conventional fixed-wing MAD configurations, being wingtip and tail placements, were considered. Using the aircraft magnetic signature models, the magnetic noise was predicted at these potential MAD locations.

4.4.2 Case #1: Tail Position

This section describes the geometric evaluation and studies on the tail position. Using the analytical model, the constituent parts of the net magnetic field were predicted at the tail. Figure 69 depicts a pie chart where the absolute value of all contributions was divided by the absolute sum of all contributions. Observe the overwhelming contribution (96%) of the rudder flight control servo. The proximity of the rudder servo causes this extreme result and overtakes the VTOL contribution.

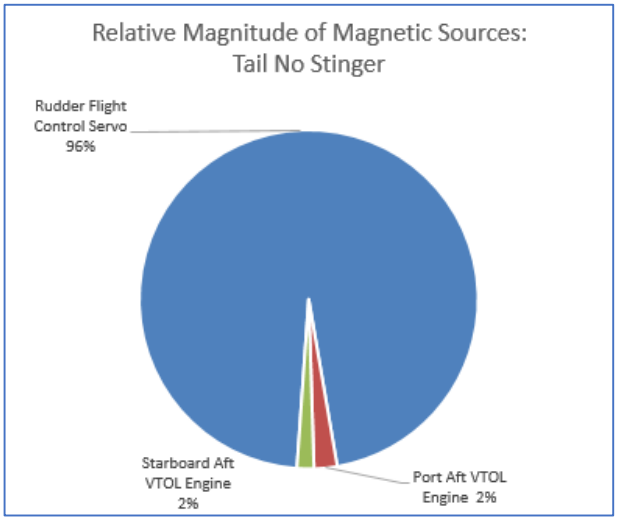

Figure 69: Relative Magnitude of Magnetic Sources Contributions – Tail

Next, Figure 70 annotates the magnetic source geometry, similar to Figure 65, whereby the radius of the red circles is proportional to the magnitude of the dipole moments divided by the inverse cube of the distance. Due to the overwhelming effect of the rudder flight control servo, and for demonstration, this figure has been evaluated 0.2 m aft of the tail (annotated by the black asterisk). When evaluated at the tail, the entire area of the chart was filled with red obscuring the entire plot. A similar effect was observed with nearby VTOL motors and tail control surfaces in the crude field extrapolations in Table 24 and Table **29**.

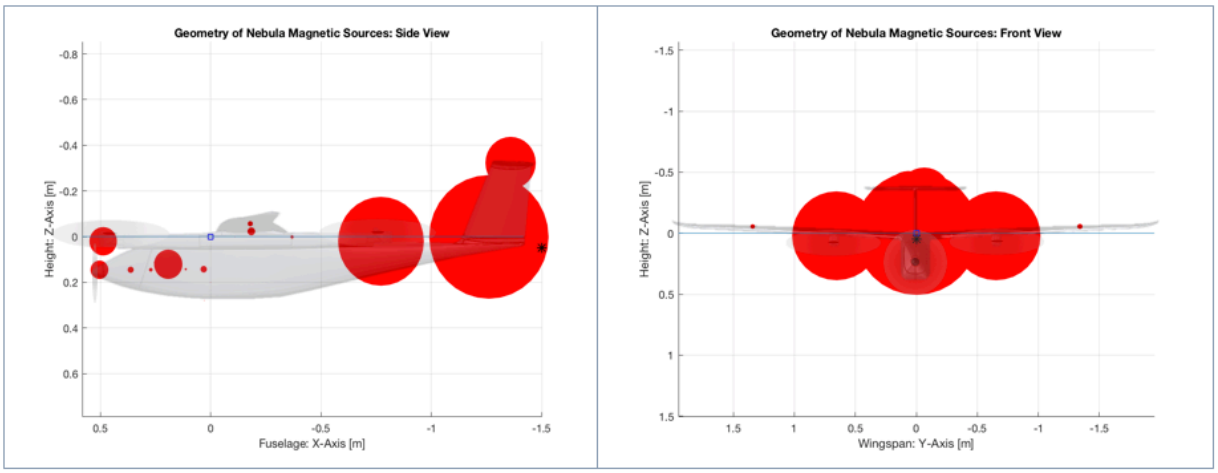

Figure 70: Scatter Plot, Normalized to Distance from Tail Stinger at 0.2 m

For added visualization effect, the numerical simulation was employed to examine the field contributions near the tail. Using isosurfaces, Figure 71 shows the magnitude of magnetic fields aft of the rear VTOL motors, avionics and flight control servos near the tail, in hundreds of nT. These isosurfaces are cut (VTOL at x = -0.8m, servos at x = -1.3 m) to observe the density of isosurfaces within. The rudder flight control servo located at the base of the tail would cause significant magnetic noise for any tail placement.

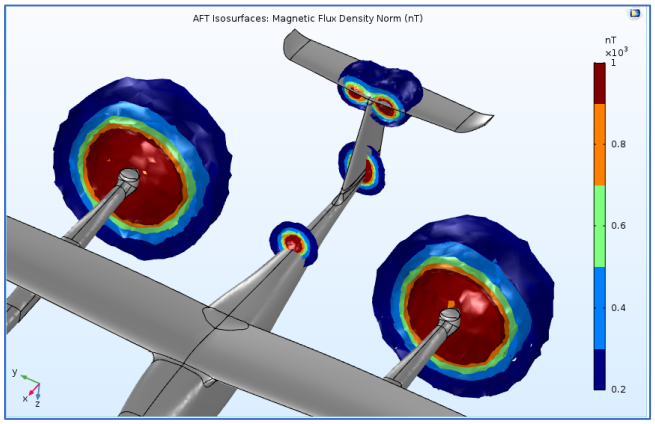

Figure 71: COMSOL – Isosurfaces Near the Tail – 1000 nT

Table 39 presents the results between the analytical and numerical models. The large error between models was initially concerning. The immediate proximity of the sources and the observation point suggest that the models suffer from discrepancies in the near-field.

Table 39: Comparison of Results – Tail

	Magnetic Flux Density Norm [nT]		
	Analytical	**Numerical**	**Error**

Tail	245.20	1279.25	80.8%

4.4.2.1 Tail Geometric Sensitivity

Due to the large fields predicted at the tail and the inverse cube law associated with magnetic field decay, the geometric sensitivity of a stinger boom was examined. Figure 72 shows the geometry of the tail geometric sensitivity whereby various lengths of stinger booms were trialled. All three magnetic models were employed for this analysis.

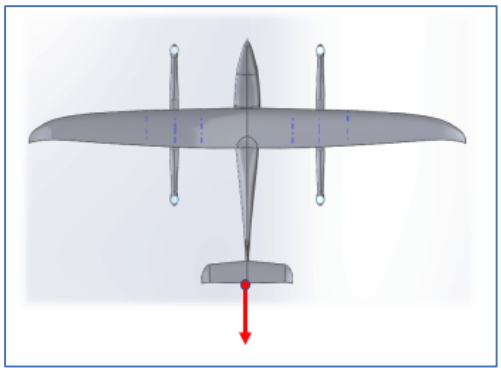

Figure 72: Tail Geometric Sensitivity Analysis

Figure 73 and Table 40 show a comparison between analytical and numerical simulation results for the tail stinger geometric sensitivity. While the error between the two varies, stinger positions #1 and #2 averaged just below 15% error. Given the complexity of the magnetic interactions and the undefined far-field, these results were generally accepted as valid. Based on the analytical results, a stinger boom greater than 0.4 m would be required to reduce the static magnetic field to the acceptable limit (< 2 nT). Contrasting that with the numerical results, a stinger boom of approximately 1.65 m would be required.

Table 40: Tail Stinger – Comparison of Computational and Analytical Results

		Magnetic Flux Density Norm [nT]		
	Length [m]	**Analytical**	**Numerical**	**Error**
Tail Stinger #1	0.1	60.94	70.43	13.5%
Tail Stinger #2	0.2	17.73	19.73	10.1%
Tail Stinger #3	0.3	8.13	13.05	37.7%
Tail Stinger #4	0.4	4.57	10.84	57.9%
Tail Stinger #5	0.5	2.79	9.32	70.1%
Tail Stinger #6	0.6	1.77	8.00	77.8%

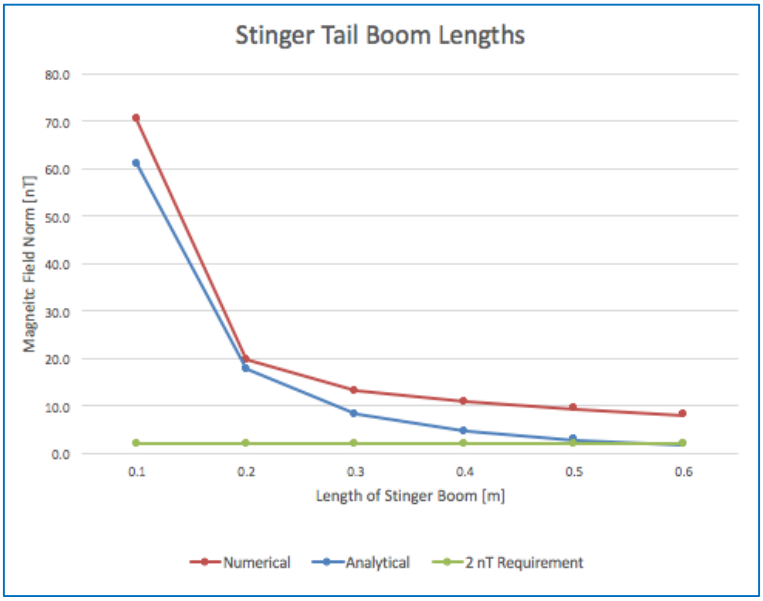

Figure 73: Tail Stinger Boom – Compare Analytical and Numerical Simulation

Figure 74 shows a series of slices to emphasize the sensitivity of the tail boom lengths, for -1.1 < *x* < -2.9. The mid-point of the slice (x ≈ -2.0) shows a value of approximately 7 nT and decays towards 2 nT at the end (x ≈ -2.9). The fields predicted at the tail and along the stinger are quite large without a substantial separation distance.

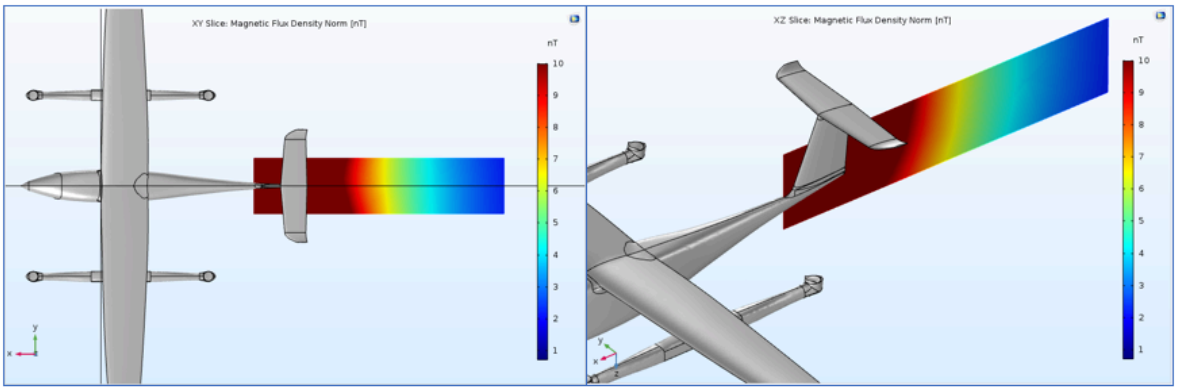

Figure 74: COMSOL – Tail Stinger Sensitivity Analysis – 10 nT (-1.1 < *x* < -2.9)

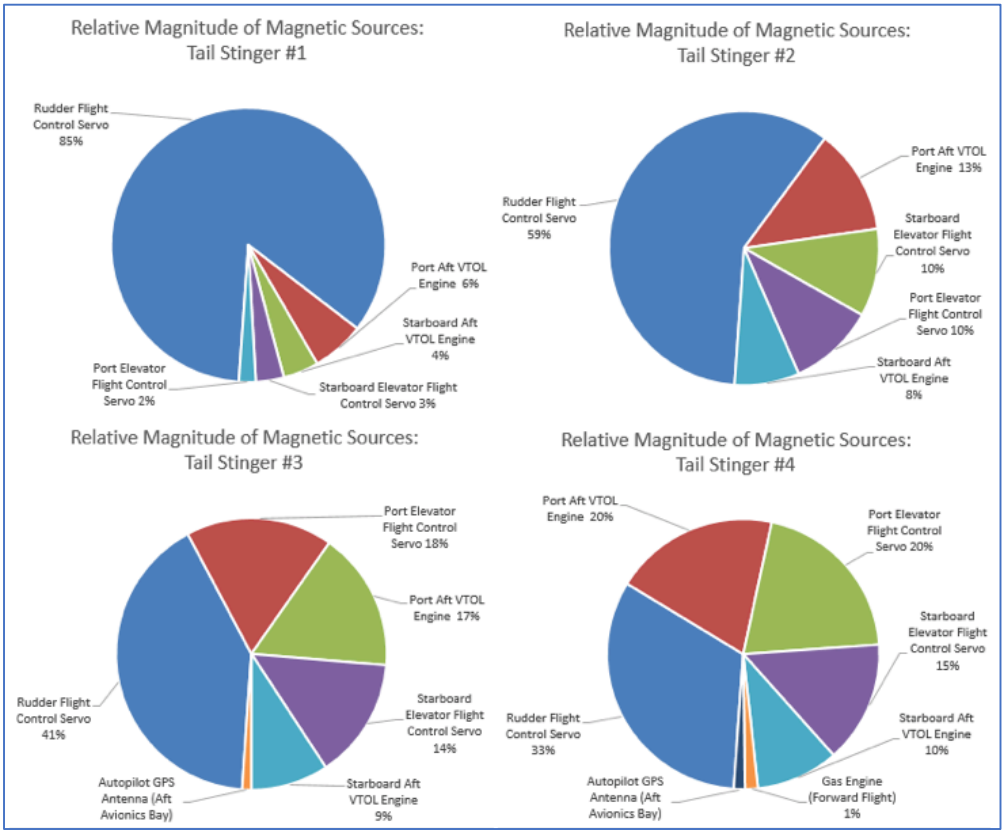

Figure 75: Relative Magnitude of Magnetic Source Contributions – Tail Stinger Booms

Figure 75 is provided to observe how the effect of rudder flight control servo decreases with increasing stinger boom length. For example, at Stinger #1 it represents 85% of the predicted field while at Stinger #4 it falls to 33%. The reader is cautioned in reviewing these charts, as it is the relative contribution of the other components that is increasing and not the magnitude of their fields.

Table **41** shows the results of the T&L assessment for the tail boom sensitivity analysis. While the values may seem trivial, it is the significant decrease in coefficient values that is of importance. The absolute sum of T&L coefficients is directly proportional to the movement noise experienced at each position evaluated.

Table 41: T&L Absolute Value Coefficient Results from Tail Boom Analysis

MAD Location		Absolute Value of T&L Coefficient										
		PERMANENT				INDUCED						
	Dist [m]	C_1	C_2	C_3	SUM	C_4	C_5	C_6	C_7	C_8	C9	SUM
Tail	**N/A**	738.6	62.33	519.80	1320	2.25E-04	1.51E-03	8.66E-03	1.45E-03	2.56E-03	4.09E-03	999.19
Stinger #1	**0.1**	38.08	4.19	32.32	74.60	2.61E-04	2.82E-04	1.16E-03	1.78E-04	6.03E-05	2.12E-04	116.16
Stinger #2	**0.2**	1.03	0.39	15.08	16.50	8.70E-05	5.76E-05	3.60E-04	6.97E-05	2.14E-05	5.68E-05	35.22
Stinger #3	**0.3**	6.12	1.20	9.12	16.44	5.92E-05	1.19E-05	1.76E-04	3.75E-05	1.07E-05	2.43E-05	17.25
Stinger #4	**0.4**	6.93	6.10	6.39	19.42	5.01E-05	2.42E-06	1.03E-04	2.17E-05	4.60E-06	1.61E-05	10.68

4.4.3 Case #2: Wing Position

This section describes the geometric evaluation and studies on the wingtip position. Similar to Figure 65, Figure 76 annotates the magnetic source geometry however normalized to the MAD location (annotated by the black asterisk). The radius of the red circles is proportional to the magnitude of the dipole moments divided by the inverse cube of the distance. Based on the figure, one can see that the VTOL and flight control servos would be most significant for wingtip sensors. For instance, if the MAD payload were on the port wingtip, the port-side VTOL motors and ailerons would cause the most noise. A similar effect was observed with nearby VTOL motors and wing control surfaces in the crude field extrapolations in Table 24 and Table 29.

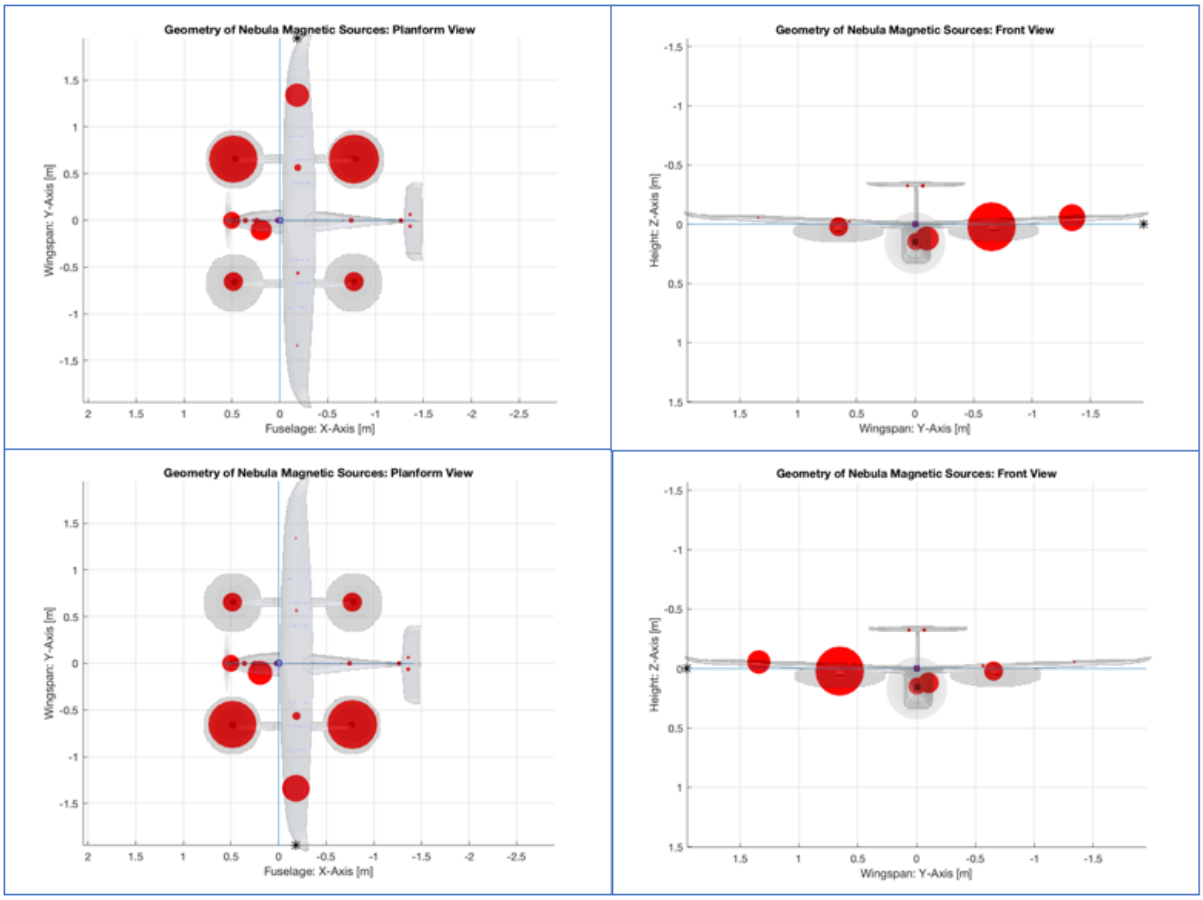

Figure 76: Scatter Plot, Magnitude of Dipole Moments, Normalized to Distance from Wingtips: Starboard MAD (top), Port MAD (bottom)

Table 42 compares the results between analytical and numerical simulation results for the wingtips. Comparing Table 39 and Table 42, the magnetic field values are much lower for wingtips versus tail positions. Note the difference between the port and starboard wingtip predictions. This difference was expected as the magnetic safety shunt was included in the models to demonstrate its strong effect on the aircraft's magnetic signature. During flight, one would expect that this permanent magnet would be removed from the aircraft.

Table 42: Predicted Magnetic Noise at Wingtip Locations

	Magnetic Flux Density Norm [nT]		
	Analytical	**Numerical**	**Error**
Port Wingtip	3.05	3.77	19.2%
Starboard Wingtip	2.86	3.29	13.1%

Furthermore, we can investigate the constituent parts of the magnetic field predicted at each wingtip. Figure 77 shows pie charts with the relative magnitudes of each field contribution for both port and starboard wingtips. Note that the pie charts depicted here evaluate the absolute value of all contributions divided by the absolute sum of all contributions. In line with the previous figures, we can see that proximity of the VTOL motors pairs contributes almost 75% of the predicted field for each wingtip. Rounding out the last 25 % are other VTOL motor pairs, ailerons flight control servos and the magnetic safety shunt. Despite being flagged as remove-before-flight, the safety shunt was included in the pie charts for demonstration.

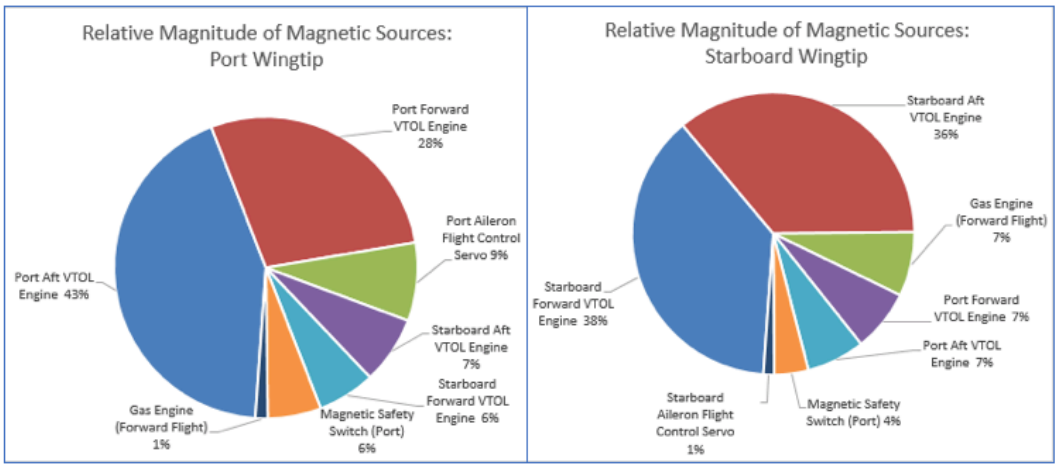

Figure 77: Relative Magnitude of Magnetic Sources Contributions – Port and Starboard Wingtips

Figure 78 shows the magnitude of magnetic fields mid-chord along the span of the wing from 1 to 10 nT. Focusing on the outboard sections of the wing, one can observe of the magnitude of magnetic field decreases towards the wingtip.

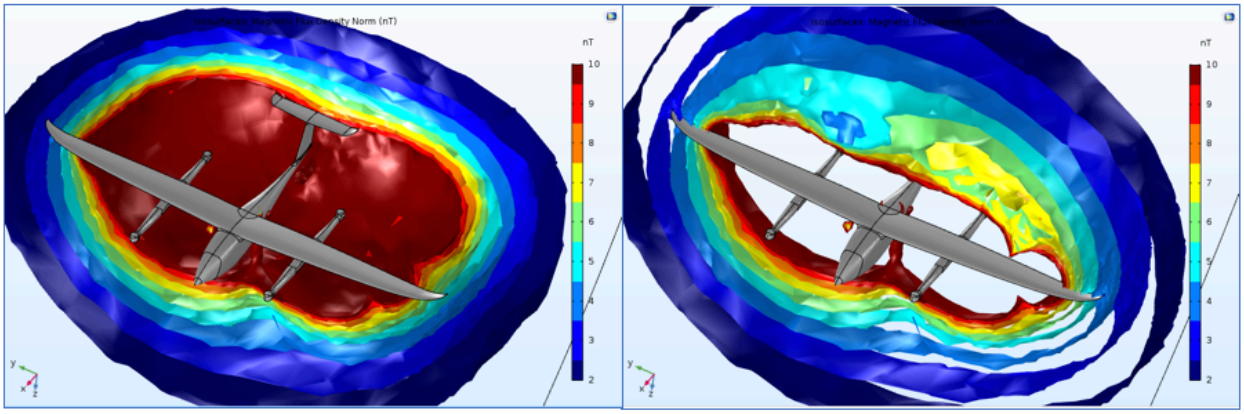

Figure 78: COMSOL – Isosurface Shells Aft of Mid-Wing Chord & Outboard Wing Section – 10 nT

Figure 79 clearly shows the magnetic field along the wingspan. Observe that fields less than 10 nT are predicted at the wingtips, which is much less severe than a tail position.

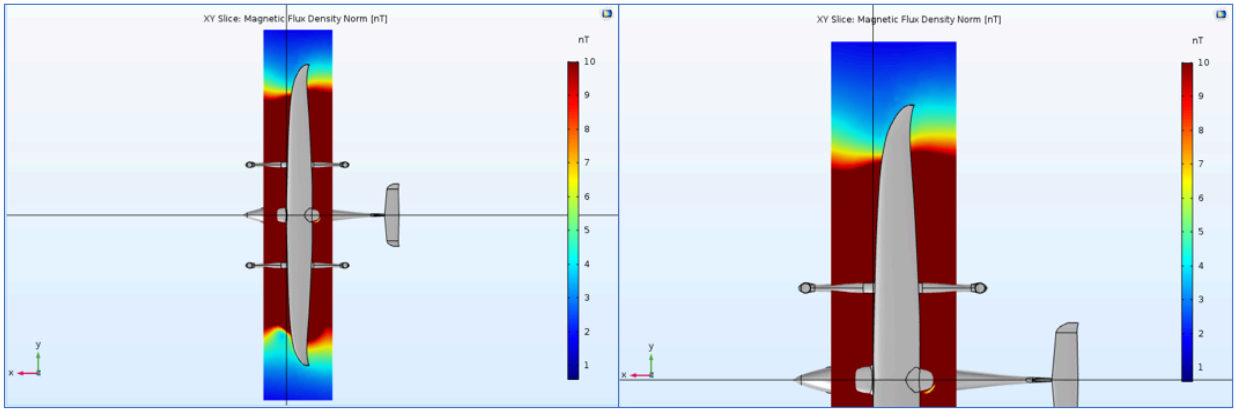

Figure 79: COMSOL – XY Slices – 10 nT (-2.4 < y < 2.4)

Furthermore, the T&L coefficients show similar results. Comparing

Table **41** and Table 43, the T&L coefficient absolute sums for the wingtips are much lower than any tail stinger positon evaluated.

Table 43: T&L Absolute Value Coefficient Results from Wingtips

MAD Location	Absolute Value of T&L Coefficient										
	PERMANENT				INDUCED						
	C_1	C_2	C_3	SUM	C_4	C_5	C_6	C_7	C_8	C_9	SUM
Port Wingtip	2.26	1.68	1.68	5.62	1.55E-05	5.07E-05	3.37E-06	1.62E-06	3.56E-05	1.26E-05	6.45
Starboard Wingtip	1.20	2.03	1.89	5.12	1.55E-05	5.05E-05	3.37E-06	2.95E-07	3.56E-05	1.26E-05	6.36

4.4.3.1 Wing Geometric Sensitivity

In this study, the effect of moving the MAD sensor forward, aft and inboard was studied. The motivation for this study was to reduce the bending moment at the wing root by placing the sensor further inboard. Figure 80 shows the geometry of the results presented in Table 44. Again, large errors observed close to magnetic sources (Inboard Wing #1 and #2) due to near-field effects. The error then tapered to less than 15% from Inboard Wing #3 through Outboard Wing #4.

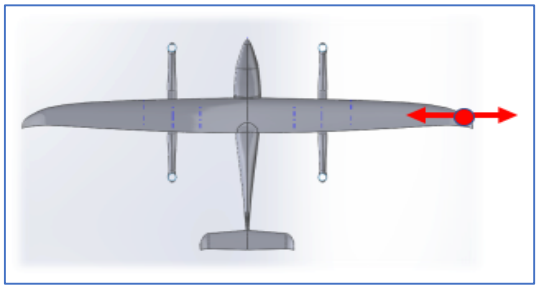

Figure 80: Geometry of Wingtip Sensitivity Analysis

Table 44: Comparison of Analytical and Numerical Results

		Magnetic Flux Density Norm [nT]		
	Length [m]	Analytical	Numerical	Error
Inboard Wing #1	-0.4	2.98	13.91	78.6%
Inboard Wing #2	-0.3	4.00	6.22	35.8%
Inboard Wing #3	-0.2	3.71	4.42	15.9%
Inboard Wing #4	-0.1	3.28	3.68	10.8%
Starboard Wingtip	0	2.86	3.29	13.1%
Outboard Wing #1	0.1	2.49	2.89	13.8%
Outboard Wing #2	0.2	2.17	2.53	14.3%
Outboard Wing #3	0.3	1.89	2.17	12.8%
Outboard Wing #4	0.4	1.66	1.92	13.9%

Figure 81 plots the favourable portion of the span wise wing analysis with the 2 nT target plotted. The analytical model predicted that acceptable magnetic fields would occur at ~0.25 m outboard of the wingtip while the numerical model predicted ~0.35 m.

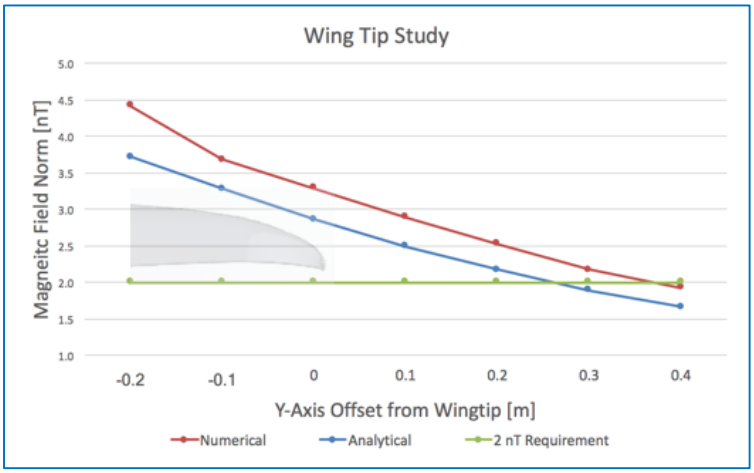

Figure 81: Comparison of Results – Wingtip Chord Wise

Next, the chord wise position of the MAD sensor was explored while the span wise position was varied. The vertical axis displays magnetic fields values while the horizontal axis displays inboard distance (y-axis) from the wingtip. Each curve represents a different chord-wise (forward and aft of mid-chord) linear path inboard from the starboard wingtip (see Figure 82).

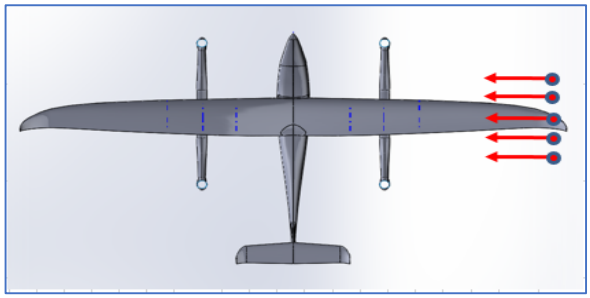

Figure 82: Geometry of Wingtip Chord Wise Sensitivity Analysis

Figure 83 shows the results of a wingtip sensitivity analysis using the analytical model on the starboard wingtip. Evidently, as we move inboard the field values increase. Due to the symmetry configuration of the VTOL motors, the mid-chord line was confirmed to be the line of least magnetic field. Interestingly, the results indicated that near the mid-chord line there was a reduction in magnetic field starting at -0.3 m. This was assumed to be the result of some destructive interference among aileron flight control servo and the VTOL motors.

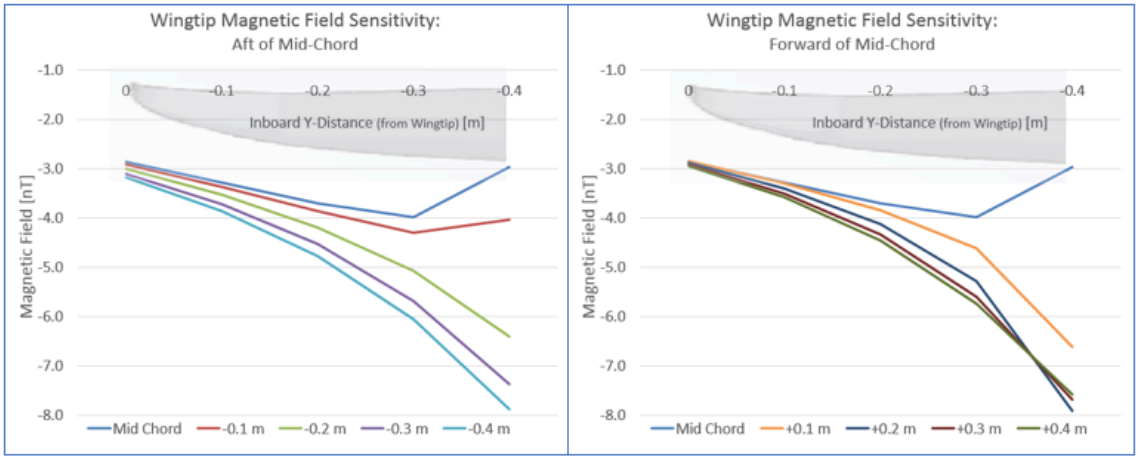

Figure 83: Wingtip Magnetic Field Sensitivity Analysis: Forward and Aft of Mid-Chord

Furthermore, Figure 84 displays a similar analysis but with T&L coefficients. Appendix C contains the value used to produce Figure 84. While the sensitivity of the permanent coefficients generally supports a mid-chord position, the induced coefficients suggest mid-chord is not ideal moving inboard.

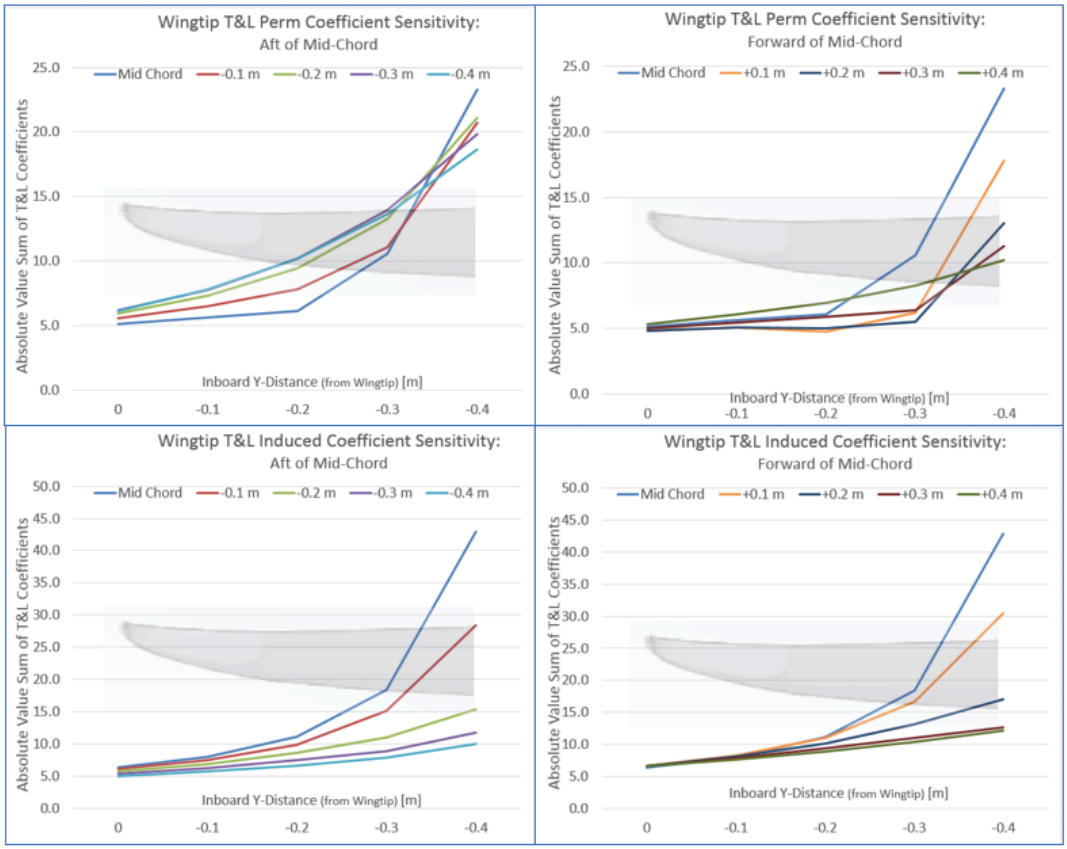

Figure 84: Permanent and Induced T&L Coefficient Absolute Sums

Evidently, being equidistant between the symmetrical VTOL pylons, the mid-chord positions were found to be the line of least magnetic inference.

4.4.4 Recommended MAD Payload Location

To directly compare the wingtip and tail potential MAD payload locations, Figure 85 plots the respective analytical and numerical results for the existing starboard wingtip and varying tail stinger lengths. The analytical tail results suggested that a tail stinger boom of ~0.45 m would be required to equal the starboard wingtip while the numerical results suggested a much larger value of ~1.3 m would be required. In other words, even if a tail stinger boom configuration was selected, the length of stinger boom required to match the field predicted at the starboard wingtip would be between 0.45 m and 1.3 m. A related study examined the aircraft stability implications of such a tail stinger boom and determined that it would be unfeasible with significant forward counter weight required [15].

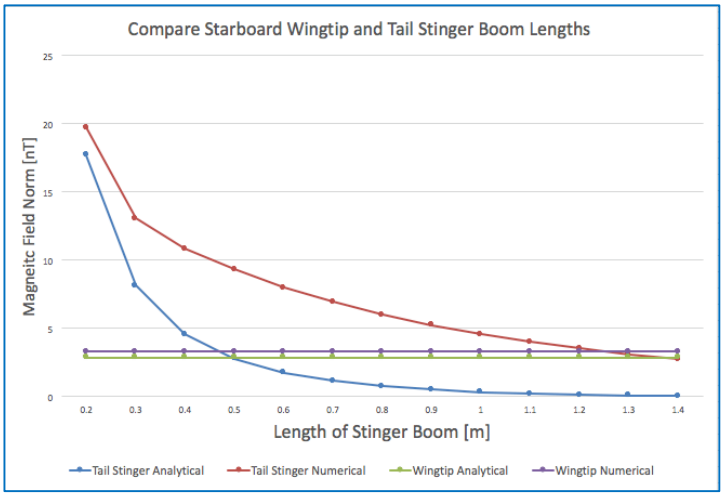

Figure 85: Comparison of Wingtip and Tail Stinger Boom Results

Finally, Figure 86 displays a top view heat map of the of the magnetic flux density norm at z = 0.1 m up to 10 nT. Evidently, the large wingspan of the aircraft allows the wingtips to offer a MAD payload location of least magnetic noise. Reviewing the results for each of the three magnetic models, a wingtip location would have the least magnetic interference.

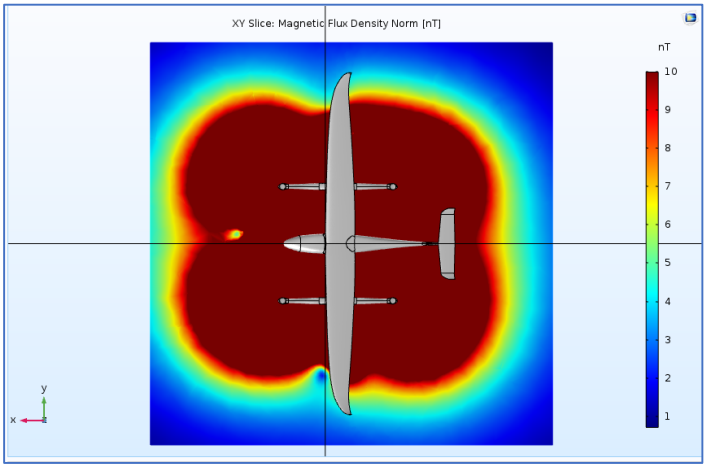

Figure 86: COMSOL – Top View – 10 nT (-2.3 < y < 2.3; -2.6 < x < 2; z = 0.1)

4.4.5 Comparison of Alternate Aircraft Configurations

With the magnetic models established, it becomes possible to explore various aircraft configurations. The two previous geometric sensitivity studies conducted on the tail (4.4.2.1) and wing (4.4.3.1) examined the aircraft in its existing configuration whereas this section modified the aircraft configuration or component positions within. The numerical model was used as it provides the most effective visualizations.

Prior establishing the magnetic models, it was suggested that the tail flight control servos could be translated forward within the fuselage and away from a potential MAD payload positions in the tail. In this configuration, aircraft controllability would be maintained using push rods and bell cranks.

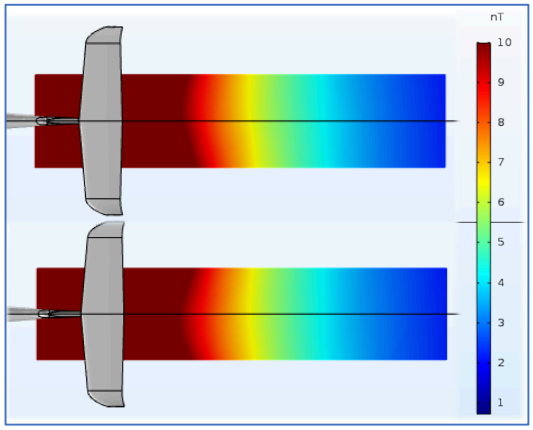

Figure 87: COMSOL – Tail Study – Current Configuration (top) vs Modified Configuration: Rudder Servo (52 cm Forward) Elevator Servos (62 cm Forward & 36 cm Down)

Figure 87 compares the current configuration to a configuration where the aft flight control servos have been moved forward. In this case, the rudder and both elevator servos were moved to the aft avionics bay. Despite the overwhelming contribution of the rudder servo at the tail position (96% in Figure 75), the VTOL effect upholds an unacceptable level of noise for a tail mounted MAD payload.

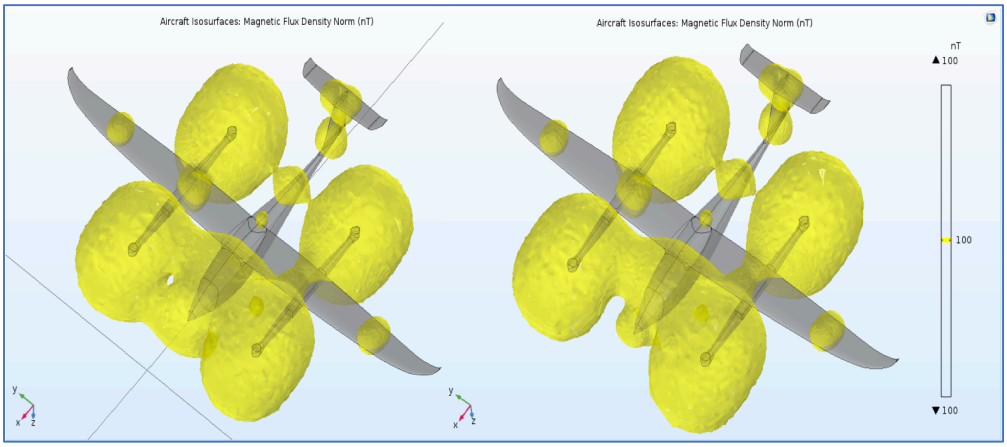

Figure 88: COMSOL – Isosurfaces – 100 nT – Unchanged Configuration (left) vs Modified Configuration: Electric Motor (right).

Figure 88 compares the aircraft forward flight propulsion systems by using 100 nT isosurfaces. As discussed in 3.6.1.1.3, the electric motor has a much smaller magnetic field contribution than the gas combustion engine. The opposite was found by Sterligov and Cherkasov [45], they replaced their electric motor preferring a gas combustion engine. The decision to replace a propulsion system should not be taken lightly as it directly affects aircraft performance. Thus, to sustain the range and endurance of a gas combustion engine, demagnetization should be used to the greatest extent possible.

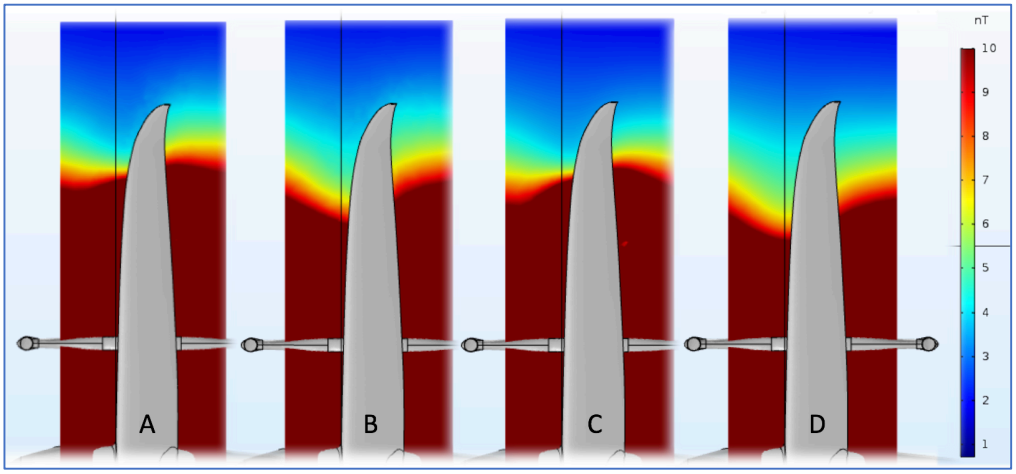

Figure 89: COMSOL – Wing Study – Current Configuration (A) vs Modified Configurations (B-D): Aileron Servos 59 cm Inboard (B); VTOL Motors 10 cm Inboard (C); Servo & VTOL Inboard (D)

Figure 89 provides the reading an interesting comparison of non-trivial wing configurations, translating the aileron servo to a position slightly outboard of the current VTOL pylons and translating the VTOL pylons inboard within stability limits. Figure 89(A) is the current wing configuration while Figure 89(B:D) modify the aileron servos and VTOL pylons inboard. In Figure 89(B), the magnetic flux curves inboard at mid-chord but remains high forward and aft due to the VTOL motors. The opposite effect is seen in Figure 89(C) where the aileron servo sustains high magnetic flux mid-chord. Figure 89(D) combines both effect provide the configuration of lowest magnetic noise at the wingtip.

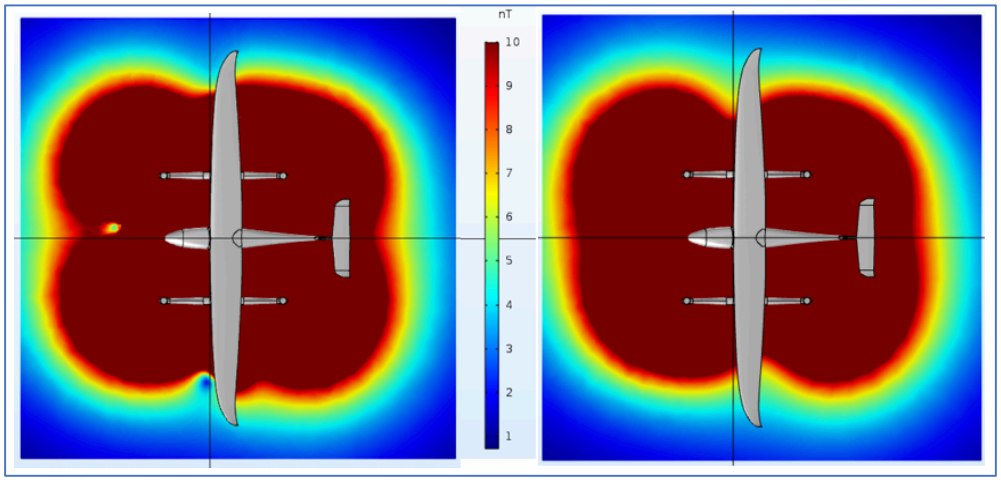

Figure 90: COMSOL – Current Configuration (left) vs Modified Configuration: VTOL Motors 10 cm Inboard + Aileron Servos 59 cm Inboard + Electric Motor (right).

Figure 90(right) combines the results of Figure 88 and Figure 89 into one low signature configuration. In this configuration, the VTOL pylons are translated 10 cm inboard, the aileron servos are translated 59 cm inboard and electric motor is the forward flight substitute. The results of this modified configuration substantiated many of the aircraft design recommendations found in section 5.4.

4.4.6 Comparison of Similar UAVs Involved in Airborne Magnetometry Operations

Two well-studied geomagnetic survey UAVs, the GeoSurv II [27] and the Corvus [17], were used to compare to the Nebula N1 static-field magnetic modelling results, as the magnetic targets accepted by this project were based on the UAV design requirements from these two studies. In [27], in was found that the GeoSurv II would not meet all the design requirements at the time of literature publication. A similar result was found in [17] for the Corvus at the time of literature publication. Furthermore, it was found that design specifications for the Corvus would only be achieved at a distance of 0.5 m outside the planform of the UAV [17]. In the case of the Nebula N1, the current wingspan would not meet the magnetic targets without a wingtip stinger between 0.25 m and 0.35 m of length.

The computed T&L aeromagnetic compensations coefficients agreed with the static-field modelling results regarding MAD payload placement. However, without devoted simulations or test flight data the Nebula N1 T&L results cannot be validated. Thus, literature was used for comparison. Magnetic testing results were compared between the Brican TD100 UAV and the Nebula N1 proposed VTOL variant, both of which resulted in wingtip magnetometer recommendations. Table 45 briefly compares the aircraft details and Table 46 summarizes the T&L modeling results at the time of literature publication.

Table 45: Comparison of Similar UAVs

Parameter	**Brican TD 100** [10]	**Nebula N1** (VTOL)
MTOW [kg]	25	35
Wingspan [m]	5.0	3.9
Wingtip to Aileron Servo [m] [8]	0.65	0.61
Flight Control Servo	Volz DA-05-60	Currawong CBS-15

In this comparison, the Brican TD100 is in a non-VTOL configuration while the Nebula N1 is in a VTOL configuration. To the surprise of the author, the Nebula N1 had lower absolute value of T&L coefficients, both in permanent and induced magnetism, despite the presence of the VTOL motors. While the two UAVs had similar distances between aileron servos and wingtips, but the Brican TD100 was using servos of larger magnetic signature (**Table 56**, Appendix D). Thus, Brican TD100 with larger magnetic signature servos would produce a similar level of permanent magnetic maneuver noise as the Nebula N1 with VTOL motors and servos of lower magnetic signature. Finally, the modeling comparison suggests that Nebula N1 would produce half of the induced magnetic maneuver noise as the Brican TD100.

Table 46: T&L Absolute Value Coefficient Results – Comparison with Brican TD100 UAV

MAD Location	**Absolute Value of T&L Coefficient**										
	PERMANENT				**INDUCED**						
	C_1	**C_2**	**C_3**	**SUM**	**C_4**	**C_5**	**C_6**	**C_7**	**C_8**	**C9**	**SUM**
Nebula N1 (VTOL & Starboard Wingtip)	1.2	2.03	1.89	5.12	1.55E-05	5.05E-05	3.37E-06	2.95E-07	3.56E-05	1.26E-05	6.36
Brican TD100 [9]	3.52	0.14	1.97	5.63	5.82E-05	1.77E-04	4.00E-06	9.40E-06	1.00E-05	4.00E-06	14.16

4.4.7 Discussion on Modelling Results

All magnetic models agree that the wingtip is the MAD payload location of lowest magnetic field. The wingtip comparisons between the numerical and analytical static-field models provided comparable values (within 15%) for the wingtip studies. Conversely, the tail boom studies did not produce comparable values. It was assumed that the proximity of the tail control surface servos to the tail MAD locations lead to approximations in the near-field region.

The numerical model was used for the alternate configurations studies as they provided the most effective visualizations. The existing infrastructure within COMSOL allows for rapid manipulation of qualitative visualizations. As the inner workings of the of COMSOL were largely unknown, it was assumed that different methods of computing magnetic flux density norms were used. It was suggested by Brad Nelson (Aeromagnetic Solutions

Incorporated) [73] that COMSOL could be computing the magnetic flux density norms without consideration for B_E as it is frequently used to model fields larger than B_E, unlike this situation. This could explain the difference in the decay properties between the analytical and numerical results in Figure 85. The analytical values were presented as absolute values to match the all-positive values obtained from COMSOL. The error was further explained by modelling complexities in near-field region and specific implementation of the model within COMSOL.

The T&L aeromagnetic compensation coefficients were computed to understand the effect of maneuver noise. Comparing the magnetic modelling result with similar UAVs, the performance of the UAVs can be inferred in the absence of flight data for validation. Compared to the magnetic modelling results of the Brican TD100, the Nebula N1 offers a VTOL capability while maintaining a similar level of permanent magnetic maneuver noise.

5 Conclusion and Recommendations

5.1 Summary

The magnetic properties of the Nebula N1 UAV (VTOL variant) were characterized and used to predict the MAD payload position of least magnetic noise. This thesis began with a brief synopsis of airborne magnetometry, an outline of UAVs involved in magnetometry operations and the UAV-MAD mission profile. A discussion of relevant magnetic field theory and material science was provided shadowed by a description of common magnetic noise sources, organized per source type. A detailed description of the planning, preparation and procedural considerations was provided, forming an experimental campaign planning guide.

Using magnetometer probes, aircraft magnetic sources were methodically identified for replacement, demagnetization or characterization. Components marked for demagnetization were immediately degaussed while components marked for replacement were noted in the magnetic grooming recommendations. Components for characterization underwent the experimental procedures discussed and their permanent and induced magnetic dipole moment characteristics were determined. The most significant sources of noise were as follows (in order of significance): propulsive units (combustion engine, VTOL motors, etc.), servos (flight control, gas throttle), assorted avionics and assorted ferromagnetic fasteners (to be replaced).

These dipole characteristics were used to build three dimensional magnetic models of the aircraft an analysis the respective effects at various MAD payload positions. MATLAB and COMSOL computational models were used to predict and visualize the magnetic fields around the aircraft. Also, Tolles and Lawson aeromagnetic compensation coefficients were computed to understand the effect of maneuver noise. The geometric sensitivity of MAD payload positions were evaluated for tail and wingtip positions. The most suitable MAD payload position was found to be the wingtip. Finally, some aircraft design and magnetic grooming recommendations were proposed.

5.2 Conclusions

The major contributions from the thesis are as follows:

1. Current State of Nebula N1 UAV (VTOL) Magnetic Signature: Collating the results from the respective component experimental testing and subsequent magnetic models, the proposed VTOL variant of the Nebula N1 does not meet the static-field magnetic signature target. The immediate proximity of the VTOL motors and flight control servos prevent magnetic signature targets from being achieved. That being said, the Nebula N1 remains competitive among similar UAVs involved in magnetometry operations. Sections 5.3 and 5.4 outline a list of recommendations to redesign or reduce the magnetic signature of the Nebula N1 or similar UAVs involved in magnetometry.
2. Component-wise Experimental Procedures: The layout of Chapter 3 provided a planning guide to conduct similar vehicle experimental campaigns. Using magnetometer probes for 'hot spot' identification to determine mitigation strategies is highly recommended. While the partial vehicle tests provided some further insight to unwanted magnetic fields, the lack of source isolation was identified as a weakness. The ten-orientation least squares tests were found to be most effective for 3D modelling purposes.
3. COMSOL Multiphysics for Vehicle Modelling: While the comparisons between the numerical and analytical static-field models provided comparable values for the wingtip studies, the tail boom studies did not produce comparable values. The poor values were assumed to be due to near-field complexities. Qualitatively, the models provided similar magnetic geometries that are representative of the aircraft magnetic signature. The COMSOL AC/DC module provides powerful visualization tools to understand the complex magnetic fields.

5.3 Magnetic Grooming Recommendations

This section highlights the magnetic grooming recommendations that would reduce the magnetic signature of the existing aircraft without major modifications to its configuration.

Table **47** summarizes the magnetic grooming recommendations for a wingtip MAD payload placement on the Nebula N1, sorted by priority and effort. Grooming actions were prioritized per their predicted effect on the aircraft's overall magnetic signature and locally at the MAD sensor. Grooming actions were assigned effort levels as perceived by the CfAR design team.

Complimentary to conventional aeromagnetic compensation techniques, real-time adaptive aeromagnetic compensation increases the compensation effectiveness against transient electrical sources of magnetic noise [38]. The technology uses voltage sensors attached to onboard electric (OBE) systems as inputs to dynamic compensation solutions. Therefore, adaptive aeromagnetic compensation is recommended for the electric motor, servos, autopilot and other high-current avionics. Furthermore, wiring harnesses should be firmly secured (as to reduce vibration) and configured in twisted pairs or closely-spaced parallel pairs to mutually cancel each other's magnetic polarity [17], [27]. Finally, harnesses and cabling should be biasedly routed on the side of fuselage furthest from the MAD payload.

Within the gas combustion engine, the crankshaft position Hall effect sensor was a large source of magnetic interference. As non-magnetic alternatives, it was suggested to replace the Hall effect system with an optical ignition switch or a capacitive sensing solution. Similarly, the flight control servos could be demagnetized and have their internal gears replaced with non-magnetic (i.e. titanium) alternatives [8]. Moreover, passive cancellation could further reduce the significance of the VTOL motors and flight control servos with the addition of small permanent magnets [27].

Basic EMI testing indicated that the aircraft would benefit from EMI shielding in the forward and aft avionics bays. The following EMI shielding methods were suggested: silver-epoxy spray the inner surface of fuselage, copper mesh to contain the avionics bays, integrate ground wires or low inductance straps, copper braid grounding buses or ferrite core chokes, beads or baluns.

Table 47: Summary of Magnetic Grooming Recommendations

Priority	Aircraft Component	Grooming Action	Effort
High	Elect Motors, Servos, Autopilot, High-Current Avionics	Investigate OBE Monitors for Adaptive Aeromagnetic Compensation	High
	VTOL Motors	Investigate Passive Cancellation	Medium
	Servos: Throttle & Flight Control	Investigate Passive Cancellation	Medium
		Replace with Titanium Gears	Low
		Demagnetize Hardware & Housing	Low
	Magnetic Safety Switch (Shunt)	Replace with Alternative	Low
	Gas Motor: Crankshaft Position Sensor	Replace Hall Effect with Alternative	Medium
Medium	Avionics Bays	Apply EMI Shielding Methods	Low
	Wiring Harnesses	Route Harnesses on Opposite Side of Fuselage as MAD Sensor	Medium
		Firmly Secured in Twisted Pairs, Closely-Spaced Parallel Pairs and Shielding	High
		Minimize Cable Lengths	Medium
Low	Assorted Antennas	Replace with Higher Quality Antenna	Low
	Assorted Aircraft Fasteners & Launch Hardware	Replace with Alternatives	Low
	Assorted Large Electrical Connectors	Demagnetize Prior to Install	Low

5.4 Aircraft Design Recommendations for Low Magnetic Signature

This section highlights the aircraft design recommendations that would change the existing aircraft configuration towards a configuration that would have a lower magnetic signature. The most prominent aircraft design recommendation is to integrate the MAD payload into a wingtip configuration in lieu of a tail configuration.

Table **48** summarizes the aircraft design recommendations for a wingtip MAD payload placement, sorted by priority and effort. Design actions were prioritized according to their forecasted effect on the aircraft's overall magnetic signature and locally at the MAD sensor. Design actions were also assigned effort levels by the CfAR design team.

Within the wing, it is further recommended to orient the sensor such that the magnetometer components are centered between the VTOL motors (equidistant, forward and aft). While the magnetic field predicted at the wingtip is more favourable than the tail, wingtip stinger booms or a lengthened wing would further decrease the magnetic noise experienced at the MAD sensor. The reader is cautioned with lengthening the wing as wing flexion, flapping, vibration or relative movement between MAD and VTOL motors could lead to significant noise. Within the CfAR design group a wing optimization study was performed on the Nebula N1 for the UAV-MAD mission profile and found that the optimal length would be 2.3 m semispan, an increase in 0.35 m [15]. To mitigate potential vibration issues, wing and VTOL pylon stiffening is recommended.

The current VTOL configuration could also be modified to decrease magnetic noise. If the VTOL pylons were lengthened or moved inboard, their overwhelming effect would be decreased in the wingtip configuration, similar to Figure 89. Despite being relatively low signature compared to other UAV flight control servos, a similar recommendation is provided for flight control servos within the wing whereby aircraft controllability could be maintained using push rods and bell cranks. Furthermore, the configuration of VTOL motors and flight control servos could also be optimized using the methodology found in [27]. Finally, a non-magnetic propeller locking system must be designed to ensure the VTOL motors do not become transient sources of noise, with wind-milling propellers in forward flight.

Table 48: Summary of Aircraft Design Recommendations for Low Magnetic Signature

Priority	Aircraft Component	Design Action	Effort
High	MAD Payload	Wingtip Placement	Medium
		Magnetometers Components Centered Between Forward & Aft VTOL Motors	Medium
	Wings	Design Stingers or Lengthen Wings	High
		Stiffen to Reduce Relative Motion & Vibration	High
	VTOL Pylons		Medium
		Translate VTOL Pylons Inboard	Medium
		Lengthen VTOL Pylons	Medium
	VTOL Motors	Optimize Orientations to Min Noise	High
		Design Non-Magnetic Propeller Lock Mechanism When Inactive	Medium
Medium	Servos: Throttle & Flight Control	Translate Wing Servos Inboard, Notably Ailerons	Low
		Optimize Orientations to Min Noise	Medium
	Forward Flight Propulsion	Use Electric Motor Vice Gas Combustion	Medium
	Aircraft Structure & MAD Pods (30 cm within MAD) [27]	Composite Material	Low
		Non-Conductive Material	Low

5.5 Future Work

While it is acknowledged that the magnetic assessments of this vehicle are not complete, the following summarizes recommendations for future work:

1. Study Wingtip Flexion, Translations and Vibrations. This type of study would be focused on the relative displacement between the magnetometer and major sources of noise, notably the VTOL motors, while in the flight regime experienced during a magnetic search. Using aeroelastic models of the aircraft, an estimate of the wingtip displacement could be obtained. Alternatively, displacement data could be obtained using wingtip-mounted accelerometers or inertial-GPS units correlated with the aircraft autopilot during (simulated payload) test flights. Similarly, the relative displacement of the inactive VTOL motors during flight could be obtained using these methods. With the vertical displacements known, vertical magnetic gradients can be evaluated at the wingtips similar to [17].
2. Implementation of Magnetic Grooming Strategies**.** As outlined in

3. Table **47** of section 5.3, there are a series of magnetic grooming actions that could be taken to reduce the magnetic signature of the vehicle. Considerable reduction in static magnetic signature could be achieved though passive cancellation strategies [27] or reductions in transient noise using OBE monitors and adaptive compensation [38].
4. Aircraft Configuration Optimization Studies. On top of the aircraft design recommendations presented in section 5.4 (

5. Table **48**) and Nebula N1 wing study [15], a formal optimization on VTOL UAV configurations could be completed for MAD operations. While the Nebula N1 will most likely meet project demonstration objectives, it may not be the best configuration for the UAV-MAD mission profile. Evidently, the aircraft configuration has a strong influence on the levels of magnetic interference, and consequently the detection range of the magnetometer payload during a magnetic search.
6. Maneuver Noise Assessments. While T&L aeromagnetic compensation coefficients were computed, they were not applied to any type of maneuver noise compensation. Generally, there are three ways to assess maneuver noise: ground figure of merit (FOM) tests, simulated FOMs and flight test FOM maneuvers. In [35], [60], the maneuver noise of an autonomous underwater vehicle (AUV) was tested using a motion table. Alternatively in [74], a ground-based FOM procedure was developed for aircraft. FOM maneuvers could also be simulated using artificial vector magnetometer inputs. Using the directional cosines between the aircraft frame of reference and Earth's magnetic field found in [40], simulated vector magnetometer inputs can be produced using sample flight data. Thus, a simulated FOM maneuver could be extrapolated using the computed T&L coefficients. In [42], [50], the standardized aircraft maneuvers and acceptable FOM standards are published for conventional maneuvers. Alternative and less arduous FOM maneuvers are suggested in [32], [38].

Bibliography

[1] W. Campbell, *Introduction to Geomagnetic Fields*, Second Edi. New York: Cambridge University Publishing, 2003.

[2] S. V Cherkasov, B. Sterligov, and L. A. Zolotaya, "On the Use of Unmanned Aerial Vehicles for High-Precision Measurements of the Earth's Magnetic Field," *Orig. Russ. Text ©*, vol. 71, no. 3, pp. 145–8752, 2016.

[3] C. Reeves, *Aeromagnetic Surveys. Principles, Practice & Interpretation*. 2006.

[4] R. Hill, *Anti-Submarine Warfare*, Second Edi. Annapolis: Naval Institute Press, 1989.

[5] "Brazilian P-3 Orion Maritime Patrol Aircraft." [Online]. Available: https://www.defenseindustrydaily.com. [Accessed: 15-Nov-2017].

[6] "USN SH-2G Super Seasprite Helicopter." [Online]. Available: https://www.naval-technology.com. [Accessed: 15-Nov-2017].

[7] K. Osborn, "Navy Arms, Upgrades Fire Scout UAS," *DefenseTech*. .

[8] B. J. Nelson, "Summary of Ground Magnetic Tests of TD100 UAV at Brican Flight Systems," Brampton, 2015.

[9] B. J. Nelson, "Summary of Flight Test at UVic CfAR," Victoria, 2015.

[10] "Brian TD100 UAV." [Online]. Available: https://www.bricanflightsystems.com. [Accessed: 15-Nov-2017].

[11] "Carleton-Sander GeoSurv II UAV." [Online]. Available: 2014uav.mae.carleton.ca/fleet. [Accessed: 15-Nov-2017].

[12] K. Parvar, "Development and Evaluation of Unmanned Aerial Vehicle (UAV) Magnetometry Systems," Queen's University, 2016.

[13] M. Wells, "Attenuating Magnetic Interference in a UAV System," Carleton University, 2008.

[14] J. Richards, "Nebula Unmanned Aerial Vehicle Systems." [Online]. Available: https://www.nebula.aero/. [Accessed: 15-Apr-2018].

[15] G. Gamerio, "Wing Optimization for MAD Operations," Instituto Superior Ténico, 2018.

[16] S. Breiner, "Application Manual for Portable Magnetometers," San Jose, California, 1999.

[17] L. Tuck, C. Samson, J. Laliberté, M. Wells, and F. Belanger, "Magnetic Interference Testing Method for an Electric Fixed-Wing Unmanned Aircraft System (UAS)," *J. Unmanned Veh. Syst.*, 2018.

[18] CAE, "Magnetic Anomaly Detection Extended Role (MAD-XR)," *Product Datasheets*, 2018. [Online]. Available: https://www.cae.com/media/media-center/documents/datasheet.MAD-XR.pdf. [Accessed: 15-Apr-2018].

[19] S. Tumanski, *Handbook of Magnetic Measurements*. Boca Raton: CRC Press, Taylor & Francis Group, LLC, 2011.

[20] F. T. Ulaby and U. Ravaioli, *Fundamentals of Applied Electromagnetics*, Seventh Ed. Upper Saddle River: Pearson Education, Inc., 2015.

[21] D. Fleisch, *A Student's Guide to Maxwell's Equations*. New York: Cambirdge University Press, 2009.

[22] K. M. Lee and H. Son, "Distributed multipole model for design of permanent-magnet-based actuators," *IEEE Trans. Magn.*, vol. 43, no. 10, pp. 3904–3913,

2007.
[23] D. Tilley, “Characterizing Magnetic Noise of AUV For Use in Towed Magnetometer Study of Internal Waves,” Florida Atlantic University, 2012.
[24] J. M. D. Coey, *Magnetism and Magnetic Materials*, vol. 46, no. 1–2. Cambridge University Publishing, 2010.
[25] T. Wildi, *Electrical Machines, Drives, and Power Systems*, Third Edit. Upper Saddle River: Prentice-Hall Inc, 1997.
[26] R. Morjan and S. Prasalovich, “EM4: Magnetic Hysteresis,” 2003.
[27] R. Forrester, “Magnetic Signature Control Strategies for an Unmanned Aircraft System,” Carleton University, 2011.
[28] S. Breiner, “Magnetic Search in the Marine Environment,” San Jose, California.
[29] J. M. D. Coey, “Magnetic Materials,” *J. Alloys Compd.*, vol. 326, no. 1–2, pp. 2–6, 2001.
[30] J. J. Holmes, *Modeling a Ship’s Ferromagnetic Signatures*, vol. 2, no. 1. 2007.
[31] L. E. Zaffanella, T. P. Sullivan, and I. Visintainer, “Magnetic field characterization of electrical appliances as point sources through in situ measurements,” *IEEE Trans. Power Deliv.*, vol. 12, no. 1, pp. 443–449, 1997.
[32] B. J. Nelson, “Time-Domain Tolles & Lawson Aircraft Compensation,” in *Presentation by Aeromangetic Solutions Inc. to NRC Flight Research Lab*, 2017.
[33] L. Tuck, C. Samson, J. Laliberté, M. Wells, F. Bélanger, and L. Sander, “Measuring the Magnetic Signature of a Small Electrically-powered Fixed-wing Unmanned Aircraft System for Mineral Exploration,” in *PDAC 2017*, 2017.
[34] R. Forrester, M. S. Huq, M. Ahmadi, and P. Straznicky, “Magnetic Signature Attenuation of an Unmanned Aircraft System for Aeromagnetic Survey,” *IEEE/ASME Trans. Mechatronics*, vol. 19, no. 4, pp. 1436–1446, 2014.
[35] G. I. Allen, J. Purpura, and D. Overway, “Measurement of magnetic noise characteristics on select AUVS with some potential mitigation techniques,” *Ocean. 2002 Mts/IEEE Conf. Exhib. Vols 1-4, Conf. Proc.*, pp. 978–984, 2002.
[36] M. Wynn and J. Bono, “Magnetic sensor operation onboard an AUV: magnetic noise issues and a linear systems approach to mitigation,” *Ocean. ’02 Mts/Ieee*, vol. 2, 2002.
[37] A. Hay, “Instrumentation and Application of Unmanned Ground Vehicles for Magnetic Surveying,” Carleton University, 2017.
[38] G. Noriega and A. Marszalkowski, “Adaptive Techniques and Other Recent Developments in Aeromagnetic Compensation,” *First Break*, vol. 35, no. 9, pp. 31–38, 2017.
[39] J. J. Holmes, *Reduction of a Ship’s Magnetic Field Signatures*, vol. 3, no. 1. 2008.
[40] P. Leliak, “Identification and Evaluation of Magnetic- Field Sources of Magnetic Airborne Detector Equipped Aircraft,” *IRE Trans. Aerosp. Navig. Electron.*, pp. 95–105, 1961.
[41] B. W. Leach, “Automatic Aeromagnetic Compensation,” *Lab. Tech. Report, Natl. Res. Counc. Canada*, vol. LTR-FR-69, p. 133, 1979.
[42] D. J. Teskey, “Guide to Aeromagnetic Specifications and Contracts,” Energy, Mines and Resources Canada, 1991.
[43] G. Schultz, R. Mhaskar, M. Prouty, and J. Miller, “Integration of Micro-Fabricated Atomic Magnetometers on Military Systems,” vol. 982318, no. May 2016, p.

982318, 2016.
[44] B. J. Nelson, “Aeromagnetic Noise During Low-Altitude Flights over the Scotian Shelf,” no. May, 2002.
[45] B. Sterligov and S. Cherkasov, “Reducing magnetic noise of an unmanned aerial vehicle for high-quality magnetic surveys,” *Int. J. Geophys.*, vol. 2016, 2016.
[46] B. J. Nelson, “Detecting Wave-Induced Magnetic Signals with an Airborne Magnetometer,” 2002.
[47] Z. Daya, D. Hutt, and T. Richards, “Maritime electromagnetism and DRDC Signature Management research,” 2005.
[48] J. Jankowski and C. Sucksdorff, *Guide for Magnetic Measurements and Observatory Practice*. 1996.
[49] G. Noriega, “Aeromagnetic Compensation in Gradiometry—Performance, Model Stability and Robustness in Aeromagnetic Compensation,” *First Break*, vol. 31, no. 3, pp. 73–79, 2015.
[50] M. Coyle, R. Dumont, P. Keating, F. Kiss, and W. Miles, “Geological Survey of Canada aeromagnetic surveys: design, quality assurance, and data dissemination,” 2014.
[51] C. Samson, P. Straznicky, J. Laliberté, R. Caron, S. Ferguson, and R. Archer, “Designing and Building an Unmanned Aircraft System for Aeromagnetic Surveying,” *SEG Tech. Progr. Expand. Abstr. 2010*, no. April 2015, pp. 1167–1171, 2010.
[52] B. J. Nelson, “ASI-2018-1: Summary of Nebula Magnetic Grooming,” Gloucester, Ontario, 2018.
[53] T. Roy, “Spacecraft magnetic field modeling,” *IEEE Trans. Magn.*, vol. MAG-13, no. 1, pp. 914–919, 1977.
[54] W. L. Eichhorn, “Magnetic Dipole Moment Determination by Near-Field Analysis,” 1972.
[55] K. Mehlem, “Multiple Magnetic Dipole Modeling and Field Prediction of Satellites,” *IEEE Trans. Magn.*, vol. 14, no. 5, pp. 1064–1071, 1978.
[56] K. Mehlem, D. Pastrone, and L. Casalino, “Optimal Magnetic Cleanliness Modeling (Ch 13 from: Modeling and Optimization in Space Engineering),” in *Modeling and Optimization in Space Engineering*, 2013, pp. 343–362.
[57] B. Armstrong *et al.*, “Field Measurement of Surface Ship Magnetic Signature Using Multiple AUVs,” *Ocean. 2009*, pp. 1–9, 2009.
[58] D. Tilley, M. Dhanak, E. An, and K. Von Ellenrieder, “Characterizing magnetic sensors and magnetic noise of AUVs,” *Ocean. 2012 MTS/IEEE Harnessing Power Ocean*, 2012.
[59] G. I. Allen, R. Matthews, and M. Wynn, “Mitigation of platform generated magnetic noise impressed on a magnetic sensor mounted in an autonomous underwater vehicle,” *Ocean. Conf. Rec.*, vol. 1, pp. 63–71, 2001.
[60] J. T. Bono, D. J. Overway, and W. M. Wynn, “Magnetic sensor operation onboard a UUV: Magnetic noise investigation using a total-field gradiometer,” *Ocean. 2003 Celebr. Past... Teaming Towar. Futur.*, vol. 4, pp. 2018–2022, 2003.
[61] R. Versteeg, M. McKay, M. Anderson, R. Johnson, B. Selfridge, and J. Bennett, “Feasibility Study for an Autonomous UAV – Magnetometer System,” 2007.
[62] J. B. Stoll, “Unmanned Aircraft Systems For Rapid Near Surface Geophyscial

Measurements," 2013.
[63] R. Caron, "Aeromagnetic Surveying Using a Simulated UAS," Carleton University, 2011.
[64] R. Caron, C. Samson, P. Straznicky, S. Ferguson, R. Archer, and L. Sander, "Magnetic and magneto-gradiometric surveying using a simulated unmanned aircraft system," *SEG Tech. Progr. Expand. Abstr. 2011*, no. April 2015, pp. 861–865, 2011.
[65] R. Caron, C. Samson, P. Straznicky, S. Ferguson, and L. Sander, "Aeromagnetic Surveying using a Simulated UAS," *Geophys. Prospect.*, vol. 62, no. 2, pp. 352–363, 2013.
[66] M. Cunningham, "Aeromagnetic Surveying with Unmanned Aircraft Systems," 2016.
[67] S. Tumanski, "Modern Magnetic Field Sensors – A Review," *PRZEGLĄD ELEKTROTECHNICZNY*, no. 10, pp. 1–12, 2013.
[68] N. R. Canada, "Victoria (VIC) Magnetic Observatory," *Geomagnetism Canada*. [Online]. Available: http://www.geomag.nrcan.gc.ca/obs/vic-en.php. [Accessed: 15-Apr-2018].
[69] N. R. Canada, "Magnetic Field Calculator," *IGRF-12*. [Online]. Available: http://geomag.nrcan.gc.ca/calc/mfcal-en.php. [Accessed: 15-Apr-2018].
[70] B. J. Nelson, "ASI-2018-6: Summary of Nebula Magnetic Grooming," Gloucester, Ontario, 2018.
[71] COMSOL Mulitiphysics, "AC/DC Module User's Guide," vol. 5.2, 2015.
[72] COMSOL Multiphysics Online Application Gallery, "Tutorial: Magnetic Signature of a Submarine."
[73] B. J. Nelson, "Personal Email Correspondence." .
[74] B. J. Nelson, "Predicting In-Flight MAD Noise From Ground Measurements," 2002.

Appendix A – Summary of Magnetic Dipole Moment Results

The following table summarizes the magnetic parameter results of from the 10-Orientation 3D Source Characterization discussed in 3.6.1.1. This table includes all the aircraft components tested.

Table 49: Summary of Magnetic Dipole Moment Results

Aircraft Source		Permanent Magnetic Effects			Induced Magnetic Effects		
		M_{px}	M_{py}	M_{pz}	k_x	k_y	k_z
Propulsion	**Port Forward VTOL Engine**	5.14	1.02	3.30	2.00E-06	-2.30E-05	-3.00E-06
	Port Aft VTOL Engine	5.14	1.02	3.30	2.00E-06	-2.30E-05	-3.00E-06
	Starboard Forward VTOL Engine	5.14	1.02	3.30	2.00E-06	-2.30E-05	-3.00E-06
	Starboard Aft VTOL Engine	5.14	1.02	3.30	2.00E-06	-2.30E-05	-3.00E-06
	Gas Engine (Forward Flight)	-2.27	-1.77	-6.90	1.07E-04	8.10E-05	1.09E-04
	Electric Engine (Forward Flight)	-0.17	-0.05	0.06	-1.65E-06	-9.89E-08	2.86E-06
	Gas Engine Throttle Servo	1.24E-02	1.52E-02	1.26E-01	4.57E-07	3.32E-07	1.12E-06
Flight Controls	**Port Flap Flight Control Servo**	1.26E-01	1.52E-02	-1.24E-02	1.12E-06	3.32E-07	4.57E-07
	Port Aileron Flight Control Servo	1.26E-01	1.52E-02	-1.24E-02	1.12E-06	3.32E-07	4.57E-07
	Starboard Flap Flight Control Servo	-1.26E-01	1.52E-02	1.24E-02	1.12E-06	3.32E-07	4.57E-07
	Starboard Aileron Flight Control Servo	-1.26E-01	1.52E-02	1.24E-02	1.12E-06	3.32E-07	4.57E-07
	Port Elevator Flight Control Servo	1.26E-01	1.52E-02	-1.24E-02	1.12E-06	3.32E-07	4.57E-07
	Starboard Elevator Flight Control Servo	-1.26E-01	1.52E-02	1.24E-02	1.12E-06	3.32E-07	4.57E-07
	Rudder Flight Control Servo	-1.24E-02	-1.52E-02	1.26E-01	4.57E-07	3.32E-07	1.12E-06
Flight Pack Batteries	**Battery Flight Pack – FWD (#1)**	-2.61E-02	1.00E-04	8.00E-04	5.00E-07	4.00E-07	1.00E-07
	Battery Flight Pack – AFT (#2)	-1.47E-01	5.13E-02	-1.27E-01	5.30E-06	1.80E-06	3.00E-07
Specific Avionics	**Silvis FM Radio (FWD Avionics Bay)**	-8.21E-02	-1.30E-01	-1.90E-01		2.00E-07	9.00E-07
	Video Encoder (FWD Avionics Bay)	1.92E-02	2.47E-02	7.50E-03	9.00E-07	1.60E-06	8.00E-07

	900 MHz Antenna (Aft Tail)	0	0	0	0	0	0
	2.4 GHz Whip Antenna #2 (Aft Avionics Bay)	0	0	0	0	0	0
	2.4 GHz Whip Antenna #1 (Aft Avionics Bay)	0	0	0	0	0	0
	DGPS Electronics (Aft Avionics Bay)	5.09E-02	6.00E-02	7.66E-02	2.60E-06	2.40E-06	1.20E-06
	DGPS Antenna (Aft Avionics Bay)	-1.73E-02	-1.40E-03	6.20E-03	6.00E-07	1.20E-06	1.00E-07
	Autopilot GPS Antenna (Aft Avionics Bay)	5.09E-02	6.00E-02	7.66E-02	2.60E-06	2.40E-06	1.20E-06
	Magnetic Safety Switch (Port)	0	3.49E+00	0	0	2.80E-05	0
Electrical	**Connector: Aft Switchboard to Saddle, Wing Attach**	0	0	-0.01	0	0	0
	Connector: DGPS to Aft Switchboard	1.88E-02	0	0	0	0	0

Appendix B – Single Magnetic Dipole Simulation

Prior to utilizing the COMSOL for modeling the complex magnetic signature of the Nebula UAV, a series of simple magnetic dipole cases were used to establish confidence in the computational results. A single point magnetic dipole was simulated and the results were compared to analytical results. The complexity of the aircraft's magnetic signature along with the inability to experimentally measure the aircraft's magnetic field pre-production, leads to this outside-the-box approach. The results of this study were used to tune and improve confidence in the complex aircraft magnetic signature model. In all cases, a point magnetic dipole of 100 Am^2 (10 000 nTm^3) was placed at (0,0,0) and the magnetic flux density norm was obtained at various distances along the x, y and z-axes. In all single dipole magnetic dipole simulations, the absolute value of the TF calculations are compared to the COMSOL results. Figure 91 displays a sample 2D planar cut of the COMSOL results.

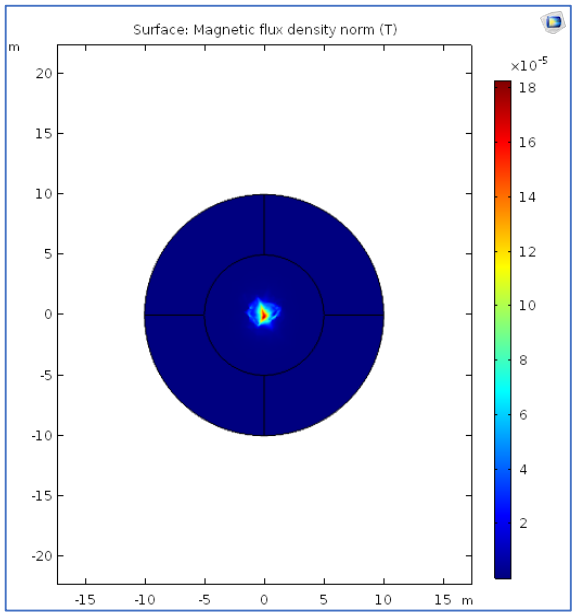

Figure 91: 2D Planar Cut of Single Dipole Simulation

Three dipole trials were conducted using $M = M_{xx}$, $M = M_{yy}$ and $M = M_{zz}$ using COMSOL. For each dipole trial, the analytical results were compared to the COMSOL results in in the x, y and z-axes. Figure 92, Figure 93 and Figure 94 display the single magnetic dipole comparisons in x, y and z-axes for $M = M_{zz}$, M_{yy} and M_{xx} respectively.

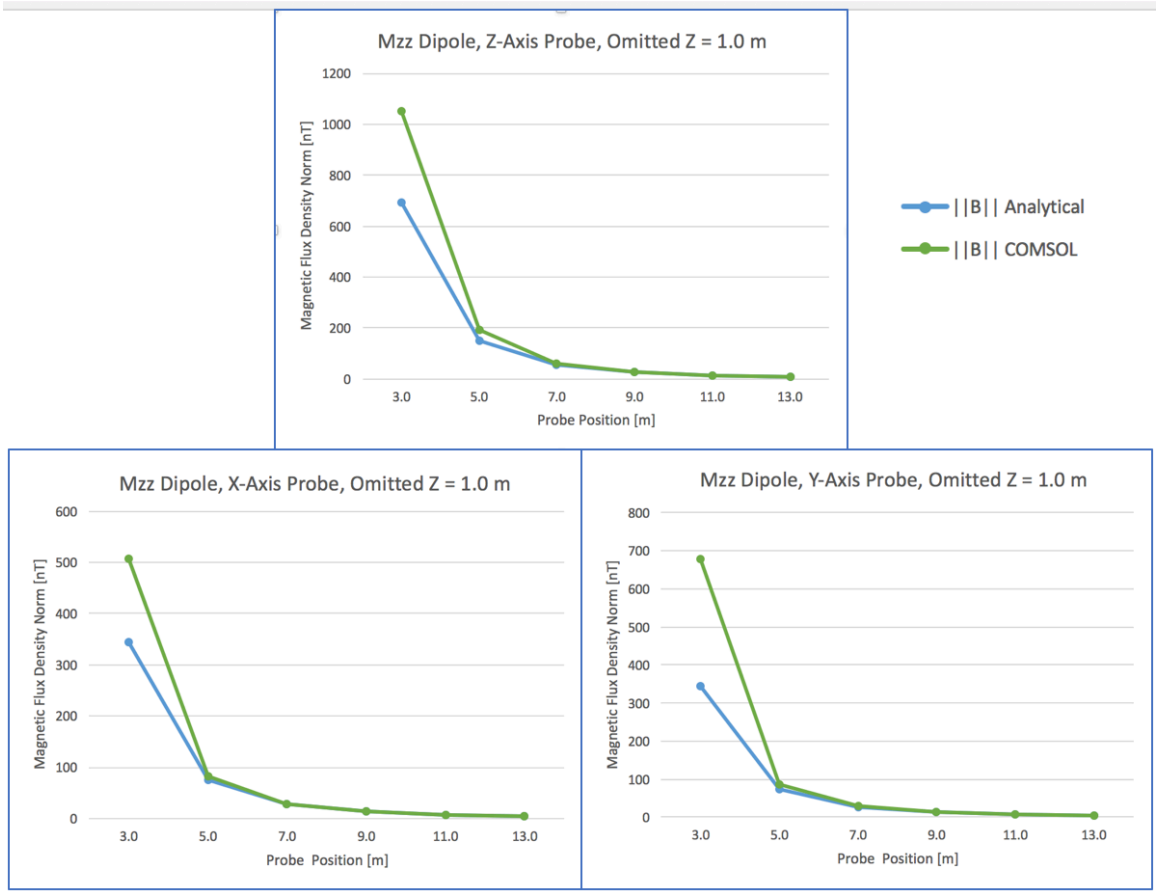

Figure 92: Single Magnetic Dipole $M = M_{zz}$ Comparison in x, y and z-axes

Best of all the cases studies, Figure 92 and

Table **50** show an excellent fit (less than 10% error) between analytical and computational results into the far-field region (assumed to be 7 m). The accuracy of the fit decreases closer to the dipole, as expected, with the complexity of the near-field region. Note that if the absolute value of TF were not taken, the x-axis and y-axis analytical curves would be negative, since these axes are perpendicular (zero $M \cdot R$ dot product).

Table 50: Single Magnetic Dipole $M = M_{zz}$ Comparison in x, y and z-axes

	Z-Axis			Y-Axis			X-Axis		
Length [m]	**Analytical [nT]**	**Numerical [nT]**	**Error**	**Analytical [nT]**	**Numerical [nT]**	**Error**	**Analytical [nT]**	**Numerical [nT]**	**Error**
1.0	18653.14	14875.00	25.4%	9326.57	8266.90	12.8%	9326.57	15700.00	40.6%
3.0	690.86	1051.80	34.3%	345.43	677.76	49.0%	345.43	506.09	31.7%
5.0	149.23	190.15	21.5%	74.61	85.36	12.6%	74.61	81.19	8.1%
7.0	54.38	60.20	9.7%	27.19	29.62	8.2%	27.19	27.69	1.8%
9.0	25.59	26.71	4.2%	12.79	14.03	8.8%	12.79	13.91	8.0%
11.0	14.01	14.83	5.5%	7.01	7.63	8.1%	7.01	7.73	9.3%
13.0	8.49	9.02	5.9%	4.25	4.55	6.7%	4.25	4.58	7.4%

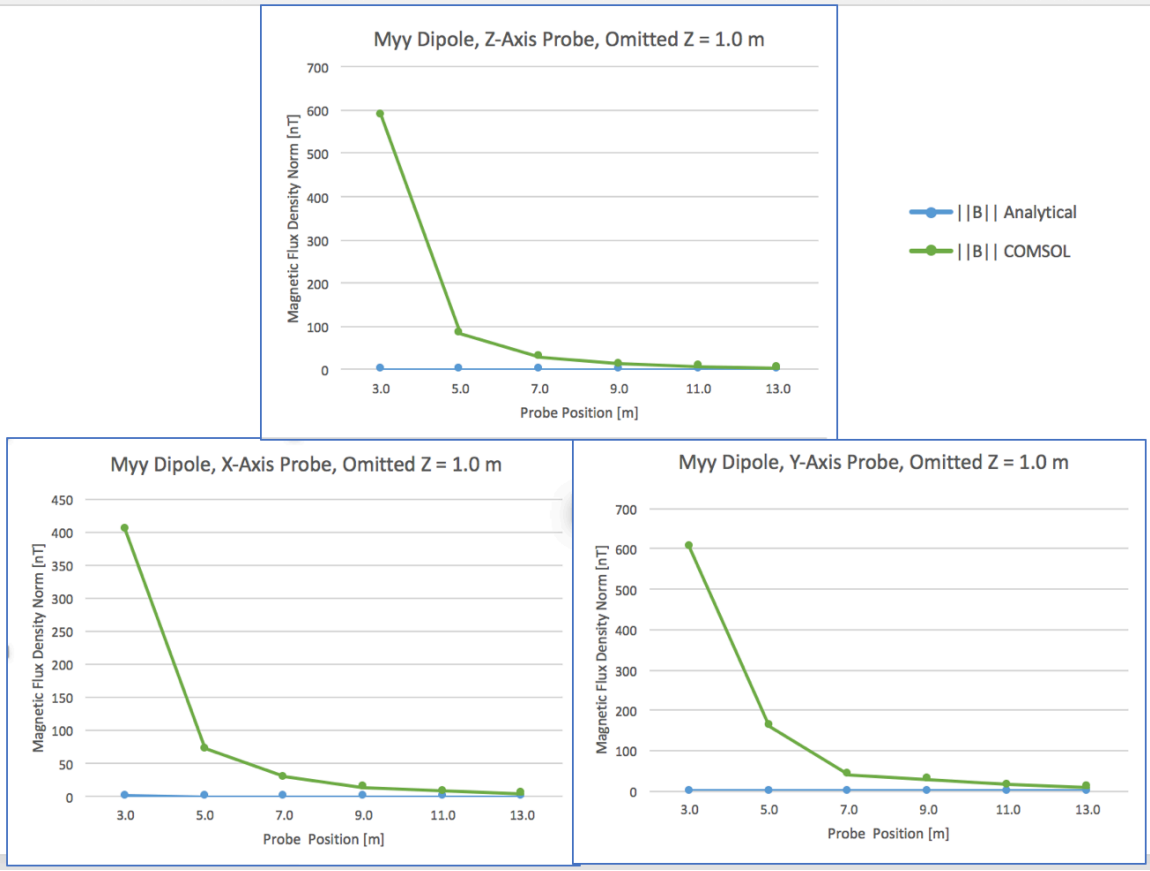

Figure 93: Single Magnetic Dipole $M = M_{yy}$ Comparison in x, y and z-axes

Table 51: Single Magnetic Dipole $M = M_{yy}$ Comparison in x, y and z-axes

	Z-Axis			Y-Axis			X-Axis		
Length [m]	**Analytical [nT]**	**Numerical [nT]**	**Error**	**Analytical [nT]**	**Numerical [nT]**	**Error**	**Analytical [nT]**	**Numerical [nT]**	**Error**
1.0	6.89	9584.20	99.9%	13.78	14244.00	99.9%	6.89	8011.20	99.9%
3.0	0.26	588.86	100.0%	0.51	604.24	99.9%	0.26	403.40	99.9%
5.0	0.06	83.73	99.9%	0.11	160.83	99.9%	0.06	72.03	99.9%
7.0	0.02	29.59	99.9%	0.04	40.14	99.9%	0.02	28.82	99.9%
9.0	0.01	13.51	99.9%	0.02	28.13	99.9%	0.01	13.40	99.9%
11.0	0.01	7.58	99.9%	0.01	15.00	99.9%	0.01	7.67	99.9%
13.0	0.00	4.53	99.9%	0.01	9.15	99.9%	0.00	4.63	99.9%

Figure 93 and

Table **51** do not show any type of fit between analytical and computational in all regions. The flatness of the analytical results is due to the small magnitude of Earth's magnitude field in y-axis, B_{Ey}, decreasing the value of $M \cdot B_E$. Suggesting that the values for Earth's geomagnetic filed were skewing data.

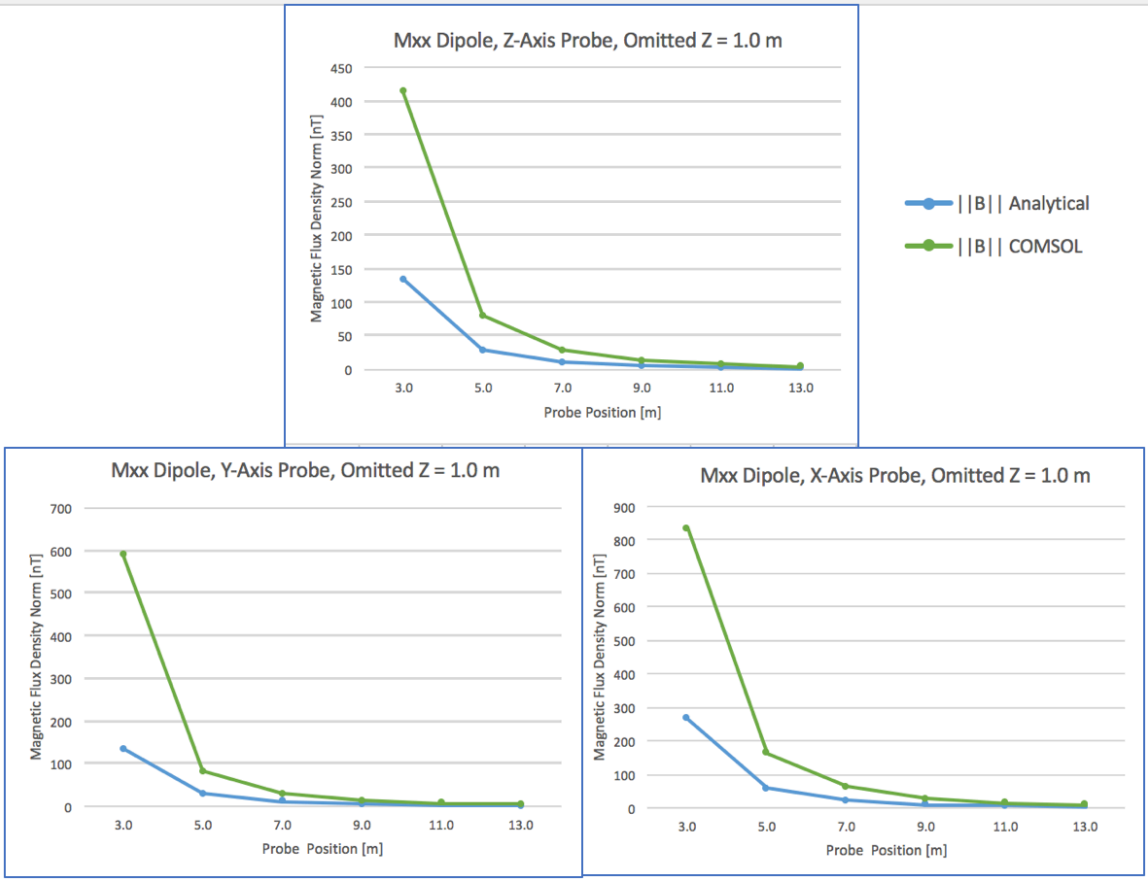

Figure 94: Single Magnetic Dipole $M = M_{xx}$ Comparison in x, y and z-axes

Figure 94 and Table 52 indicate that the computational solution over-estimated the result (60% error) as compared to the analytical solution in all regions. Similar to Figure 92, perpendicular axes created a zero $M \cdot R$ dot product, but in this case it occurred in the y-axis and z-axis. As the results varied so wildly, it was assumed that the mesh implementation within COMSOL was flawed.

Table 52: Single Magnetic Dipole $M = M_{xx}$ Comparison in x, y and z-axes

	Z-Axis			Y-Axis			X-Axis		
Length [m]	**Analytical [nT]**	**Numerical [nT]**	**Error**	**Analytical [nT]**	**Numerical [nT]**	**Error**	**Analytical [nT]**	**Numerical [nT]**	**Error**
1.0	3607.64	9957.50	63.8%	3607.64	4252.00	15.2%	7215.28	22622.00	68.1%
3.0	133.62	413.34	67.7%	133.62	589.36	77.3%	267.23	835.49	68.0%
5.0	28.86	79.77	63.8%	28.86	81.63	64.6%	57.72	162.45	64.5%

7.0	10.52	29.09	63.8%	10.52	29.04	63.8%	21.04	62.66	66.4%
9.0	4.95	13.61	63.6%	4.95	13.78	64.1%	9.90	26.71	62.9%
11.0	2.71	7.36	63.2%	2.71	7.46	63.7%	5.42	15.08	64.1%
13.0	1.64	4.55	63.9%	1.64	4.54	63.8%	3.28	9.25	64.5%

Appendix C – T&L Wing Sensitivity Results

The following tables summarizes the T&L aeromagnetic compensation coefficient values used to produce Figure 84 as part of the wing sensitivity analysis conducted in section 4.4.3.1. The first table features the values forward of the mid-chord and the second table features values aft of the mid-chord.

Table 53: Results of T&L Wing Sensitivity Analysis: Forward of Mid-Chord

MAD Location [m]		**Absolute Value of T&L Coefficient**										
		PERMANENT				**INDUCED**						
Fwd X	**Inboard Y**	**C1**	**C2**	**C3**	**SUM**	**C4**	**C5**	**C6**	**C7**	**C8**	**C9**	**SUM**
Mid Chord [0.0]	Wingtip [0.0]	1.20	2.03	1.89	5.12	1.55E-05	5.05E-05	3.37E-06	2.95E-07	3.56E-05	1.26E-05	6.36
	-0.1	0.84	2.46	2.32	5.61	2.00E-05	6.41E-05	4.27E-06	1.13E-06	4.37E-05	1.54E-05	8.02
	-0.2	0.13	3.10	2.87	6.10	2.86E-05	8.94E-05	5.74E-06	5.02E-06	5.74E-05	2.00E-05	11.13
	-0.3	2.74	4.25	3.58	10.58	4.97E-05	1.50E-04	9.44E-06	1.62E-05	8.71E-05	2.92E-05	18.42
	-0.4	11.77	7.31	4.23	23.31	1.24E-04	3.51E-04	2.97E-05	5.49E-05	1.81E-04	5.37E-05	42.88
+0.1	Wingtip [0.0]	1.16	1.82	1.87	4.85	1.63E-05	5.14E-05	2.67E-06	1.15E-06	3.77E-05	1.31E-05	6.61
	-0.1	0.85	1.90	2.32	5.07	2.03E-05	6.43E-05	3.56E-06	2.67E-06	4.59E-05	1.60E-05	8.25
	-0.2	0.09	1.71	2.96	4.76	2.70E-05	8.67E-05	5.34E-06	6.13E-06	5.88E-05	2.04E-05	11.04
	-0.3	1.65	0.48	4.06	6.19	3.91E-05	1.34E-04	1.06E-05	1.42E-05	8.29E-05	2.87E-05	16.69

	-0.4	5.28	5.41	7.08	17.76	5.73E-05	2.53E-04	3.67E-05	3.27E-05	1.38E-04	4.76E-05	30.50
+0.2	Wingtip [0.0]	1.27	1.71	1.85	4.83	1.62E-05	5.12E-05	2.22E-06	1.82E-06	3.90E-05	1.34E-05	6.69
	-0.1	1.18	1.59	2.30	5.07	1.91E-05	6.22E-05	3.28E-06	2.80E-06	4.67E-05	1.61E-05	8.11
	-0.2	0.99	1.03	2.96	4.98	2.20E-05	7.85E-05	5.62E-06	4.54E-06	5.71E-05	2.01E-05	10.15
	-0.3	0.84	0.60	4.06	5.50	2.23E-05	1.04E-04	1.20E-05	7.17E-06	7.19E-05	2.63E-05	13.17
	-0.4	2.03	4.67	6.35	13.05	5.69E-06	1.42E-04	3.28E-05	8.34E-06	9.08E-05	3.70E-05	17.10
+0.3	Wingtip [0.0]	1.46	1.75	1.81	5.02	1.59E-05	5.05E-05	1.86E-06	1.98E-06	3.99E-05	1.36E-05	6.68
	-0.1	1.61	1.61	2.26	5.48	1.77E-05	5.98E-05	2.97E-06	2.23E-06	4.69E-05	1.61E-05	7.87
	-0.2	1.87	1.14	2.89	5.90	1.87E-05	7.16E-05	5.26E-06	2.36E-06	5.55E-05	1.95E-05	9.34
	-0.3	2.51	0.06	3.85	6.42	1.61E-05	8.61E-05	1.03E-05	1.83E-06	6.58E-05	2.42E-05	11.03
	-0.4	4.17	1.75	5.36	11.27	4.09E-06	1.01E-04	2.13E-05	8.70E-07	7.65E-05	3.06E-05	12.65
+0.4	Wingtip [0.0]	1.62	1.95	1.76	5.34	1.56E-05	4.98E-05	1.51E-06	1.92E-06	4.04E-05	1.36E-05	6.64
	-0.1	1.95	1.92	2.20	6.07	1.71E-05	5.81E-05	2.48E-06	1.52E-06	4.71E-05	1.61E-05	7.69
	-0.2	2.49	1.69	2.80	6.98	1.79E-05	6.80E-05	4.26E-06	4.93E-07	5.50E-05	1.91E-05	8.90
	-0.3	3.41	1.18	3.66	8.25	1.68E-05	7.93E-05	7.50E-06	1.77E-06	6.41E-05	2.30E-05	10.39
	-0.4	4.96	0.36	4.89	10.21	1.28E-05	9.11E-05	1.27E-05	6.22E-06	7.44E-05	2.77E-05	12.15

Table 54: Results of T&L Wing Sensitivity Analysis: Aft of Mid-Chord

MAD Location [m]		Absolute Value of T&L Coefficient										
		PERMANENT				INDUCED						
Aft X	Inboard Y	C1	C2	C3	SUM	C4	C5	C6	C7	C8	C9	SUM
Mid Chord [0.0]	Wingtip [0.0]	1.20	2.03	1.89	5.12	1.55E-05	5.05E-05	3.37E-06	2.95E-07	3.56E-05	1.26E-05	6.36
	-0.1	0.84	2.46	2.32	5.61	2.00E-05	6.41E-05	4.27E-06	1.13E-06	4.37E-05	1.54E-05	8.02
	-0.2	0.13	3.10	2.87	6.10	2.86E-05	8.94E-05	5.74E-06	5.02E-06	5.74E-05	2.00E-05	11.13
	-0.3	2.74	4.25	3.58	10.58	4.97E-05	1.50E-04	9.44E-06	1.62E-05	8.71E-05	2.92E-05	18.42
	-0.4	11.77	7.31	4.23	23.31	1.24E-04	3.51E-04	2.97E-05	5.49E-05	1.81E-04	5.37E-05	42.88
+0.1	Wingtip [0.0]	1.44	2.19	1.90	5.54	1.35E-05	4.82E-05	4.37E-06	2.57E-06	3.25E-05	1.20E-05	6.11
	-0.1	1.24	2.94	2.31	6.50	1.69E-05	6.04E-05	5.64E-06	2.12E-06	3.94E-05	1.45E-05	7.51
	-0.2	0.70	4.32	2.80	7.81	2.28E-05	8.19E-05	7.89E-06	1.20E-07	5.06E-05	1.86E-05	9.83
	-0.3	0.47	7.44	3.17	11.08	3.39E-05	1.28E-04	1.38E-05	5.91E-06	7.24E-05	2.63E-05	15.11
	-0.4	1.90	16.92	1.90	20.71	5.07E-05	2.46E-04	4.05E-05	2.15E-05	1.24E-04	4.45E-05	28.46
+0.2	Wingtip [0.0]	1.82	2.20	1.91	5.94	1.08E-05	4.48E-05	5.54E-06	5.43E-06	2.88E-05	1.12E-05	5.76
	-0.1	1.90	3.08	2.33	7.31	1.24E-05	5.44E-05	7.33E-06	6.49E-06	3.39E-05	1.33E-05	6.90
	-0.2	2.00	4.62	2.81	9.44	1.37E-05	6.89E-05	1.06E-05	7.55E-06	4.10E-05	1.65E-05	8.55

	-0.3	2.45	7.54	3.26	13.25	1.20E-05	9.23E-05	1.81E-05	8.85E-06	5.14E-05	2.17E-05	11.04
	-0.4	4.94	13.08	3.09	21.11	7.16E-06	1.27E-04	4.03E-05	1.33E-05	6.44E-05	3.10E-05	15.31
+0.3	Wingtip [0.0]	2.23	2.00	1.93	6.16	7.99E-06	4.10E-05	6.63E-06	8.41E-06	2.50E-05	1.03E-05	5.37
	-0.1	2.58	2.82	2.36	7.76	8.04E-06	4.81E-05	8.77E-06	1.10E-05	2.83E-05	1.20E-05	6.28
	-0.2	3.14	4.13	2.90	10.17	6.68E-06	5.72E-05	1.24E-05	1.48E-05	3.22E-05	1.43E-05	7.43
	-0.3	4.22	6.20	3.55	13.97	1.18E-06	6.83E-05	1.90E-05	2.08E-05	3.61E-05	1.75E-05	8.80
	-0.4	6.45	9.10	4.29	19.85	1.45E-05	7.88E-05	3.20E-05	3.12E-05	3.84E-05	2.19E-05	11.71
+0.4	Wingtip [0.0]	2.58	1.62	1.94	6.14	5.56E-06	3.74E-05	7.49E-06	1.11E-05	2.14E-05	9.42E-06	4.99
	-0.1	3.13	2.27	2.39	7.78	4.81E-06	4.28E-05	9.73E-06	1.50E-05	2.34E-05	1.08E-05	5.75
	-0.2	3.94	3.24	2.98	10.16	2.69E-06	4.90E-05	1.31E-05	2.06E-05	2.53E-05	1.24E-05	6.65
	-0.3	5.22	4.65	3.79	13.65	2.06E-06	5.57E-05	1.83E-05	2.93E-05	2.65E-05	1.44E-05	7.89
	-0.4	7.15	6.55	4.92	18.63	1.08E-05	6.17E-05	2.60E-05	4.29E-05	2.62E-05	1.66E-05	9.94

Appendix D – Comparison of UAV Flight Control Servos

The following tables compare the experimental results from this study with a study conducted on a series of flight control servos for the Brican TD100 UAV [8]. Overall, the Currawong CBS-15 flight control servo on the Nebula N1 is had a relatively low magnetic signature.

Table 55: Magnetic Parameter Comparison: Other Flight Control Servos

	Tested for Brican TD100 [8]				**Nebula N1**
Parameter	**Volz DA-05-60**	**HiTec HSR 5990TG**	**HiTec 7955TG**	**MKS HBL850**	**Currawong CBS-15**
$\|M_{P\,x}\|$ **[nTm^3]**	3.510	6.770	10.250	0.001	0.012
$\|M_{P\,y}\|$ **[nTm^3]**	4.440	1.030	5.320	0.019	0.015
$\|M_{P\,z}\|$ **[nTm^3]**	2.110	0.200	0.170	0.036	0.126
$\|\chi_x\|$ **[m^3]**	2.68E-04	1.54E-05	7.69E-04	7.00E-07	4.57E-07
$\|\chi_y\|$ **[m^3]**	7.98E-05	2.49E-05	5.30E-04	5.00E-07	3.32E-07
$\|\chi_z\|$ **[m^3]**	4.05E-05	5.30E-06	2.59E-04	4.00E-06	1.12E-06

Table 56: T&L Absolute Value Coefficient Results – Comparison of Other UAV Flight Control Servos

	Tested for Brican TD100 [8]				**Nebula N1**
T&L Coefficient	**Volz DA-05-60**	**HiTec HSR 5990TG**	**HiTec 7955TG**	**MKS HBL850**	**Currawong CBS-15**
C_1	35.12	-67.74	-102.56	0.01	0.55
C_2	-138.27	-41.27	251.65	2.03	0.15
C_3	-62.88	-13.8	68	0.15	-0.03
C_4	-2.68E-03	-1.54E-04	-7.70E-03	-7.00E-06	-4.87E-06
C_5	6.09E-03	3.50E-04	1.75E-02	1.60E-05	1.45E-05
C_6	1.95E-03	1.12E-04	5.60E-03	5.00E-06	1.27E-07
C_7	-1.02E-03	3.17E-04	6.74E-03	6.00E-06	2.85E-06
C_8	-1.50E-03	3.02E-04	9.74E-03	9.50E-05	5.95E-06
C_9	1.10E-04	-1.44E-05	-7.05E-04	-1.10E-05	-1.94E-06

Appendix E – Magnetic Noise Sources – Full Mind Map

The following figure summarizes all sources of magnetic interference discussed in section 2.2. This figure is the full mind map to which most figures in section 2.2 were taken.